SPECTRAL CONTROL OF TOTAL INTERNAL REFLECTION FOR NOVEL INFORMATION DISPLAYS

by

MICHELE ANN MOSSMAN

B.Sc.H., Acadia University, 1995
M.Sc., University of British Columbia, 1997

A THESIS SUBMITTED IN PARTIAL FULFILLMENT OF

THE REQUIREMENTS FOR THE DEGREE OF

DOCTOR OF PHILOSOPHY

in

THE FACULTY OF GRADUATE STUDIES

(Department of Physics and Astronomy)

We accept this thesis as conforming
to the required standard

THE UNIVERSITY OF BRITISH COLUMBIA

April 2002

Department of Physics & Astronomy

The University of British Columbia
Vancouver, Canada

Date 17 April 2002

ABSTRACT

A new method for creating a reflective image device has been devised based on total internal reflection (TIR). This technique has the potential to yield a brighter, higher-contrast image than those of current reflective displays by incorporating polymeric micro-prismatic sheets that reflect by means of TIR. High surface reflectance is achieved by efficiently redirecting ambient light toward the viewer, and an image is generated by controllably preventing, or "frustrating", the reflection in selected regions through absorption of light in the very thin evanescent wave region near the TIR interface. The transition between the reflective and absorptive state requires a motion of less than a micron of the absorber, and therefore it can occur quickly and efficiently.

A fundamental problem in this approach – interfacial adhesion – was ameliorated through the use of liquid phase backing material, instead of gas. However, this complicated the optical requirements by substantially reducing the refractive index ratio at the TIR interface. To maintain TIR over an acceptable angular range, a low refractive index perfluorinated hydrocarbon was identified as an ideal liquid, and an optical configuration was devised to enhance the effective refractive index ratio at the interface.

Detailed Monte Carlo ray tracing verified that high reflectance and a high contrast ratio are achievable with these designs over a useful range of viewing directions.

Electrophoresis of pigment particles in a perfluorinated hydrocarbon has been shown to be a practical method for modulating TIR. The observed photometric performance is consistent with a numerical model developed to describe the interaction of an incident light ray with a density distribution of particles near the interface. Colour pigment suspensions have yielded, for the first time, spectrally selective control of TIR, which requires the particles to be essentially non-scattering but selectively absorptive.

The results presented here demonstrate the feasibility of this TIR-based approach in practical reflective image device applications, and are suggestive that further development work in this area is warranted.

ABSTRACT

A new method for creating a reflective image device has been devised based on total internal reflection (TIR). This technique has the potential to yield a brighter, higher-contrast image than those of current reflective displays by incorporating polymeric micro-prismatic sheets that reflect by means of TIR. High surface reflectance is achieved by efficiently redirecting ambient light toward the viewer, and an image is generated by controllably preventing, or "frustrating", the reflection in selected regions through absorption of light in the very thin evanescent wave region near the TIR interface. The transition between the reflective and absorptive state requires a motion of less than a micron of the absorber, and therefore it can occur quickly and efficiently.

A fundamental problem in this approach – interfacial adhesion – was ameliorated through the use of liquid phase backing material, instead of gas. However, this complicated the optical requirements by substantially reducing the refractive index ratio at the TIR interface. To maintain TIR over an acceptable angular range, a low refractive index perfluorinated hydrocarbon was identified as an ideal liquid, and an optical configuration was devised to enhance the effective refractive index ratio at the interface.

Detailed Monte Carlo ray tracing verified that high reflectance and a high contrast ratio are achievable with these designs over a useful range of viewing directions.

Electrophoresis of pigment particles in a perfluorinated hydrocarbon has been shown to be a practical method for modulating TIR. The observed photometric performance is consistent with a numerical model developed to describe the interaction of an incident light ray with a density distribution of particles near the interface. Colour pigment suspensions have yielded, for the first time, spectrally selective control of TIR, which requires the particles to be essentially non-scattering but selectively absorptive.

The results presented here demonstrate the feasibility of this TIR-based approach in practical reflective image device applications, and are suggestive that further development work in this area is warranted.

TABLE OF CONTENTS

LIST OF TABLES

LIST OF FIGURES

ACKNOWLEDGEMENTS

First and foremost, I would like to thank past and present SSP team members for making the lab such an enjoyable place to work. In particular, I would like to acknowledge the assistance provided by Januk Aggarwal, Karla Boucher, Kevin Cheng, Alison Clark, Robin Coope, Roger Donaldson, Vincent Kwong, Anne Liptak, Jill Miwa, Jordan Schultz, Helge Seetzen, Kim Tkaczuk and Ben Tippett. Special thanks to Kiri Nichol for all her hard work in becoming our initial raytrace pro.

Sincere thanks to Andrzej Kotlicki for his assistance and advice with this research program over the past few years. I would also like to express my appreciation to the members of my supervisory committee, Boye Ahlborn, Brian Turrell and Chris Waltham for their always helpful advice during the preparation of this thesis.

The collaborative nature of our work has provided the opportunity to learn from many professionals from the 3M Company. Thanks to David Arney, Rolf Biernath, Steve Buckingham, Kathleen Dennison, David Kowitz, Pat McGuire, Mark Pellerite, John Potts, and Rick Weiss for the time they have devoted to this research program. Special thanks to S.P. Rao for his very significant scientific contribution in the development of the pigment particle suspensions used in this research.

I am grateful to NSERC, UBC, and the family of Mr. Li Tze Fong for their financial support throughout the course of this project.

To my research supervisor, Lorne Whitehead: you have created in the lab a unique atmosphere, which blends both academic and industrial approaches to physics. From your approach, I have learned more than I could have hoped for, and I would like to sincerely thank you.

Finally, to the "Fromthepools", who join me for my much-needed fix each day, thanks for keeping me afloat. To Telus, thanks for the flat rate that keeps me in close touch with my wonderful friends across the continent. And to Mom and Dad, Jennifer, Scott, Gardie, Amanda and little Zoe, thanks for making the distance between us seem so much shorter.

1 INTRODUCTION

Reflective image devices have become increasingly important in a wide range of applications, from small displays used in hand-held electronic devices to large roadside displays used to provide information to passing motorists. In such devices, the bright regions of an image are created by reflecting ambient light toward the viewer, while the dark regions are created by absorbing this ambient light. By using spectrally selective absorption, full colour images are also possible. Although the specific requirements for a reflective image device depend on the particular application, it is always preferable to produce an image that looks bright and colourful under a wide variety of lighting conditions, with a minimum of power consumption.

Despite significant research efforts by numerous organizations, current reflective image display technologies leave much to be desired. The reflectance of current commercially available reflective displays is at best 35% for a black and white image, and less than 16% for a full-colour image, as a result of inherent limitations in the mechanism by which the reflection occurs. This limited brightness makes these displays difficult to read under many common lighting conditions. While some new technologies are claimed to have the potential to exceed these reflectance values, these have not yet been proven.

The work presented in this thesis establishes a new technology for a reflective image device. Total internal reflection is used as the mechanism to reflect light rays striking the surface, redirecting them back toward the viewer. Total internal reflection, typically abbreviated as "TIR", is the well-known phenomenon that occurs when a light ray travelling through a material arrives at an interface with a second, less optically dense material. If the ray strikes that interface with a sufficiently large incident angle, it will undergo TIR, and there will be no net transfer of light across the interface. Under these conditions, the light completely reflects, providing a mechanism of reflection that is, in principle, 100% efficient.

Although there is essentially no transmitted radiation with TIR, a complete solution of the electromagnetic fields at the interface shows that some electromagnetic energy, known as the evanescent wave, does penetrate a small distance into the second material, in an exponentially tapered fashion. The penetration depth, for visible light, is typically less than

0.25 μm, or about half of the wavelength. The conditions for TIR depend on the optical properties in this very thin evanescent wave region, so by altering those properties, (for example, by moving a scattering or absorbing material into the region), the reflectance at the interface can be reduced. This is sometimes known as "frustration" of TIR. In a reflective image device based on TIR, such frustration must be selectively, and controllably, applied to generate the desired dark and light portions of the image.

The general idea of evanescent wave scattering is not new; it has been used to study the optical properties of scattering materials and in the field of TIR microscopy. In addition, it has been proposed as an optical switch for fibres, where a scattering material is moved into the evanescent wave region and prevents further propagation of the light along the fibre. However, to the best of our knowledge, this thesis represents the first use of controlled frustration of TIR in a reflective image display.

The TIR-based approach has three unique features in comparison to other reflective displays. First, a reflectance of near-100% is practical. Readily available optically microstructured polymeric sheets can produce the required reflection. Second, only a very slight movement of the absorber can switch the frustration on and off. The absorber need only move in and out of the evanescent wave region, a distance of less than 0.5 μm, and can therefore, in principle, switch the reflectance quickly. Finally, subtractive colour filtering can be employed to yield a full colour image. Unlike other colour display technologies, this approach allows the uses of an array of efficient, subtractive filters, in a single electro-optic layer, to produce a bright, full colour display.

One of the challenges of positioning an absorber in the tiny evanescent wave region is that direct physical contact is problematical, due to adhesion forces. Such adhesion would greatly increase the required actuating force and power consumption. It was therefore concluded during the course of this study that such solid-solid adhesion must be substantially reduced. One way to do so is to use a liquid, rather than air, as the second interfacial material. However liquids have a much higher refractive index than air, making it more difficult to achieve TIR than at a solid-air interface. This led to identification of a low index perfluorinated hydrocarbon liquid, as well as the development of a novel geometrical

approach to enhance the effective refractive index ratio in order to achieve TIR over a useful angular range with a solid-liquid interface.

A number of possible absorbing materials were investigated. The most promising system uses a liquid suspension of electrostatically charged pigment particles to frustrate the TIR. These pigment particles must be optically small such that they are essentially non-scattering, and sufficiently absorptive that they effectively frustrate the TIR. Under an applied electric field, the particles can be moved into and out of the evanescent wave region to modulate the surface reflectance, using the well-known mechanism of electrophoresis. Another new result of this work is the demonstration that by using sub-optical coloured pigment particles, the spectral distribution of the reflected light can be controlled. This is a requirement for the operation of a full colour device based on TIR.

To best understand the work presented here, it will be helpful to review the diverse set of physical and psychophysical phenomena involved. Chapter 2 briefly reviews some useful background information in each of these areas, as appropriate to the context of this thesis. In addition, a brief description of other reflective display technologies is included, in order to provide a framework for comparison to the new TIR-based approach.

In Chapter 3, factors specifically influencing the design of a TIR-based reflective image display are discussed. In particular, the rationale for the use of a solid-liquid TIR interface, in terms of the surface energy considerations, is presented, as well as the method of enhancing the effective refractive index ratio at the interface. Key features of the pigment suspensions incorporated into the device are discussed, as well as the method of subtractive colour filtering to generate a full colour image.

Experimental results demonstrating spectrally selective reflectance by the electrophoresis of pigment particles are provided in Chapter 4. This new observation is one of the cornerstones of this thesis. In addition to the demonstration of such spectral control of the reflected light, the reflectance response to time-varying electric fields was analyzed. Such time-varying reflectance modulation is crucial to the use of pigment electrophoresis in a TIR-based reflective image device, in which the image must be regularly updated. Additionally, a study of this reflectance change under a number of different experimental conditions was

undertaken in order to develop a more complete understanding of the dynamics of the electrophoretic pigment particles. These experimental measurements are presented in Chapter 5.

One of the conclusions from these measurements is that the particles have sufficient density to modify the energy distribution in the evanescent wave, making simple absorption models incomplete. In Chapter 6, a more sophisticated model of the evolving particle density distribution near the interface was developed to explain the level of absorption measured in the previous experiments. A number of possible distributions were considered and one with a maximum density limit and an exponentially tapered tail was found to best match the experimental observations.

Chapter 7 describes the investigation of several possible configurations of micro-prismatic sheets comprising a TIR-based display. Computer ray trace models were designed to determine the reflectance of these structures at different viewing angles. In the last section of this chapter, a sample of one of these structures is incorporated into an electrophoretic pigment test cell and the measured reflectance is compared with the model predictions. These results establish the feasibility of using electrophoretic pigments in an image device based on frustrated TIR, and suggest a number of areas for further work.

2 BACKGROUND

The work presented in this thesis incorporates key ideas from several disparate fields. This introductory chapter provides a relevant background discussion in each of these areas in order to show how they relate to one another in the context of the research subsequently presented.

2.1 Total Internal Reflection

The primary focus of this study involves the application of total internal reflection (henceforth abbreviated "TIR") to a reflective image device. TIR occurs when light traveling in a material reaches an interface with a material of lower index of refraction, at a sufficiently large incident angle. In this section, this well-known phenomenon is reviewed.

2.1.1 Index of refraction

Light, being an electromagnetic disturbance, causes the displacement of local charges as it propagates through a material. These moving charges, in turn, produce additional electromagnetic disturbances that combine with the original to form a wave that travels slower than light in a vacuum. The propagation speed of this wave in a particular material depends on the properties of that material, summarized as the index of refraction, n, which is the ratio of the speed of the light in vacuum, c, to its speed in the material, v:

$$n = \frac{c}{v} \tag{2-1}$$

The index of refraction of air at STP is about 1.0003, whereas more optically dense materials such as water and glass (depending on its type) have index values of approximately 1.33 and 1.51, respectively. The value of n depends on the wavelength of the light, but for the materials considered throughout the course of this study, this wavelength dependence is quite slight.

The refractive index of a material is determined by the relative permittivity, ε_r and the relative permeability, μ_r.

$$n = \sqrt{\varepsilon_r \mu_r} \tag{2-2}$$

In nonmagnetic materials, such as those considered in this study, μ_r=1, and (2-2) becomes:

$$n = \sqrt{\varepsilon_r} \tag{2-3}$$

It is well known that dielectric materials can exhibit energy loss in oscillating fields and that these losses can be represented mathematically by an imaginary component of the dielectric constant.[1] Similarly, the index of refraction can also have both real and imaginary components,

$$n = n' + in'' \tag{2-4}$$

where the imaginary component represents the absorbance of the material. In a purely transparent material, $n'' = 0$, but if the intensity of the light diminishes as the wave propagates, then n'' (and therefore the imaginary component of the dielectric constant, ε_r'') has a nonzero value. Under these circumstances, the intensity of the wave decreases exponentially, at a rate described by the absorption coefficient, *k*, of the material. The intensity, *I*, after the wave has propagated a distance *x* is given by

$$I = I_0 e^{-kx} \tag{2-5}$$

where I_0 is the initial intensity. *k* is related to ε_r'' by the following relation[2]:

$$k = \frac{2\pi\varepsilon_r''}{n'\lambda} \tag{2-6}$$

The index of refraction describes the propagation of light in optically different materials and is a fundamental concept in this study, since this parameter determines the conditions for TIR, as explained in the next section.

2.1.2 Conditions for TIR at an interface

A typical depiction of TIR is shown in Figure 2-1. An electromagnetic wave, represented by a light ray, strikes an interface between two optically different materials, the first having a refractive index value of n_1, and the second a lower value, n_2.

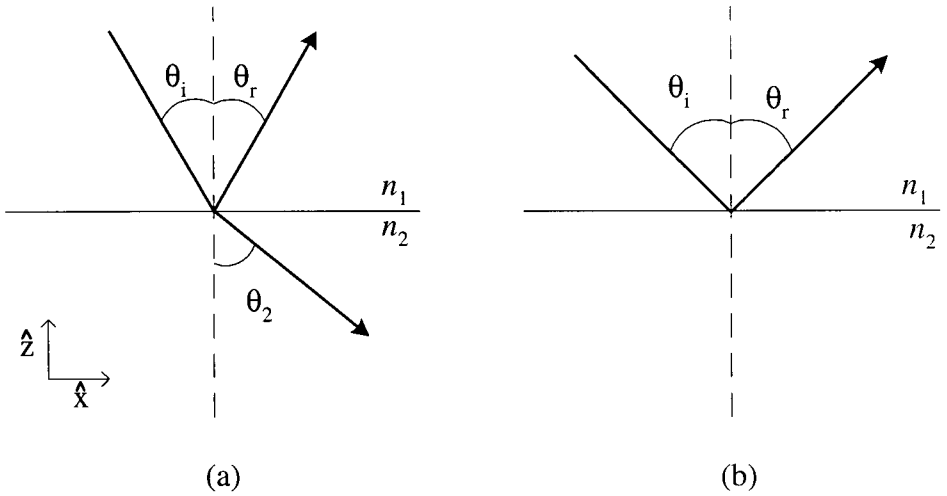

Figure 2-1. Reflection, refraction and TIR at an interface

As the light ray passes from the higher index medium to the lower one depicted by Figure 2-1(a), it refracts away from the surface normal at an angle θ_2, as governed by (2-7), known as Snell's law:

$$\theta_2 = \arcsin\left((n_1/n_2)\sin\theta_1\right) \tag{2-7}$$

TIR, shown in Figure 2-1(b), occurs when Snell's law generates a complex solution for the refracted angle θ_2. This occurs for all light rays having incident angles greater than a critical angle θ_c, derived from (2-7):

$$\theta_c = \arcsin\left(n_2/n_1\right) \tag{2-8}$$

From (2-8) it is clear that the conditions for TIR depend on the ratio of the refractive indices of the two materials.

In many texts, the optical situation is simplified to the special case of a discontinuity in refractive index across the interface[3]. However, in its most general form, Snell's law describes the situation when a light ray passes from one region of uniform value of refractive index into a second having a different index value, and there is no requirement that the index transition between the two regions be abrupt. In fact, it is not uncommon to find continuous index gradients in nature[4], and optical engineers often construct this transition in several steps for practical reasons[5]. However, the discontinuous situation depicted in Figure 2-1 is most often presented because, in this special case, the Maxwell equations can be analytically solved in a straightforward manner.[6] It will be helpful to consider ray propagation in the more general case in which the refractive index changes continuously.

The differential form of Snell's law, used to describe the path a light ray follows as it enters a region of refractive index gradient, is given (2-9),[7]

$$\frac{d}{dl}(n\hat{r}) = \bar{\nabla} n \qquad \textbf{(2-9)}$$

where l is the path length along the ray path, $\hat{r}$ is the ray direction at the point l and n is the index at that point. At each incremental step dl along the ray path l, $\hat{r}$ is determined by this differential equation. A differential algorithm based on (2-9) is employed in Chapter 6 in order to predict the path and the absorption of a light ray as it passes through a distribution of pigment particles in a fluid medium.

Figure 2-2 shows a situation where the refractive index gradually changes from one value to another over a distance much greater than a wavelength, with the paths predicted by numerical integration of (2-9). Here, the partial reflectance is essentially zero for angles of incidence less than the critical angle, and TIR occurs for angles greater than critical. Each light ray curves as it passes through the gradient. Just as in Figure 2-1, if the angle is less than the critical angle, the ray will transmit. Otherwise, it will reflect by TIR.

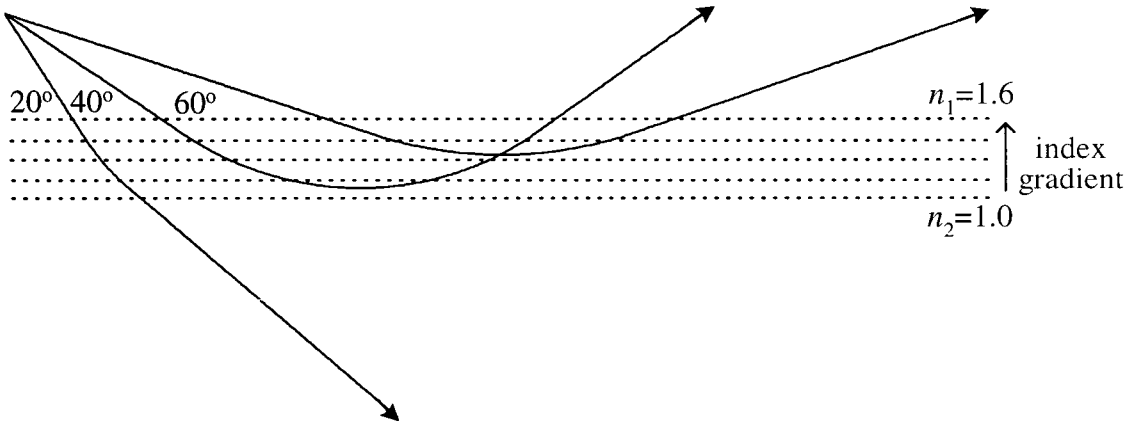

Figure 2-2. Path of light rays in a refractive index gradient

The case where TIR occurs in a region of refractive index gradient is a key feature in the discussion presented in Chapter 6, and will be discussed in further detail there. In the meantime, it is important to consider the distribution of electromagnetic energy when TIR occurs.

2.1.3 The evanescent wave

As described in Section 2.1.1, when the angle of incidence exceeds the critical angle, Snell's law generates a complex angle of refraction, written as (2-10).

$$\theta_2 = a + ib \tag{2-10}$$

The resultant wavenumber, $\mathbf{k}_2$, of the transmitted wave is complex[8], as in (2-11).

$$\mathbf{k}_2 = k_2\left(\sin\theta_2\hat{\mathbf{x}} + i\sinh b\hat{\mathbf{z}}\right) \tag{2-11}$$

Since there is no real component of $\mathbf{k}_2$ perpendicular to the interface, this form implies that there is no net transfer of electromagnetic energy across the interface under these conditions. However, (2-11) shows that some electromagnetic field does penetrate a small distance into the second medium, as shown pictorially in Figure 2-3. This is equivalent to the fact that in

the full solution of the Maxwell equations at the interface, the Poynting vector of the evanescent wave is parallel to the surface.[9]

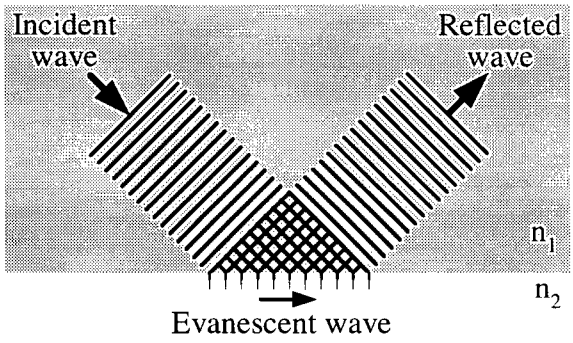

Figure 2-3. Pictorial representation of the evanescent wave

This so-called evanescent wave propagates along the interface, but its strength drops off exponentially with distance into the second medium, so it effectively penetrates only a very short distance into the material. This effective penetration distance, δ, depends on the angle of incidence, θ_1 (since b depends on θ_1), and the wavelength, λ_2, and is given by[8] (2-12).

$$\delta = \frac{\lambda_2}{2\pi \sinh b} \qquad \textbf{(2-12)}$$

Figure 2-4 plots the evanescent wave depth for light striking a glass-air interface ($n_1 \cong 1.5$, $n_2 \cong 1.0$) interface, at a wavelength, λ_2, of 500nm, as a function of incident angle. The critical angle, θ_c, in this case is about 41.8°. The angular dependence of the plot shows that very close to the critical angle, the wave penetrates a relatively long distance into the air, and the depth rapidly declines as the incident angle decreases. Except in the very narrow range just past the critical angle, for visible light, the penetration depth is about half a wavelength, or 0.25 μm.

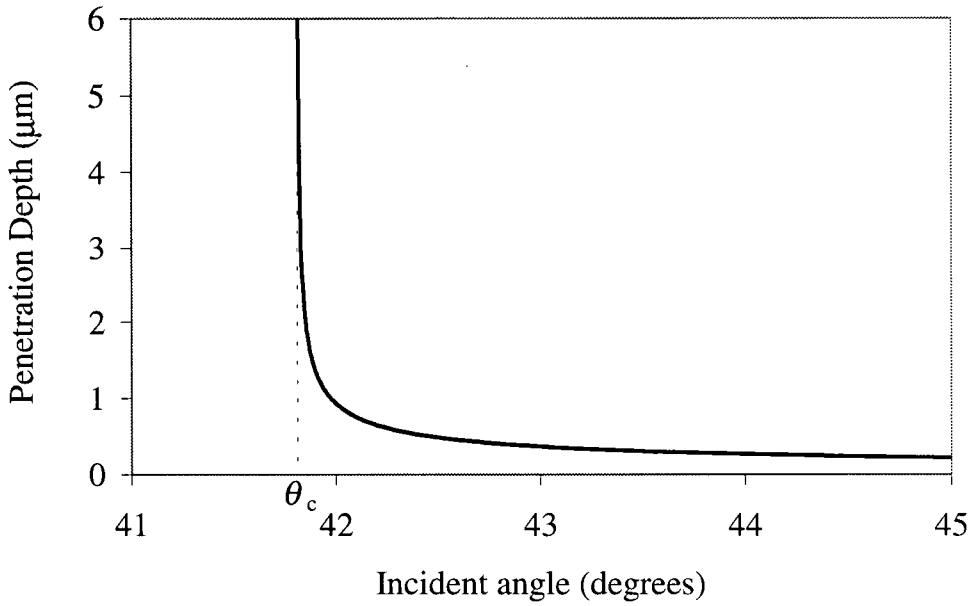

Figure 2-4. Evanescent wave depth for glass/air interface

As will be discussed in the following section, the occurrence of TIR at an interface can be prevented by absorbing the electromagnetic energy in the evanescent wave region. For this reason, it will be helpful to more carefully consider such interactions.

2.1.4 Frustrated TIR

As described in Section 2.1.2, the occurrence of TIR is dependent upon the optical properties of the materials. It therefore follows that reflectance can be controlled by altering the optical properties at the interface. Specifically, TIR can be prevented or "frustrated" by scattering or absorbing the electromagnetic energy in the evanescent wave. By moving a highly absorptive material into the evanescent wave region, almost all of the light can be absorbed, and if the absorber is returned to the region just outside the zone in which the evanescent wave penetrates, complete reflection is restored. This effect is depicted schematically in Figure 2-5.

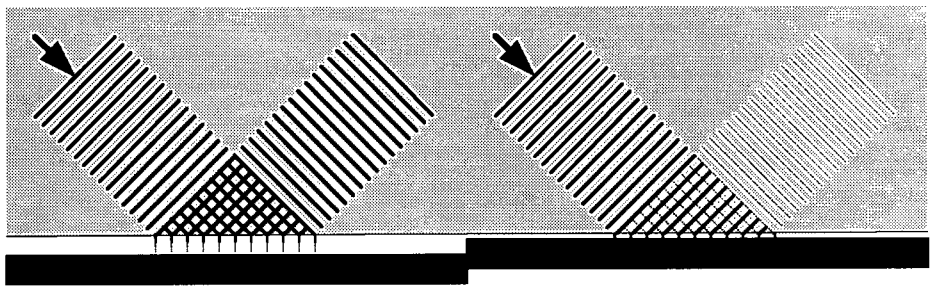

Figure 2-5. (a) TIR and (b) frustration of TIR by an absorptive material

It is remarkable that such a dramatic reduction in reflectance can occur by moving the absorber such a small distance. The fact that the evanescent wave only penetrates typically less than half a micron into the second medium is responsible for this effect.

The idea of using evanescent wave scattering for an optical switch is not new; it has been proposed for a particular application in optical fibres, where a scattering material is moved into the evanescent wave region and prevents further propagation of the light along the fibre.[10] However, the work presented in this thesis is, we believe, the first demonstration of controlled frustration of TIR in a reflective image display.

The development of a practical reflective image device based on this controlled TIR approach required the use of specially designed reflective sheets. These are described in the following section.

2.2 Geometrical optics

To yield a reflective image device, the effect of frustrated TIR can be employed in conjunction with special reflective sheets made by micro-replication techniques. These microstructured sheets can have customized optical properties based on their specific design details.

2.2.1 Micro-replicated sheets

There are many applications in which it is desirable to have a material whose surface contains tiny, yet very precise, structures. For example, for the abrasives industry, microscopic pyramids of an abrasive material can be created on a sheet to yield a type of sandpaper with better qualities than the traditional random assortment of particulates.[11] As the structures wear down, they maintain their pyramidal shape and, as a result, greatly extend the lifetime. In a number of fluid transport applications, very small channels have been structured into an otherwise hydrophilic material to direct fluid away from certain regions. Of particular interest in regard to this thesis, microstructured prismatic surfaces are made using clear polymer resin, and these surfaces can be designed such that TIR occurs when light is directed at the sheet.[12]

The process used to form these optical structures, known as micro-replication, uses a carefully designed mould, typically made of a robust metal alloy. Although there are a number of micro-replication techniques, typically the uncured polymer resin is poured into the mould and cured under high heat and pressure. The resulting microstructures are essentially optically clear in the bulk, with less than 2% absorption[13], and the surfaces of the structures are optically smooth. (The phrase "optically smooth" means that the surface inaccuracies are much smaller than a wavelength of light.) Sheets of polycarbonate micro-prisms with a pitch of 50 μm and included angle of both 90° and 70° are currently readily available.[14,15] Research and development is continuing in the field of micro-replication, to produce sheets with new surface profiles and higher refractive indices.

To describe in more detail the interaction of light with these microstructures, it is helpful to consider a specific example: Figure 2-6(a) shows an isometric drawing of an optical system having translational symmetry along a direction $\mathbf{r}_{\parallel}$. (In other words, the system has the same shape in all cross sectional planes perpendicular to $\mathbf{r}_{\parallel}$, as shown in Figure 2-6(b) and therefore has linear features, as in an extrusion.) In this example, the cross-section of the surface structure is a series of prisms having an included angle of 90°.

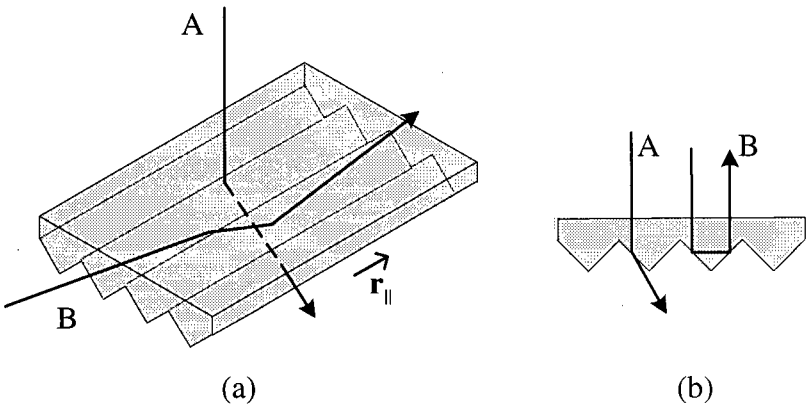

Figure 2-6. (a) Isometric and (b) cross-sectional view of an optical system

Light rays incident on the surface will either reflect or refract, depending on their incident angle. Figure 2-6(a) shows two rays, where ray A transmits and ray B undergoes TIR, and Figure 2-6(b) shows the projection of these paths on to such a cross sectional plane.

One of the special features of an optical system having translational symmetry is the fact that a light ray traveling with a component of motion along the symmetry axis behaves as though the refractive index ratio is enhanced. This effect is important for the research described in this thesis, and it will therefore be useful to expand on this in the next section.

2.2.2 Enhanced refractive index ratio

As mentioned above, under certain circumstances, a light ray with a component propagating in the direction of the translational symmetry exhibits an enhanced response to index transitions.[16] Consider again the light rays shown in Figure 2-6. It is simplest to describe the path of rays in terms of the wave vector, $\mathbf{k}$, of the associated plane wave, whose phase, ϕ, is given by

$$\phi = \mathbf{k} \cdot \mathbf{r} - \omega t \qquad \textbf{(2-13)}$$

In (2-14), $\mathbf{k}$ is resolved into components parallel and perpendicular to the direction of translational symmetry:

$$\mathbf{k} = \mathbf{k}_{\parallel} + \mathbf{k}_{\perp} \text{ where } \mathbf{k}_{\parallel} = (\mathbf{k} \cdot \mathbf{n}_{\parallel})\, \mathbf{n}_{\parallel} \text{ and } \mathbf{k}_{\perp} = \mathbf{k} - \mathbf{k}_{\parallel} \qquad \textbf{(2-14)}$$

The translational symmetry of the system ensures that $\mathbf{k}_{\|}$ is a constant of the motion for any given ray. Since the path followed by the ray is changed only upon interaction with a medium of different refractive index, the translational symmetry of this structure in the $\mathbf{r}_{\|}$ direction ensures that this directional component will not change, regardless of the initial ray angle. It will be helpful to define a dimensionless constant of the motion, κ, as follows:

$$\kappa = \frac{k_{\|}}{k_0} \text{ where } k_{\|} = \left|\mathbf{k}_{\|}\right| \text{ and } k_0 = \omega / c \qquad \textbf{(2-15)}$$

One can think of κ as a measure of the extent to which the wave vector lies in the direction of translational symmetry, relative to the magnitude of the free space wave vector, k_0. κ is a constant of the motion for any given ray, and can have a value ranging from zero (for a light ray traveling perpendicular to the direction of translational symmetry) to the highest value of refractive index in the system (for rays traveling parallel to the symmetry direction). It is easy to determine κ; it is given by:

$$\kappa = n\cos\alpha \qquad \textbf{(2-16)}$$

where n is the index of the material through which the ray travels at some particular point in its path, and α is the angle, at that point, between the ray direction and the direction of translational symmetry, (in other words, $\alpha = \arccos(\mathbf{k} \cdot \mathbf{r}_{\|})$). Thus,

$$\kappa = n(\mathbf{k} \cdot \mathbf{r}_{\|})$$

In turn, α can be determined from the index of the medium and the value of κ, employing the converse of (2-16):

$$\alpha = \arccos\left(\frac{\kappa}{n}\right) \qquad \textbf{(2-17)}$$

If the ratio κ/n exceeds unity in a given medium (hence making α complex), TIR prevents the ray in question from entering that material regardless of the ray's direction in the cross sectional plane. This is often the situation in waveguides. As a result, κ is an indication of the degree to which the propagation media confine a particular ray.

From this perspective, the propagation of a ray in the cross-section perpendicular to the symmetry axis can be considered.[17] To do so, the component of travel in the symmetry direction must be taken into account, and fortunately, this can be done in a simple manner. In Figure 2-7, the angles θ_i' and θ_j' represent the apparent angles of incidence and transmission of the cross sectional projection of actual ray paths. It would be helpful to find a simple relationship of these angles in analogy to Snell's Law.

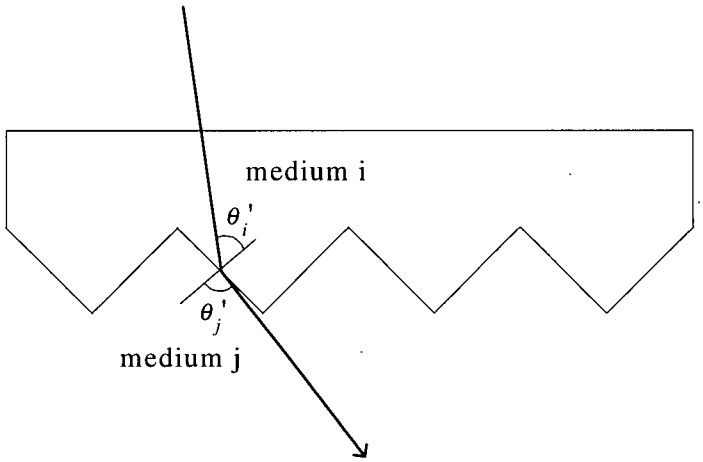

Figure 2-7. Apparent angles for two-dimensional projection of a ray path

It is straightforward to show that a simple expression does indeed relate these angles:

$$(n_i^2 - \kappa^2)^{1/2} \sin\theta_i = (n_j^2 - \kappa^2)^{1/2} \sin\theta_j \qquad \textbf{(2-18)}$$

where κ is defined, as previously discussed, in (2-14). This looks just like Snell's law, if one replaces the refractive index, n, of a given medium by an effective reduced index n' given by

$$n' = \sqrt{n^2 - \kappa^2} \qquad \textbf{(2-19)}$$

Since this reduction is proportionately greater for lower index materials, the result can be a substantial enhancement of the effective index ratio between two media.[18] This in turn enables TIR to occur over a wider range of azimuthal angles than would be the case without such propagation in the direction of translational symmetry.

As will be described in Section 3.3, this index ratio enhancement technique can be incorporated into a reflective image device as a way of overcoming some optical limitations. In the meantime, it is important to consider how best to measure the reflectance of a surface, as a means of evaluating its behaviour. The next section discusses the surprisingly subtle problem of describing surface reflectance in general.

2.2.3 Specification of reflectance in prismatic systems

An optical surface is considered to be a structure that is macroscopically planar over a region that is larger than the scale of its surface structure or optical penetration depth, so that its macroscopic surface normal is well defined. The measurement of the reflectance of an arbitrary optical surface is a complex, but well-established field. The luminance of a surface, as seen from a particular viewing angle, is determined as the solid-angle integral of the product of the bi-directional reflectance distribution function (BRDF) and the luminance distribution of the ambient environment.[19] In the special case of a perfectly diffuse surface, this relationship can be summarized as a single number called reflectance. For non-diffuse surfaces, the luminance depends on the viewing angle and the ambient luminance distribution, and this dependence is often quite complex. The prismatic structures discussed in this thesis are inherently angularly dependent, so this issue must be addressed. For simplicity in this discussion, unless otherwise indicated, the reflectance of a surface is defined as the ratio of the surface luminance, at a defined viewing angle, to that of a standard sample, when the surface and the standard are in a uniformly luminous environment. This sample can be either a near-100% reflective diffuse white surface[20], or a near-100% reflective specular surface[21], depending on the desired specifications. The calculation of reflected luminance based on the BRDF is explained in further detail in Appendix B.

All of the above discussion is based on light rays of unspecified wavelength. In modern displays, however, it is desirable to reproduce colour information, so it is now appropriate to review the methods for specifying the colours resulting form wavelength-dependent processes.

2.3 Colour

Light can be defined as visually evaluated radiant energy, in the wavelength band extending from about 380 nm to 780 nm, and colour is the characteristic of light by which an observer may distinguish between different spectral power distributions. This section briefly discusses some of the standard methods for measuring and producing colour.

2.3.1 Measurement of colour

The measurement of the spectral distribution of radiant power results in physical information, however the evaluation of colour by a human observer is psychological. It is fascinating that some aspects of colour perception are observer-independent, whereas others are purely subjective. Here, the former are considered, which arise from the existence in the human retina of specific photoreceptor molecules having fixed universal action spectra.[22] In this regard, the Commission Internationale de l'Éclairage (CIE) established a number of standards for the colour interpretation of spectral data. In particular, a set of colour-matching functions was developed using standardized conditions of observation.[23] As well, the CIE has recommended the spectral power distribution of several standard illuminants, designed to behave like common natural or artificial light sources, for calculating colour. The more modern and preferred of these is Standard Illuminant D_{65}, representing a phase of daylight at a correlated colour temperature of approximately 6500 K.[24]

2.3.2 CIE method of colour specification

Light with a given spectral power distribution is perceived to have a particular colour, but most of such colours can be reproduced by a number of different spectral power distributions. The different distributions in this set are called metamers and the basic method used to define all metameric pairs is the CIE method of colour specification.[25]

Mixing specific proportions of three primary colours can generate any colour. In other words, a particular colour, D, can be described in terms of the amounts a, b and c of primary colours A, B and C, respectively.

$$D=aA+bB+bC \tag{2-20}$$

The primary additive colours of light are considered to be blue, green and red. This arises from the fact that receptors in the human eye are predominantly responsive to light stimuli in these wavelength bands. However, it is important to note that a set of primary colours can be any three colours that are mutually independent in the sense that none can be matched by mixing the other two. The amounts a, b and c of these three primary colours can be calculated by combining the spectral power distribution of a standard source and the spectral reflectance of the object being measured.

The CIE method established a basic standard for the unambiguous specification of colours by defining a set of primary functions, X, Y and Z, which can be used to convert a given spectral irradiance distribution of a light source, $S(\lambda)$, into standard tristimulus values. These primaries do not refer to particular colours, but instead provide a convenient approach to numerically describing colour. These primary functions are given by:

$$X = k \sum_{\lambda=380\text{nm}}^{780\text{nm}} S(\lambda)\bar{x}(\lambda)\Delta\lambda \tag{2-21}$$

$$Y = k \sum_{\lambda=380\text{nm}}^{780\text{nm}} S(\lambda)\bar{y}(\lambda)\Delta\lambda \tag{2-22}$$

$$Z = k \sum_{\lambda=380\text{nm}}^{780\text{nm}} S(\lambda)\bar{z}(\lambda)\Delta\lambda \tag{2-23}$$

where k is the normalization factor that ensures that:

$$k \sum_{\lambda=380nm}^{780nm} \bar{x}(\lambda)\Delta\lambda = k \sum_{\lambda=380nm}^{780nm} \bar{y}(\lambda)\Delta\lambda = k \sum_{\lambda=380nm}^{780nm} \bar{z}(\lambda)\Delta\lambda = 683 \ \mathrm{lmW^{-1}} \quad \textbf{(2-24)}$$

and $\bar{x}(\lambda)$, $\bar{y}(\lambda)$, and $\bar{z}(\lambda)$ are the defined spectral tristimulus colour matching functions. (k depends on the number of wavelength bands employed in the summation and has no physical significance. It is chosen so that the value of Y gives the luminous intensity in lumens per watt, but k subsequently cancels out in most cases.) In order to separate colour information from intensity, the chromaticity values x, y, and z are used, where:

$$x = \frac{X}{X+Y+Z} \quad \textbf{(2-25)}$$

$$y = \frac{Y}{X+Y+Z} \quad \textbf{(2-26)}$$

$$z = \frac{Z}{X+Y+Z} \quad \textbf{(2-27)}$$

In addition to specifying the colour of a source having a spectral irradiance distribution $S(\lambda)$, it is useful to describe the colour of a surface having a spectral reflectance $\rho(\lambda)$, illuminated by such a source. In this situation, X, Y and Z are calculated by:

$$X = k \sum_{\lambda=380nm}^{780nm} S(\lambda)\rho(\lambda)\bar{x}(\lambda)\Delta\lambda \quad \textbf{(2-28)}$$

$$Y = k \sum_{\lambda=380nm}^{780nm} S(\lambda)\rho(\lambda)\bar{y}(\lambda)\Delta\lambda \quad \textbf{(2-29)}$$

$$Z = k \sum_{\lambda=380nm}^{780nm} S(\lambda)\rho(\lambda)\bar{z}(\lambda)\Delta\lambda \quad \textbf{(2-30)}$$

The luminous reflectance of the surface, ρ, under illuminant $S(\lambda)$ is calculated by:

$$\rho = \frac{\sum_{\lambda=380nm}^{780nm} \rho(\lambda)S(\lambda)\bar{y}(\lambda)}{\sum_{\lambda=380nm}^{780nm} S(\lambda)\bar{y}(\lambda)} \quad \textbf{(2-31)}$$

Since $x+y+z=1$, the coordinates can be completely described by specifying two of the three values; by the adopted convention, chromaticity is described in terms of the x and y coordinates. These coordinates are often plotted on a chromaticity diagram, as described in the following section, as a convenient method of representation.

2.3.3 CIE chromaticity diagram

For simplified representation, the chromaticity coordinates can be plotted on a rectangular grid in the form of a chromaticity diagram, shown in Figure 2-8. When plotted in this format, each colour occupies a particular point on the diagram, given by its x and y coordinates. In a three-dimensional representation, the brightness of each colour, Y, is plotted on the vertical axis, extending out of the page, and all spectral distributions representing the same colour, but different brightness, lie in a vertical line. In a colour representation, where all colours are reduced to the same intensity, this plot collapses down to the two-dimensional representation shown in Figure 2-8.

Monochromatic spectral distributions, when plotted on the chromaticity diagram, make up the horseshoe-shaped curve of a standard CIE chromaticity diagram. This curve is known as the spectrum locus, and the line joining the ends of the locus is called the purple boundary. All possible colours lie within this enclosed area. The dotted triangle shown in Figure 2-8 shows an example set of tristimulus primaries red, blue and green, and all colours that can be matched with varying amounts of these three colours lie within this triangle.[26]

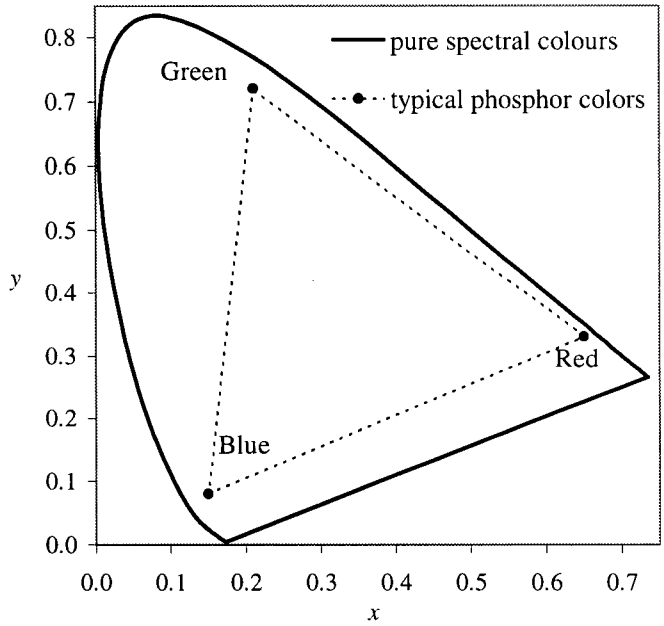

Figure 2-8. Standard CIE chromaticity diagram

Any combination of primaries can be used to define a boundary on the chromaticity diagram. The area enclosed within this boundary is referred to as the colour gamut, as it defines the range of all possible colours that can be matched by adding those primaries in various combinations. Colour gamut is an important specification for many light-emitting or light-reflecting devices, such as cathode ray tube monitors and liquid crystal displays, since the extent of the colour gamut indicates the colour quality of the image. A large gamut means that the colours reproduced by the display can be vivid, so that a wider range of naturally occurring colours can be realistically reproduced.

Although additive colour mixing, as described above, is an important way to produce colour, an important alternative involves subtractive colour employing filters. This is particularly important for a reflective display. For this reason, it will be helpful to review such colour filtering issues in a bit more detail.

2.3.4 Colour filtering

White light contains roughly equal energy contributions from three primaries of the visible spectrum, for instance, red, green and blue wavelength bands. For discussion purposes here, "red light" refers to a spectral distribution with significant contribution of radiation within the red wavelength band, from 580 to 700 nm, and negligible contributions from radiation outside this band. Similarly, "green light" refers to a spectral distribution predominantly within the wavelength band from 500 to 580 nm, and "blue light" within the 450 to 500 nm band. This section compares in more detail the two main methods for mixing colours, additive and subtractive colour filtering.

2.3.4.1 Additive colours

As mentioned previously, there are two approaches for mixing various colours of light. In the additive approach, red, green and blue light are added in a selected ratio to generate the desired colour. The matrix presented in Table 2-1 shows the result of the addition of one part of each of these colours. Obviously, if there is a contribution of red light in the absence of green or blue, the resulting patch of light will be red, and similarly patches of green and blue can be produced in the absence of contributions from the other two sources. Combining two of the additive primaries produces the additive secondary colours, cyan, magenta and yellow. These additive secondaries are also known as subtractive primaries, as explained in Section 2.3.4.2.

Contribution from light sources			Resultant colour
Red	Green	Blue	
0	0	0	Black (K)
1	0	0	Red (R)
0	1	0	Green (G)
0	0	1	Blue (B)
1	1	0	Yellow (Y)
1	0	1	Magenta (M)
0	1	1	Cyan (C)
1	1	1	White (W)

Table 2-1. Additive colour filtering

The six colours red, green, blue, yellow, magenta and cyan are considered to be standard colours for full-colour light-emitting or light-reflecting devices. Black and white, while not strictly considered to be colours, are important to denote the absence or presence of all wavelengths in the visible spectrum. As described in the discussion of chromaticity coordinates in Section 2.3.3, varying the amounts of red, green and blue light can produce any desired colour within the available gamut. The saturation level of these three individual colours determines the achievable gamut for a particular set of primaries.

For reflective displays, the additive method, while an effective method for generating colours, tends to be inefficient since the red, green and blue contributions are produced by filtering the light from a broadband source, such an incandescent or tri-stimulus phosphor fluorescent bulb, with filters having the appropriate spectral transmittance characteristics. As a result, a significant fraction of the light (in each case, approximately two thirds) is absorbed by the filters, and therefore the brightness of the resultant colour is substantially limited.

2.3.4.2 Subtractive colours

The other approach for mixing colour, subtractive colour filtering, has greater relevance to this thesis. Rather than using red, blue and green filters to mix light, this system uses primary subtractive colour (cyan, magenta and yellow) filters. As mentioned in Section 2.3.4.1, these subtractive primaries are also known as additive secondary colours since they can be produced by adding two of the three additive primaries, red, green and blue. A filter with a spectral transmittance characteristic consistent with cyan absorbs wavelengths in the red band and transmits in the blue and green bands. Similarly, magenta absorbs wavelengths in the green band while transmitting in the red and blue, and yellow absorbs wavelengths in the blue band while transmitting in the green and red. Ideal transmittance characteristics for such filters are shown in Figure 2-9.

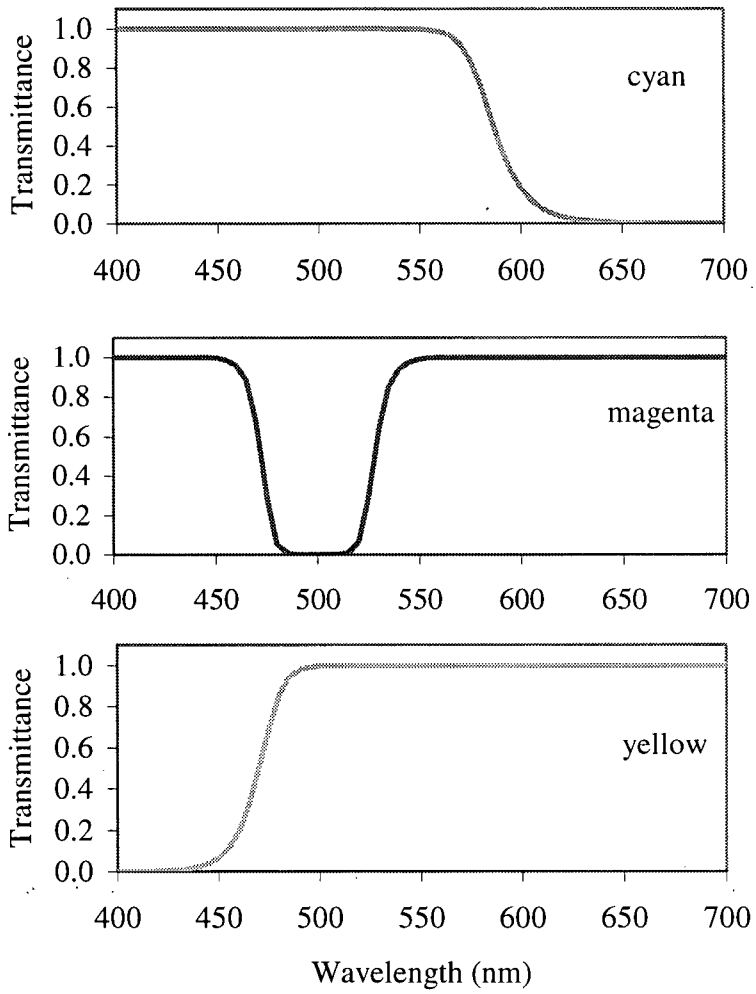

Figure 2-9. Ideal transmittance characteristics for subtractive colour filters

Subtractive filtering can produce the same colours as the additive method, by appropriately subtracting various permutations of red, green and blue. For instance, the addition of pure green and blue light (cyan light) is spectrally equivalent to the subtraction of the contributions of red light from the visible spectrum (by a cyan filter). Table 2-2 demonstrates the filter combinations required to produce the six standard colours, as well as white and black.

Contribution from filters			Resultant colour
Cyan	Magenta	Yellow	
0	0	0	White (W)
1	0	0	Cyan (C)
0	1	0	Magenta (M)
0	0	1	Yellow (Y)
1	1	0	Blue (B)
1	0	1	Green (G)
0	1	1	Red (R)
1	1	1	Black (K)

Table 2-2. Subtractive colour filtering

Again, the achieved gamut is determined by the spectral quality of the filters, and all colours within the gamut can be achieved by partially filtering the light appropriately. Typically, the gamut for a colour filtering system using additive colours is defined by a triangular boundary, since the colours combine linearly. However, with subtractive colour filters, the effect is multiplicative rather than additive. As a result of this non-linear behaviour, the boundary will be defined by the six standard colours, rather than just three. A typical gamut for a device using subtractive colour filtering, shown in Figure 2-10, occupies a region of the chromaticity diagram bounded by the coordinates of the six standard colours.

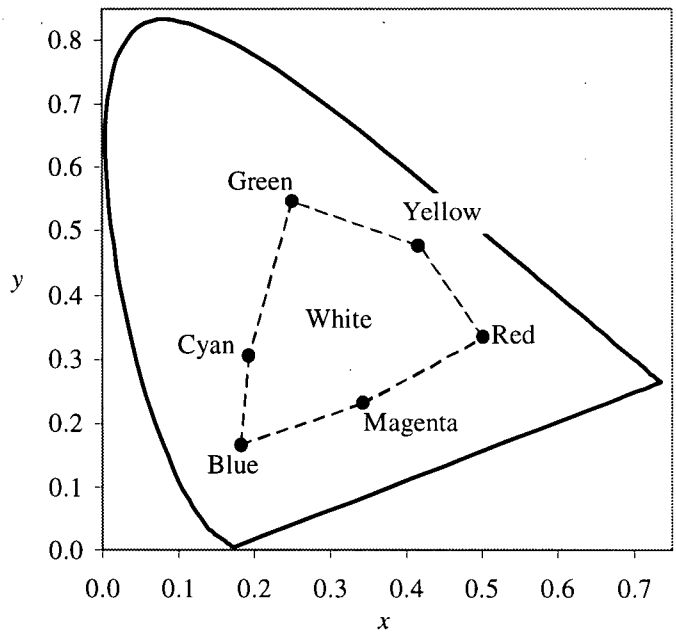

Figure 2-10. Colour gamut of a device based on subtractive colours

By appropriately filtering white light with selected densities of cyan, magenta and yellow filters, any desired colour within the allowable range can be generated. Spectrally, this gives the same result as the additive method, however in some circumstances this method can be much more efficient.

Specifically, for reflective displays, additive colour mixing requires segmenting the display, on a microscopic scale, into "red", "green" and "blue" pixels, each of which absorbs a minimum of two thirds of the incident light. Thus, the maximum reflectance in the white state is about 1/3. In contrast, with subtractive filtering, the filters are placed on top of one another, so colour pixelization is not required, and the white state has a potential reflectance approaching 1. In Chapter 3, a new approach to colour mixing is presented in which a hybrid of these two concepts yields an intermediate maximum potential reflectance of 2/3. This approach involves coloured pigments suspended in a liquid to filter reflected light. For this reason, the behaviour of particles in suspension will be discussed in the next section.

2.4 Particle suspensions

Suspensions of small particles in fluids are used in a wide variety of applications. For instance, drug delivery systems use suspensions to allow the proper dosage and release of drugs in a person's body. Photocopying and printing techniques use liquid toners, in which the pigments used to print the image are suspended in a liquid. The food industry uses particle suspensions for the preparation and preservation of many food items. These wide-ranging applications have supported a great deal of research in the field.

The term "colloid" is often used to describe suspended particles in the size range from about 0.1 to 100 μm. Usually these particles become electrostatically charged when they are suspended in a liquid, and there are a number of mechanisms by which the particles can become charged. For instance, the preferential adsorption of ions in solution can result in an electrical charge on the particle surface. The dissociation of chemical groups on the surface can also result in a charge. In some cases, substitution of surface groups can be responsible for the charge. The existence of such a surface charge is crucial in many applications, including the research described in this thesis. However, the specific charging mechanism(s) are often not known in detail. Fortunately, however, the magnitude of the charge is fairly

easy to determine, as discussed in Section 2.4.2, and the fact that the precise origin of the charge is unknown is seldom a problem.

Since the suspension must have an overall neutral charge, for each unit charge residing on the particle surface, there must be corresponding opposite unit charge in solution. Typically a colloidal particle will have a charge equivalent to many electrons, and the countercharges reside on ionic species present in the fluid. It is common to have orders of magnitude more counterions than particles present in the suspension.

For the purpose of discussion in this section, the particle is considered to be positively charged, and the counterions negatively charged. These small counterions will be attracted, by electrostatic force, to the region near a particle, forming a cloud of negative charge around the positively charged core. In this region, known as the electrical double layer, the inner layer is considered to have a surface charge consisting of the charges adhering to the particle, as well as the counterions very close to the particle surface. In such close proximity, the electrostatic force is very high, therefore overcoming the thermal motion of the counterions and binding them tightly to the particle. These counterions move with the particle, and form what is known as the Stern layer. In the outer or diffuse region of the double layer, the electrostatic force is reduced and becomes comparable to the force due to the thermal motion of the counterions. These counterions tend to remain near the particle, but are not bound to it.[27]

One common method of characterizing these particles refers to the potential, Φ, at different points within the double layer, relative to the potential at a distant point in the bulk, well outside the influence of the particle and its associated counterions. Typically, for a particle of radius a, the surface potential is denoted Φ_o, and the potential tends to zero in the bulk, as in equation (2-32).

$$\Phi = \frac{a\Phi_o}{r} e^{-\kappa(r-a)} \qquad \textbf{(2-32)}$$

The Debye length, $1/\kappa$, is given as the distance from the particle surface at which Φ has dropped by a factor of 1/e. This is typically considered to be the "thickness" of the double layer. If the Debye length is very short, then the diffuse layers of two neighbouring particles

are unlikely to interact, and the particle behaviour can be predicted using some relatively straightforward analysis models. In suspensions with long Debye lengths, the diffuse layers may overlap substantially, complicating the particle interactions.[28]

A particular value of potential, known as the zeta potential, ζ, is often cited as an important characteristic of a colloidal particle. When an externally applied force acts on a particle and causes it to move, some of the surrounding counterions will move with it. The potential at the radius within which the counterions move with respect to the solvent is defined as the zeta potential. This value is close to, but not exactly, the Stern potential. While the zeta potential is not directly measurable, it is considered to be a useful parameter for determining the electrokinetic behaviour of the particle[29], as described in Section 2.4.2.

The initial step in formulating a stable suspension of particles in a liquid medium requires that the net buoyancy force be sufficiently low that the particles are likely to remain at an equilibrium position in the suspension, rather than sinking or floating due to gravity. This net buoyancy force acting on the particle is the difference between the weight of the particle and the buoyant force of the liquid acting on the particle. This settling force, F, can be written in terms of the densities of the particle, ρ_p, and the surrounding liquid, ρ_l, and the volume of the particle, V.

$$F = g(\rho_p - \rho_l)V \tag{2-33}$$

The energy associated with this settling force is then $hg(\rho_p - \rho_l)V$, where h is the relative position of the particle within the suspension. The settling can be counteracted by provided that this settling energy is much less than the thermodynamic energy kT:

$$hg(\rho_p - \rho_l)V << kT \tag{2-34}$$

This implies that small particles, with a density closely matched to that of the surrounding medium, are most likely to yield stable suspensions.

To further improve the stability of a colloidal suspension, to prevent both settling and particle aggregation, either electrostatic or steric stabilization methods can be employed. Using electrostatic stabilization, particle aggregation is reduced or eliminated by electrostatic

repulsion.[30] Steric stabilization, on the other hand, requires a molecular dispersant mechanism. Typically, this involves adding a substance consisting of molecules that, on one end, chemically favour the particle and therefore attach to it, and on the other end, have an affinity for the liquid and readily dissolve. The result is that the dispersant molecules arrange themselves around the particle, and suspend it within the fluid. Further, these solvated molecules surround the particle and provide an excluded volume to prevent the approach of another particle.[31] In some suspensions, it is both possible and desirable to incorporate both stabilization methods. The choice of method usually depends on the suspension components and formulation process.

The behaviour of a particle in suspension depends in part on the properties of the fluid in which it is suspended. In the next section, a comparison is made between particles suspended in high dielectric and low dielectric constant fluids.

2.4.1 High dielectric and low dielectric constant media

The behaviour of particles suspended in relatively high dielectric constant (most often aqueous) liquids is fairly well understood. It stands to reason that these systems have been well studied, since biological systems based on water, as well as substances that interact with biological systems, are so important. The behaviour of particles suspended in low dielectric constant liquids, such as the perfluorinated hydrocarbon particle systems described in this thesis, are much less well understood.

The Debye length of the counterion cloud depends on both the dielectric constant and the ionic strength of the surrounding fluid. In aqueous systems, where the dielectric constant is relatively high, the electrical double layer tends to be very thin. This means that in order to characterize various particle parameters, such as diameter, charge and electrophoretic mobility, the suspension can be modeled as a system of non-interacting particles. On the other hand, in low dielectric constant fluids, the electrical double layer extends a long distance into the suspension. In these suspensions, characterization of the particle parameters is far more complicated, since the interaction of many neighbouring particles must be taken into account.[32]

The understanding of particles in low dielectric constant media is becoming increasingly important in many fields, including the development of paints, inks and toners[33], and the study of oil and fuel systems.[34] The research described in this thesis does not attempt to further the understanding of charging mechanisms and particle characterizations in perfluorinated hydrocarbon liquids. However, these issues are important to bear in mind when dealing with these systems, as it is necessary to recognize the complex behaviour of particles in these systems and to apply the principles and analysis methods of particle characterization judiciously.

As previously mentioned, the significance in this thesis of the electrostatic charge of the colloidal particles is that they can be moved by an applied electric field. This controlled motion, known as electrophoresis, is discussed in further detail in the following section.

2.4.2 Electrophoresis

Electrophoresis refers to the motion of electrostatically charged particles in response to an applied electric field. Under typical moderate applied field strengths, the drift velocity, v, of a particle is linearly proportional to the electric field strength, E. The constant of proportionality is known as the electrophoretic mobility, μ:

$$v = \mu E \tag{2-35}$$

For a given particle, the mobility value depends on its net electrostatic charge, q_{net}, and its effective hydrodynamic radius, a_{net}. The exact relationship between overall charge, radius and mobility of particles in a low-dielectric medium is complicated, as a result of the interactions of the extended double layers. However, when the particle is moving at constant velocity under the influence of an applied field, the relationship can be approximated by equating the electrostatic force, F_e,

$$F_e = q_{net} E \tag{2-36}$$

to the drag force on a spherical particle, F_s, given by Stokes' equation[35],

$$F_s = 6\pi\eta a_{net} v \tag{2-37}$$

where η is the viscosity of the fluid.

Combining equations (2-35), (2-36) and (2-37), the mobility is given by

$$\mu = \frac{q_{net}}{6\pi\eta a_{net}} \tag{2-38}$$

which is proportional to the ratio q_{net}/a_{net}, which is in turn approximately proportional to the zeta potential. Therefore, measurement of the electrophoretic mobility provides key information about the particle. In particular, since the zeta potential is approximately:

$$\varsigma \cong \frac{q_{net}}{4\pi\varepsilon a_{net}} \tag{2-39}$$

where ε is the permittivity, combining with (2-38) yields the relationship:

$$\mu \cong \frac{2\varepsilon\varsigma}{3\eta} \tag{2-40}$$

which is felt to be valid even for the more complex case of low dielectric constant fluids.[36]

As reported in detail in later chapters, this research program investigated electrophoresis as an appropriate control mechanism for frustrating TIR with pigment particles. Clearly, such a use of electrophoresis requires characterization of the colloidal properties. It is therefore helpful to briefly consider the various electrokinetic techniques used to characterize various particle parameters, as discussed in the next section.

2.4.3 Particle characterization

There are many methods for characterizing various particle parameters, such as size and electrostatic charge. This section briefly describes two standard characterization methods that were implemented during the course of this research. Both analysis methods are typically performed using dedicated commercial instruments.

One method employed in this work uses an electroacoustic method to measure electrophoretic mobility, in which a high frequency alternating electric field is applied across

a sample of the suspension and the particles move electrophoretically in response to the applied field. Provided a density difference exists between the particles and the suspension medium, this motion causes an alternating acoustic wave. Measurement of the electrokinetic sonic amplitude as a function of frequency, compared with a calibrating measurement of standard suspensions, yields a value of electrophoretic mobility.[37] Under the proper conditions, reasonable values of the mobility can be achieved using this approach. However, in the absence of a properly calibrated standard, these measured values are considered to be unreliable and, for this reason, alternate methods will be used to obtain reasonable estimates of the mobility.

A different method, known as dynamic light scattering, can be used to measure the particle size distribution. In this technique, two laser beams intersect and form interference fringes in a dilute sample of the suspension. As a particle moves through the fringes by diffusion, it scatters light with an intensity that fluctuates with a frequency distribution related to its diffusion rate. The scattered light is analyzed to give a frequency spectrum from which the particle mobility distribution is calculated. Since the particle mobility is related to the size of the particles, this can be translated into the particle size distribution.[38]

Both of these are effective methods for characterizing particles in aqueous solutions. However, as with other particle characterization methods, the interpretation for particles in a non-aqueous medium is more difficult. As a result, these measurements can only be considered rough estimates for particles in non-aqueous media.

In this chapter, a number of principles relating to a new reflective image device technology have been discussed. In order to assess this technology in context, it will now be helpful to compare devices that are currently commercially available or under development. For this reason, these current technologies are described in the following section.

2.5 Current display technologies

At the moment, there are a number of reflective image display technologies; some of these are commercially available while others are in the development stage. Each of these display technologies has different advantages and disadvantages, and it will probably be the case that

some will be better suited to some applications that others, and a diverse set of technologies will be required to fulfill all needs in this field.

2.5.1 Liquid crystal displays

Liquid crystal displays (LCD's) are by far the most common reflective display. They use a thin layer of liquid crystal material to control the reflectance of a surface. Liquid crystals represent an unusual phase of matter since, unlike typical liquids with randomly oriented molecules, their molecules exhibit some degree of orientational alignment. In descriptions of the behaviour of these molecules, their preferred orientation direction is often represented by an arrow, called the director. Depending on the substance itself and the environmental conditions, a liquid crystal can take one of a number of phases, and a few of these will be briefly described here.

Perhaps the most straightforward phase is the nematic liquid crystal phase, in which the molecules orient parallel to one another and the director points in a uniform direction across the sample. In a second phase, known as the chiral nematic liquid crystal phase, the director rotates through the sample, forming a helical pattern. (Substances forming this phase are often called cholesteric liquid crystals, since the most common examples of these materials are associated with cholesterol.) Smectic liquid crystals represent a third phase and these molecules are observed to have some degree of positional, as well as orientational, alignment, since they tend to arrange into distinct layers. For the purposes of this brief review, it is not necessary to provide a detailed discussion of the properties of these materials. However, it is important to note that in all of these phases, an anisotropy results from the preferred orientation of the molecules, particularly in terms of the interaction of light with these materials.

In an image display device, a thin layer of liquid crystal material is typically contained in a gap between two glass plates. An electric field applied across the gap causes the permanent or induced dipoles in the liquid crystal molecules to orient with the dipole axis parallel to the field, and therefore the director will orient with respect to the field. Although the director is typically free to point in any direction in response to a field, there are a number of ways in which it can be controlled. Before the gap is filled with liquid crystal, the inner glass

surfaces can be prepared by a number of methods, for instance, rubbing with a cloth or applying a chemical film, to cause the director to align in a particular orientation. In this case, near the surface, the director is constrained and cannot respond to an applied electric field. Toward the center of the gap, however, the director can orient with respect to the field. This results in an induced deformation of the liquid crystal across the gap, which can substantially affect the way in which light interacts with the material, specifically in terms of the polarization of the light. For illustrative purposes, the discussion presented here will describe the interaction of polarized light with a nematic liquid crystal sample having a uniform director.

Polarization is a characteristic of light that describes the direction of the electric and magnetic fields comprising the wave. For instance, linearly polarized light is a special case in which the electric field points in a single direction. The anisotropy of a nematic liquid crystal resulting from the orientational alignment causes light that is linearly polarized parallel to the director to propagate at a different velocity than light that is linearly polarized perpendicular to the director. As a result of the behaviour, it is useful to consider, for this discussion, that light is a combination of these two linear polarizations.

These two polarization components travel through a slab of nematic liquid crystal material at two different velocities, and therefore emerge from the material with a phase difference that is proportional to the thickness of the material. Thus, the orientational alignment of a liquid crystal affects the change it imparts to the polarization of incident light, which is why they are so useful in image displays.

Linearly polarized light can be produced by passing unpolarized light through a polarizing material that almost completely absorbs one polarization while allowing the other polarization to pass through fairly efficiently. If two such polarizing filters are layered with perpendicular polarization directions (in an arrangement known as crossed polarizers), very little light will pass through since the linearly polarized light emerging from the first polarizer will be absorbed by the second. The insertion of an isotropic material between the two polarizers will have no effect on the transmission of light since the polarization of the light is unchanged as it passes through such a material. A liquid crystal material inserted in this region, however, changes the polarization state such that some of the light will transmit

through the stack. The application of an electric field across the nematic crystal can deform the crystal structure to change this anisotropy. In this manner, the amount of light that passed through the stack can be controlled.

In many display applications, a liquid crystal is used in which the director rotates about an axis in a helical fashion. This can be achieved, for instance, by fixing the directors on the glass surface, and therefore forcing the liquid crystal to twist along the direction perpendicular to the surfaces. The interaction of light with these twisted structures is analogous to that of the nematic crystal just described. However, in this case, it is more appropriate to characterize the light in terms of right- and left-circularly polarized components. The helical path followed by the director causes these two components to travel at different velocities through the material, and one possible result is that linearly polarized light can emerge, with a polarization axis that depends on the thickness of the sample. Again, this anisotropy can be controlled by further deforming the crystal structure by an applied electric field.

Liquid crystals can be used in two primary types of image displays, namely transmissive and reflective. Transmissive displays are constructed by stacking the appropriate polarizing filters and liquid crystal material, and they glow because they incorporate a backlight to direct light through this liquid crystal panel toward the viewer. In the bright state, the molecules are oriented so that light passes through the panel. In the dark state, the light is absorbed, and the region looks dark. To generate each of these states, the anisotropy of the liquid crystal material is changed by the application of an applied electric field.

The reflective configuration is similar, but includes a polarization-preserving rear reflector instead of a backlight. In this case, the bright state again allows polarized, ambient light to pass fairly efficiently through the layers, where it reflects from the rear reflector, and passes again through the panel to return to the viewer. In the dark state, the light is absorbed, creating a dark appearance. These passive displays rely on the ambient lighting conditions, rather than a backlight, for the image on the display to be visible.

A full-colour image can be generated in both the reflective and transmissive display configurations, typically using the additive colour filtering approach described in Section

2.3.4.1. This approach uses a filter overlay, which divides each pixel into three subpixels of blue, green and red. The brightness of each subpixel is determined by the amount of light reflecting from (or passing through) the liquid crystal assembly in the region beneath each filter subpixel, so the contributions of each colour within an individual pixel is controlled, generating a complete gamut of colours. This additive technique means that with intensely coloured filters, the maximum reflectance is only one third of that of the equivalent monochrome display. In many reflective displays available in the market today, unsaturated colours are used to enhance the overall brightness at the expense of a reduced colour gamut.

As mentioned above, transmissive liquid crystal displays yield bright, colourful images by illuminating the display with a high intensity backlight. This is a visually effective technique, but because of the substantial power consumption of the backlight, it is inappropriate for low power, battery-operated device applications. Reflective displays, on the other hand, can operate on low power since they reflect the ambient light, but the maximum reflectance of such displays is quite limited. In theory, a monochrome LCD display is at most 50% reflective since at least half of the ambient light must be absorbed by the polarizer. In practice, the maximum reflectance of a typical monochrome reflective display is only 34% [39], and this value drops to at most 16% for a full-colour reflective liquid crystal display.[40] A powerful frontlight is sometimes used to illuminate this display surface for improved legibility, but again this drastically increases the power required to operate the device.

The technique for achieving a full-colour reflective image device based on TIR, as described in this thesis, provides a number of possible advantages over current liquid crystal displays. The most important advantage is a four-fold improvement in the reflectance, which results from the elimination of the polarizer and the use of subtractive colour filtering.

2.5.2 Cholesteric liquid crystal displays

A number of organizations are currently exploring the use of cholesteric liquid crystal materials to produce full-colour reflective images.[41,42,43] Displays based on this approach may have some advantages over conventional liquid crystal displays in terms of brightness,

viewability and power consumption. Given these potential advantages, it is worthwhile here to briefly describe their operation.

As discussed briefly in the previous section, cholesteric or chiral nematic liquid crystals are capable of switching between two different alignment states. In particular, in one state they are capable of selectively reflecting incident light within a narrow wavelength band, since constructive interference occurs when the pitch of the helical structure, or the distance required for one complete rotation, is equal to the effective wavelength of the light in the material. (Constructive interference occurs when the material properties repeat themselves over a distance equal to half the wavelength of light. In this case, although the pitch is defined as the distance required for one complete rotation of the director, the helical structure repeats itself twice in each pitch cycle.) Wavelengths of light outside this band transmit through the material. As a result, panels containing a thin layer of a cholesteric liquid crystal can be used as a filter to reflect a desired colour and transmit the rest of the light in the visible band. These molecules can also be bistable, since once the desired state is achieved, it will remain fixed when the applied voltage is removed. Such bistability offers the potential of a very low power device since the voltage need not be constantly applied.

Various configurations are used to generate reflective images using cholesteric liquid crystals. In perhaps the simplest example, three liquid crystal panels are stacked over a black absorbing background material. The liquid crystal material contained in each panel is chosen and tuned to reflect one of three specific wavelength bands, for instance, blue, green or red, and such reflected light is circularly polarized in one direction only. The combination of all three coloured filters, along with the black background, allows the eight standard colours to be generated, as discussed in terms of additive colour filtering in Section 2.3.4. The reflectance of the surface can be further increased by stacking an additional set of blue, green and red filters, reflecting light with the opposite circular polarization.

In theory, this type of structure can yield a maximum reflectance of nearly 100% and achieve a reasonably large colour gamut. In practice, however, there are significant losses, costs, and resolution problems associated with such a stacked structure. Typically, the maximum reflectance of current prototypes is only 35%.[44]

2.5.3 Electrophoretic image displays

A number of previous research efforts have been aimed at developing an image display using electrophoresis of pigment particles, in a substantially different optical principle than the approach presented in this thesis. The previous approach used pigment particles suspended in an opaque liquid. In one state, the particles were moved against the viewing surface, hiding the liquid, and therefore giving the viewing surface the appearance of the colour of the particles. In the other state, the particles were moved away from the viewing surface, so that they were hidden from view so the surface would take on the appearance of the opaque liquid.[45,46,47,48]

A number of organizations tried to commercialize displays based on this principle but were ultimately unsuccessful because of problems caused by particle migration. Such designs require the particles to move a substantial distance (typically greater than 100 μm) away from the viewing surface so that they would be sufficiently hidden from view by the opaque fluid. It was observed that when such particles moved long distances in the fluid, they tended to cluster together after repeated cycling of the applied electric field, thus degrading the image quality.[49] This particle clustering behaviour is described in further detail in Section 3.11.

Recently, a technique has been established that makes the use of an electrophoretic suspension more practical in a display. [50,51,52] This method, known as micro-encapsulation, prevents particle migration by confining the suspension within a very small volume. The primary method of this new generation of electrophoretic image displays uses a suspension of particles in a coloured fluid, contained in polymeric microcapsules having a diameter of about 100 μm. The basic operation is the same as that of a conventional electrophoretic image display, where the two states are generated either by moving the particles toward the front viewing surface of the capsule, or drawing them to the non-viewing side, thereby hiding them behind the opaque fluid. However, since the particles are confined within the microcapsules, they cannot drift over time to form the particle clusters. This is a fairly new technique, but current results indicate that this approach will substantially reduce and possibly eliminate particle migration problems.

The TIR-based approach presented in this thesis is a fundamentally different use of electrophoresis. Perhaps the most important difference is the maximum reflectance level. In the microcapsule approach, scattering of ambient light typically causes the reflection from white titanium dioxide particles that are moved toward the viewing surface. These particles scatter light approximately equally in all directions, resulting in a diffuse appearance. This is an advantage in terms of the viewing angle of the image, but it reduces the maximum reflectance of the surface. Prototype devices using this technique have demonstrated a maximum reflectance of at most 40%.[53] In contrast, the TIR approach has demonstrated a maximum reflectance of nearly 100%, although this is true only for a somewhat limited range of viewing angles.

A second important distinction is the distance that the particles must travel in order to alter the reflectance state. Instead of moving about 100 μm, as mentioned above, in the TIR-based approach the particles need only move less than 1 μm to shift from outside to inside the evanescent wave zone. For particles having about the same electrophoretic mobility, this implies a substantially reduced transit time required for switching between the reflective and absorptive states. As will be explained in detail in Chapter 3, the encapsulation approach can also be used in a TIR-based reflective image device by taking advantage of the microstructured geometry of the reflective sheets.

In comparison with some current reflective image display technologies, it is apparent that the technique based on total internal reflection has some possible advantages, particularly in terms of its potential to generate a bright, colourful image. Having briefly introduced the background information associated with this study, it is now appropriate to discuss this new optical system in more detail.

3 DESIGN ISSUES IN A NOVEL TIR-BASED DISPLAY

As described in the previous chapter, TIR can be frustrated by scattering or absorbing the electromagnetic energy in the evanescent wave. Presented in this chapter are the key conceptual issues that were identified in the initial feasibility research regarding a possible TIR-based reflective image device.

3.1 Principle of a TIR-based reflective display

The principle of reflectance modulation using frustrated TIR can be demonstrated using a simple device, shown in Figure 3-1, based on the linear prismatic structure depicted in Figure 2-6. In this device, a polycarbonate microstructured sheet, with refractive index of n_1=1.59, is separated by a thin air gap, with refractive index n_2=1.0, from a black absorber. In the reflective state, a light ray, shown in the left-hand portion of Figure 3-1, enters the prismatic sheet at normal incidence, undergoes TIR at each prismatic facet and exits the sheet at 180° to the incident ray. By moving the absorptive material into optical contact with the prismatic rear surface of the sheet, as shown in the right-hand portion of Figure 3-1, the majority of the incident light is absorbed at the first prismatic facet, and any light reflecting from this surface is further absorbed at the second facet, resulting in almost complete absorption of the light and elimination of reflection. Removing the absorber from the surface to create the thin air gap completely restores the reflection, thus allowing control of reflectance. Clearly, an absorber that can conform in some manner to the microstructured surface will most effectively frustrate the TIR.[54,55]

This optical switching technique has three novel features, which will be discussed in detail in later sections. First, the prismatic geometry of the microstructured sheet redirects a substantial fraction of the ambient light in a typical luminous environment, resulting in a highly reflective surface. Second, since the evanescent zone is microscopically thin, only a very small movement of the absorber is required to switch between the highly reflective and highly absorptive states. Third, the prismatic geometry allows a unique approach to subtractive colour filtering to yield a full-colour image. As a result, this display has a large

reflectance difference and has the potential to be switched quickly with a small amount of energy per unit area.

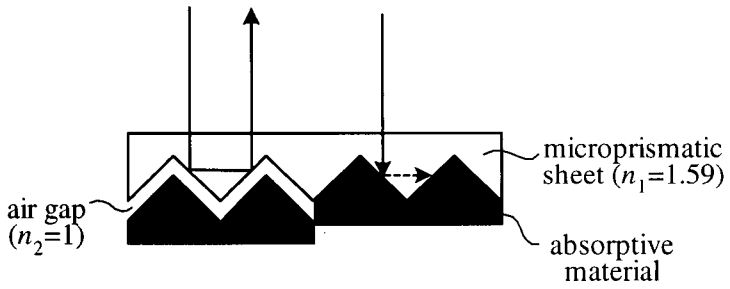

Figure 3-1. Principle of a TIR-based reflective image device

There are a number of possible methods for actuating this type of reflective image device. In one approach, an array of tiny, individually controlled micro-mechanical elements could move the absorber into and out of optical contact with the TIR surface. However, such micro-mechanical approaches are currently very expensive, and are not likely to be practical for use in the near future in an image display, especially for high-resolution images. Another method uses an array of pneumatic valves to force, by means of air pressure, specific regions of an elastomeric bladder into surface contact.[56] In these regions, the elastomer will conform to the microstructure to frustrate TIR. This method is also impractical because the pneumatic control requires an air compressor, and it is limited to rather low-resolution displays. A more promising actuation method would use electrostatic force, caused by an applied electric field, to controllably move the absorber into contact. Since the electric field can be applied to selected regions of the display by standard microelectronics methods, the resolution of the resulting image can be very high. There are several absorbing materials that can be moved into contact with the TIR surface under electrostatic force, and some of these methods can operate at sufficiently low voltage to make them practical for a small, battery-operated device. This will be discussed in further detail in Section 3.5, but first it will be helpful to consider in more detail certain material constraints for TIR.

3.2 Index mismatch requirements

As follows from its definition in (2-8), the critical angle decreases as the ratio of n_1/n_2 increases. As a result, a large index mismatch between the prismatic material and the medium at the interface means that a large angular range of light rays will exceed the critical angle and undergo TIR. Therefore, to achieve reflection for the largest possible fraction of the incident flux, it is desirable to maximize the ratio of n_1/n_2 for a reflective display. Figure 3-2 demonstrates schematically that the fraction of incident light rays that undergo TIR depends on the refractive index ratio. Figure 3-2(a) shows that for a relatively low ratio of 1.05, the critical angle is quite high so that only the rays at glancing incidence are reflected. A much larger ratio of 2.00, as shown in Figure 3-2(b), causes many of the incident rays to be reflected. A ratio equal to 1.59, as illustrated in Figure 3-1, is achieved with a polycarbonate/air interface, and it works quite well for a reflective image device.

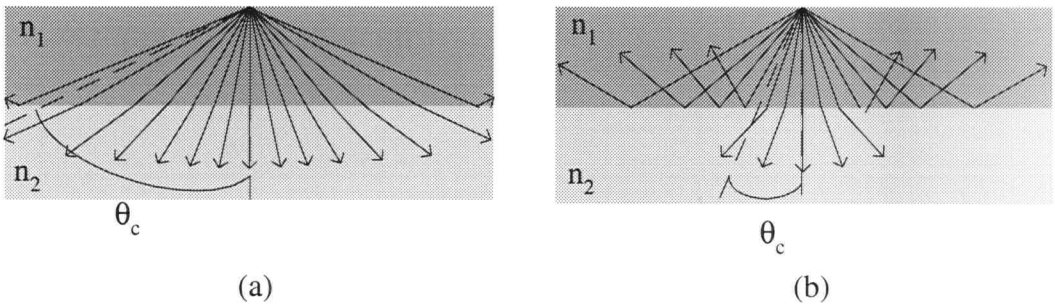

Figure 3-2. Light rays at an interface with index ratio of (a) 1.05 and (b) 2.00

Clearly, a significant refractive index ratio at the interface is an important feature of a reflective image device based on TIR. As will be discussed at length in Section 3.6, this ratio can be effectively enhanced by taking advantage of a unique optical property of the linear prismatic structures used throughout this study. In the meantime, it is important to consider certain mechanical issues concerning the contact with the absorber, particularly in terms of the surface energies involved.

3.3 Surface energy considerations

In the reflectance device described schematically in Figure 3-1, TIR occurs in a polycarbonate sheet having index n_1=1.59, and is frustrated by a conformable absorber

moving in air. Although this system works quite well optically, there are undesirable surface energy effects associated with the motion. This section describes this complication in terms of the energy required to initiate and eliminate optical contact in order to estimate the power per unit area required to drive the device.

It is useful to consider a typical numerical example. Consider a $1x10^{-6}$ m thick sheet of conformable absorbing material, such as a carbon-loaded silicone elastomer, oscillating with an amplitude of $1x10^{-6}$ m so that it moves substantially into and out of the evanescent wave at a frequency of 30 Hz. A sample of this membrane, with a typical density of about $1x10^{3}$ kgm^{-3}, has a mass per unit area of 10^{-3} kgm^{-2}, a maximum speed of $1.9x10^{-4}$ ms^{-1}, and therefore a maximum kinetic energy per unit area of $1.5x10^{-11}$ Jm^{-2}. Since this energy must be imparted twice per cycle, this represents a mechanical power requirement of about 10^{-9} Wm^{-2}. Clearly, this movement can be created with a very small amount of power.

Unfortunately, the energy per unit area associated with the physical contact between the membrane and the surface at which TIR occurs is typically greater than 10^{-2} Jm^{-2}, nine orders of magnitude greater than the mechanical energy associated with the oscillation![57] Clearly, in a practical device based on frustrated TIR, the absorbing material should not make physical contact with the interface since it requires too much energy to remove it.

For this reason, in the course of this study, the use of liquid as the second medium was investigated as a method of effectively lubricating the TIR surface to prevent direct physical contact by the absorbing material. This is best considered in terms of the surface energies at the interfaces. These are σ_{LA}, the surface energy of the interface between the liquid and the absorber, σ_{LS}, the surface energy between the liquid and the TIR surface, and σ_{AS}, the surface energy between the absorber and the TIR surface. If the surface energy of the absorber-TIR surface interface is greater than the sum of the liquid-absorber and liquid-TIR interfaces, in other words,

$$\left|\sigma_{AS}\right| > \left|\sigma_{LA} + \sigma_{LS}\right| \qquad \textbf{(3-1)}$$

the liquid will spread in a thin layer between the two materials. This means that, in such a case, it is energetically favourable for a very thin layer of liquid to remain between the solid surfaces rather than for the liquid to entirely flow out so the two solids make direct contact. This results in the reduction or even elimination of adhesion between the absorber and the TIR surface, and greatly reduces the energy required to drive the device. It has long been recognized that a liquid lubricant can reduce or eliminate problems associated with friction or sticking between solid parts, however this research, we believe, represents the first time this solution has been applied to facilitate the controlled frustration of TIR by a solid absorbing material.

In summary, surface energy considerations make a solid-liquid interface very desirable for a controlled TIR device. However, the presence of the liquid substantially changes the optical properties at the interface, and these new optical requirements must be taken into account to ensure that TIR can still happen. This issue is the subject of the following section.

3.4 Optical requirements for TIR at a solid-liquid interface

TIR is more difficult to achieve at a solid-liquid interface because the index of refraction of a typical liquid is much greater than that of air, and thus the refractive index ratio is substantially lowered. To maintain the required ratio, the index of the micro-prismatic material could be increased. However, while progress is being made in the area of micro-replication of high index materials, it is not possible at the present time to obtain optically precise, high index microstructures. For good optical quality microstructures, the maximum refractive index is currently limited to that of polycarbonate, at n_1=1.59.

As an alternate solution, a search was carried out for low-index fluids that are compatible with electronic device requirements. Most such liquids have an index of greater than 1.4 and are therefore unsuitable for use in a high reflectance TIR device. Eventually, perfluorinated hydrocarbon liquids were identified as a promising candidate because they have a very low index of refraction of 1.276, high optical transmission (the coefficient of absorption is substantially less than 1 m^{-1}), and very good electrical properties (the typical dielectric constant is less than 2, and dielectric strength greater than 10^7 Vm^{-1}). Table 3-1 compares the

critical angle for a few liquids in contact with a polycarbonate surface. Clearly, the perfluorinated hydrocarbon liquid provides a substantial reduction in index over oil and water. However, the index ratio is still limited to about 1.25. As will be addressed in the next section, the index ratio enhancement feature described in Section 2.2.2 can be employed to make this a practical system.

Liquid	n_2	n_1/n_2	θ_c
Hydrocarbon oil	1.5	1.06	70.6°
Water	1.33	1.19	57.2°
Perfluorinated hydrocarbons	1.276	1.25	53.4°

Table 3-1. Critical angles at typical liquid/polycarbonate interfaces

Perfluorinated hydrocarbon liquids are composed of hydrocarbon chains in which the hydrogen atoms along the chain have been replaced by fluorine atoms. Fluorine atoms are highly electronegative, light and small (although larger than hydrogen atoms) and they can normally replace any hydrogen atom in a linear or cyclical organic molecule, forming a very short, strong carbon-fluorine bond. The strength of this bond makes perfluorinated hydrocarbons very stable, inert and resistant to breakdown against a wide variety of chemicals and temperature ranges. These liquids tend to have low refractive index as a result of the strong bonds, since the electronic orbitals cannot shift as easily in response to the field, thereby lowering the polarizability of the fluid and hence the index.

Of particular interest in this thesis is a family of perfluorinated hydrocarbon liquids sold under the tradename Fluorinert™, a product of the 3M Company. One of these commercially available fluids, FC-75[58] has the molecular formula $C_8F_{16}O$ and is particularly well suited to this application.

A detailed list of the physical and electrical properties of Fluorinert™ FC-75 is provided in Appendix C. The following section describes how these unique low index liquids can be used with polycarbonate microstructures in the development of a practical device.

3.5 Possible absorbers used to frustrate TIR

A number of possible absorbers were evaluated for frustrating TIR in a liquid medium. One candidate was a porous or channeled elastomeric structure that would conform to the surface (while being lubricated by the perfluorinated hydrocarbon liquid) and would absorb the electromagnetic energy in the evanescent zone. This material would have to be porous or channeled to allow displaced fluid to escape as the absorber moved toward the TIR interface. Such a material could be made by casting a layer of carbon-loaded silicone elastomer with an array of holes in it to allow the fluid to pass through or a series of channels on the surface to conduct the fluid into a reservoir.

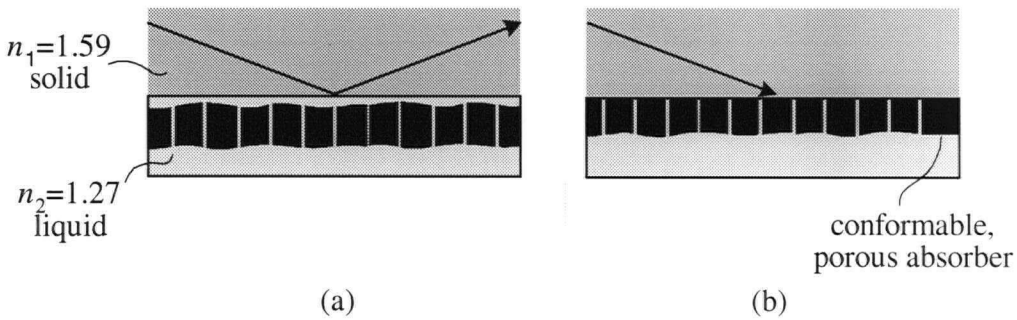

Figure 3-3. Frustration of TIR by a conformable absorber

A related approach would use a very thin, flexible porous membrane. In this case, the material composing the membrane need not be highly conformable since the flexible membrane itself could bend in order maintain optical contact along the surface, even in the presence of possible dust particles or small surface variations. This type of membrane could be made from a very thin polymer film, such as polyester sheeting, coated with an absorbing film. Alternately, a thin layer of metal could be vapour deposited onto a substrate that is later dissolved. In either case, this may only be practical for optical configurations where TIR occurs on a flat, not prismatic, interface.

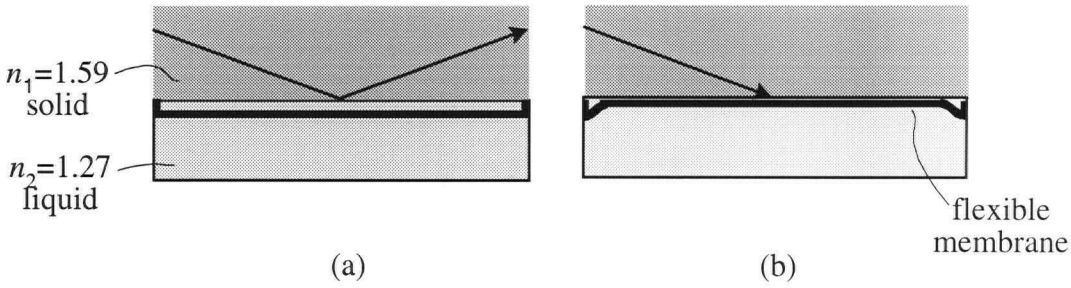

Figure 3-4. Frustration of TIR by a flexible membrane

Both of these approaches seemed prohibitively challenging and were not selected for further analysis at this stage.

Currently, the most promising absorption mechanism, and a primary focus of the research reported in this thesis, uses the electrophoresis of charged pigment particles to frustrate the TIR. As will be described in more detail in Section 3.7, pigment particles were suspended in perfluorinated hydrocarbon liquid, and the suspension was contained in a chamber at the rear of the device. In such a system, an electric field applied between transparent conductors on either side of the chamber moved the pigments, by electrophoresis, toward and away from the TIR interface. Although the pigment particles themselves were not highly conformable, they were sufficiently small that a layer of them coated the surface well.

Having identified this method for frustrating TIR at a solid-liquid interface, it is now necessary to discuss in more detail the approach for enhancing the effective index ratio to ensure that TIR occurs.

3.6 Enhancing index ratio with crossed prismatic sheet geometry

Consideration of the three-dimensional refractive index ratio enhancement effect described in Section 2.2.2 led to the discovery that it is possible to employ TIR at a liquid interface using conventional polycarbonate microstructured materials.[59] For example, Figure 3-5 shows an arrangement developed in this investigation that uses two layers of prismatic sheet, each having translational symmetry, in which the prism layers are oriented with their symmetry

axis mutually perpendicular.[60] This layered prismatic geometry, and others, are described more fully in Chapter 7. It is introduced briefly here to illustrate the index enhancement effect that is key to the design of a liquid-based TIR image device.

Figure 3-6 shows the ray path, in cross-sectional views, through this layered structure. As depicted in Figure 3-6(a), the top layer of micro-prisms is used to deflect incoming light rays. This deflection causes an initially normal incidence ray to propagate with a substantial component in the direction of translational symmetry of the bottom prism surface, producing an effective enhancement of the index ratio, as described in Section 2.2.2. The deflected light therefore undergoes TIR twice in the bottom prismatic layer, as in Figure 3-6(b), and returns to the top prism sheet, where the initial deflection is "cancelled" and the original incident angle is restored. This works for both of the deflection directions caused by the facets of the top layer, so most of the light leaves the structure traveling outward in the normal direction. There are many optical configurations using this crossed-prismatic sheet approach, each having different characteristics and advantages, and several of these are discussed in Chapter 7.

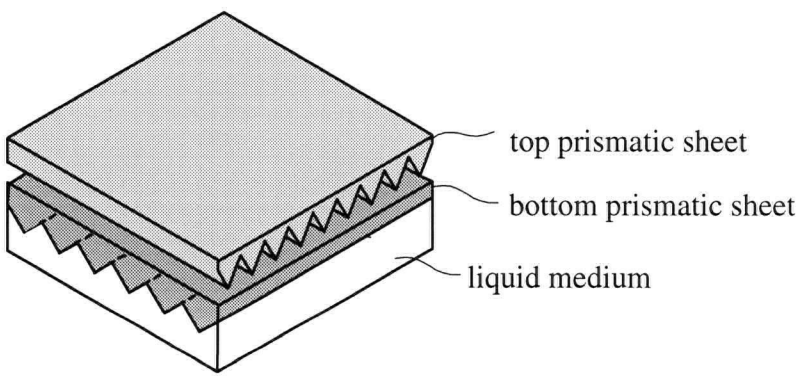

Figure 3-5. One optical arrangement for a liquid-based frustrated TIR device

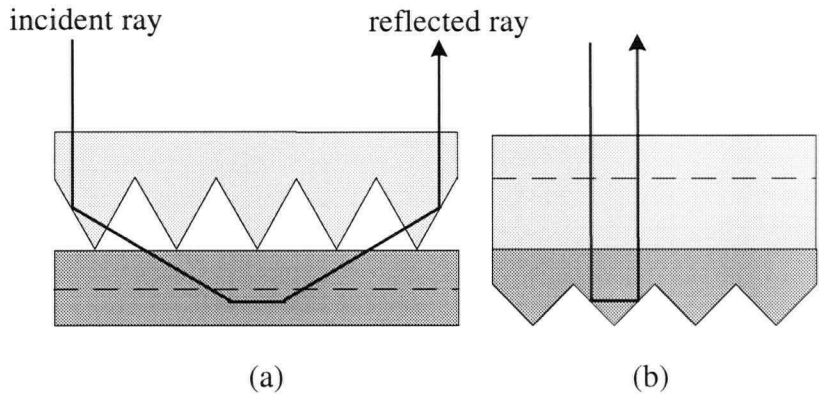

Figure 3-6. Path followed by a ray through optical arrangement

This layered prismatic approach is a novel application of the effective index ratio enhancement and it allows conventional micro-replicated surfaces to be used with perfluorinated hydrocarbon liquid to prevent adhesion of the absorber. Based on this concept, it is helpful to consider in more detail, in the following section, how pigments suspended in perfluorinated hydrocarbon liquid can be used to frustrate TIR.

3.7 Pigments suspensions in low refractive index fluid

For ideal frustration of TIR using this method of electrophoresis, the absorptive particles must be optically small so that they do not scatter much of the light, and have a sufficiently large imaginary refractive index component that most of the light encountering these particles is absorbed. For the particles to be "optically small", and therefore essentially non-scattering, the product of the effective diameter of the particle, D, and the difference in refractive index values between the particle and its surroundings, Δn, must be substantially less than the wavelength of the light.[61]

$$D\Delta n << \lambda \tag{3-2}$$

As an illustration, a typical particle diameter in these experiments is 0.25 μm and the refractive index difference of 0.5 yields a product $D\Delta n$ of 0.125 μm, which is substantially less than λ for the visible range of wavelengths of 0.4 to 0.7 μm.

As will be discussed later in this section, the required value of the imaginary refractive index component depends on the effective path as the light interacts with a layer of particles at the interface. If the effective path length is quite short, the particles must be highly absorptive in order to adequately frustrate the TIR. For longer path lengths, less absorptive particles are equally effective in frustrating TIR since the light interacts with a greater number of particles.

An additional requirement is that the particles must have a sufficiently high electrostatic surface charge, and hence electrophoretic mobility, so that they respond quickly to an electric field of magnitude that is practical in a display device. This requirement depends on the application, but for illustrative purposes it is helpful to consider the approximate value required in a typical reflective image device, in which the applied electric field magnitude is about 10^5 Vm^{-1}. In such a case, if the desired switching frequency is about 10 Hz, the particles must move about 1 μm, into the evanescent wave region in 0.1s. This corresponds to an electrophoretic mobility of $1x10^{-10}$ $m^2V^{-1}s^{-1}$, and a net surface charge, calculated using the relations described in Section 2.4, of $6.6x10^{-19}$ C.

In the course of this research, two different suspension formulations were studied.[62,63,64] In the first, the suspensions were composed of dyed latex particles, which had been formulated by combining a solution containing the monomer with the required catalyst. The resulting polymer molecules took the form of a roughly spherical particle, of average diameter about 600 nm, with the real component of the refractive index equal to about 1.6. At our request, various dyes were added and attached to the exposed receptor sites on the particle surface. A polymer dispersant material was also included which adsorbed onto the surface of the latex core to form a swollen polymer shell. Since these polymer chains have an affinity for both the adsorbed polymer layer and the perfluorinated hydrocarbon liquid, they provided the steric stabilization required to maintain a stable suspension, as described in Section 2.4.

These latex suspensions were tested using techniques described in detail in Chapter 4, and they did exhibit a small level of frustration of TIR, at most about 10%. This degree of absorption was insufficient from a practical point of view, so a second formulation, which employed a suspension of intensely coloured pigment particles and a liquid dispersant material was investigated.[65]

The results presented in this thesis were obtained using four of these pigment suspensions, each containing a single colour of pigment, as listed in Table 3-2. The suspension made using carbon black particles was particularly useful in analyzing various aspects of the system since the absorption spectrum for these particles is essentially uniform over the visible band. The cyan, magenta and yellow pigments were used to cause, for the first time, spectrally selective controlled frustration of TIR. Table 3-2 lists the specific pigments used in each of these suspensions.

Pigment colour	Product name	Supplier
Black	Raven Black 1200	Columbian Chemicals
Cyan	SpectraPak Blue	Sun Chemicals
Magenta	Cinquasia Magenta	CIBA Specialty Chemicals
Yellow	SpectraPak Yellow	Sun Chemicals

Table 3-2. Pigments suspended in perfluorinated hydrocarbon liquid

After formulation, the particle concentration and mean diameter were measured. The concentration was determined simply by evaporating the solvent from a known volume of prepared suspension and weighing the resulting solid content. The amount of solid content differs among the samples, but this does not affect the results of the experiments presented in this study as each sample was diluted to a known concentration prior to testing. The mean particle diameter was measured using the dynamic light scattering method discussed in Section 2.4.3, using a Coulter Model N4 Plus analyzer.[66] These results are presented in Table 3-3.

Pigment colour	Concentration (g/100ml)	Mean diameter (nm)
Black	5.25	118
Cyan	5.46	120
Magenta	2.84	310
Yellow	5.36	440

Table 3-3. Particle concentration and mean diameter

As well, the average electrophoretic mobility of the particles was estimated by observing the motion of charged pigment particles, over a reasonably long distance, under the influence of an electric field. To perform this experiment, a test cell was prepared, comprised of two

glass microscope slides, between which two 2 mm wide strips of thin (50 μm) brass were pressed, to be used as electrodes. The strips were separated by 20 mm, forming a cavity into which the suspension sample was injected, as sketched in Figure 3-7.

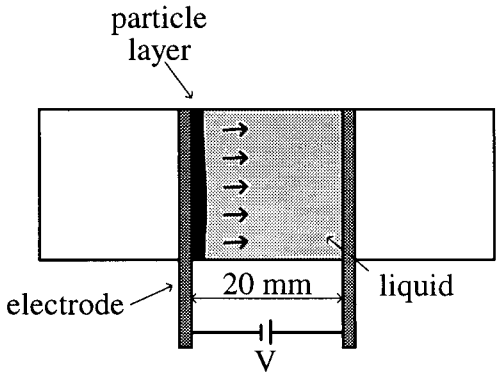

Figure 3-7. Electrophoretic mobility measurement set-up

When an electrical potential was applied between the two electrodes, the resulting electric field caused the pigment particles to migrate toward one electrode or the other, depending on the sign of their electrostatic charge, and the speed with which they moved depended on the electrophoretic mobility. Since the particles are intensely coloured, a distinct line was visible between the particles and the fluid and the speed was readily measured, enabling calculation of the average electrophoretic mobility.

This method of visual mobility measurement assumes that the electrophoretic pigment particles move at a constant velocity in response to the electric field to which they are subjected within the fluid gap. Although it will not be discussed in detail, it should be noted that the field experienced by the particles is not simply the field applied by the electrodes; rather, the local field experienced by one charged particle is altered by the presence of neighbouring charged particles and their counterions. In addition to the electrostatic forces, each particle is subjected to hydrodynamic forces from interactions with neighbouring particles and diffusion. As a result, the electrophoretic mobility calculated from this simple visual measurement is certainly not exact, but it provides a reasonable estimate of the value. The average mobility of the particles in these sample suspensions was estimated by this technique to be 1.6×10^{-10} $m^2V^{-1}s^{-1}$.

Figure 3-8 shows scanning electron micrograph (SEM) images of two different samples of (a) carbon black and (b) magenta pigments.

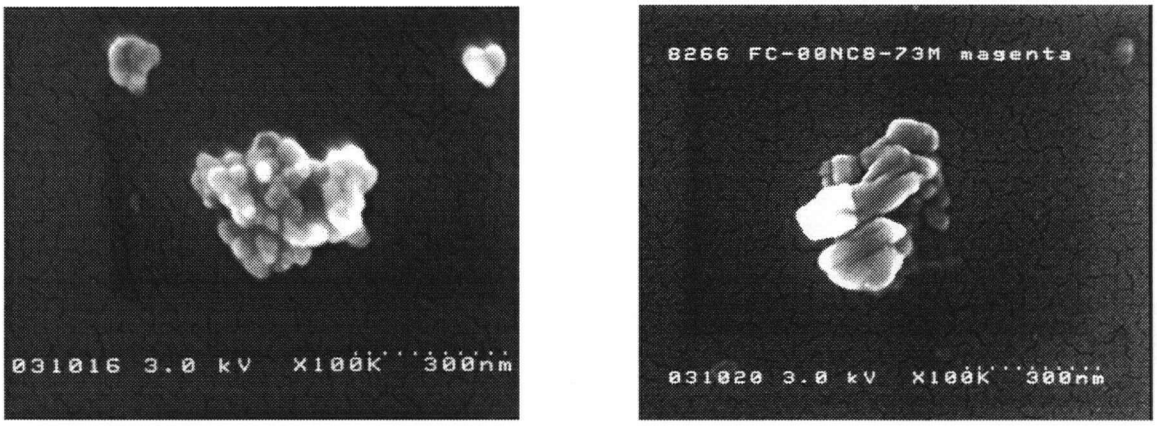

(a) (b)

Figure 3-8. SEM images of (a) carbon black and (b) magenta pigment particles

Fortunately, it was found that these formulations had a much greater ability to modulate the reflectance of a surface than the latex particles. Since the product of the particle size and the refractive index difference between the particle and surrounding medium is substantially less than a wavelength, the particles do not scatter very much.[67] As will be described in detail in Chapter 6, it seems that the key improvement in the pigment suspension over the dyed latex lies in the higher refractive index of the pigment particles, which enhances the effective path length. This effect is described briefly in the next section.

3.8 Frustration of TIR using pigment suspensions

In order to minimize the reflectance in the absorptive state of the system, it is important to develop a particle suspension capable of absorbing most of the incident light. This requires an understanding of the interaction between the light rays and the particles near the TIR interface. In this regard, a simple consideration of the frustration of TIR would suggest that maximum absorption would occur using very highly absorptive particles and that the degree of absorption would be completely determined by the number of particles occupying the region defined by the evanescent wave zone. In other words, the level of absorption should be proportional to the penetration depth of the evanescent wave (since this depth would

determine the number of absorbing particles that could occupy the region). This idea is depicted schematically in Figure 3-9, where in (a) a single layer of particles causes some absorption, but in (b) multiple particle layers filling the evanescent wave zone causes complete absorption.

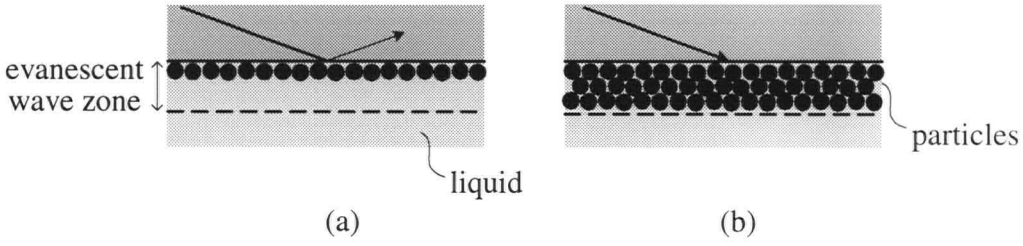

Figure 3-9. Schematic representation of evanescent wave zone

As explained in Section 2.1.3, the evanescent wave depth decreases with the incident angle, but this effect is only observable very close to the critical angle. Even though a substantially collimated detector is used in this study, such angular variations were below its collimation capacity. So, in the measurements described here, the evanescent wave depth is essentially independent of angle, and the observed absorption should therefore also be independent of angle. As well, since the penetration depth does depend directly on the wavelength of the incident light, so should the degree of absorption.

While this represented a plausible initial theory, the experimental results presented in Chapter 5 have demonstrated that it is insufficient to explain the absorption behaviour of the particles. As a result, an alternate theory, based on density gradients of small, high index, moderately absorbing particles near the interface, has been developed. Since these particles have a substantially higher index of refraction than the surrounding fluid, the particle density gradient produces a gradient of the effective refractive index of the suspension in this region. When the incident light encounters this index gradient, it follows a different ray path than it would in the absence of the particles, since the refractive index near the surface has been substantially modified. This is discussed in detail in Chapter 6, where reflectance predictions resulting from this theory are shown to be consistent with the experimental results.

The next section describes how the pigment suspensions are incorporated into a TIR-based reflective image display.

3.9 Electrophoretic suspensions in a TIR-based device

The simplest way to incorporate the pigment suspension is shown in Figure 3-10, in which the prismatic sheet and a rear flat substrate define a chamber that houses the suspension of pigment particles.[68,69,70] The prism facets and the rear substrate were each coated with a thin, (typically 100 nm) layer of transparent conductor, usually indium tin oxide (ITO), such that it makes direct contact with the electrophoretic suspension. (The conductor on the rear surface need not be transparent, since the light does not reach this layer, but ITO was usually used on this surface to simplify the overall system chemistry.)

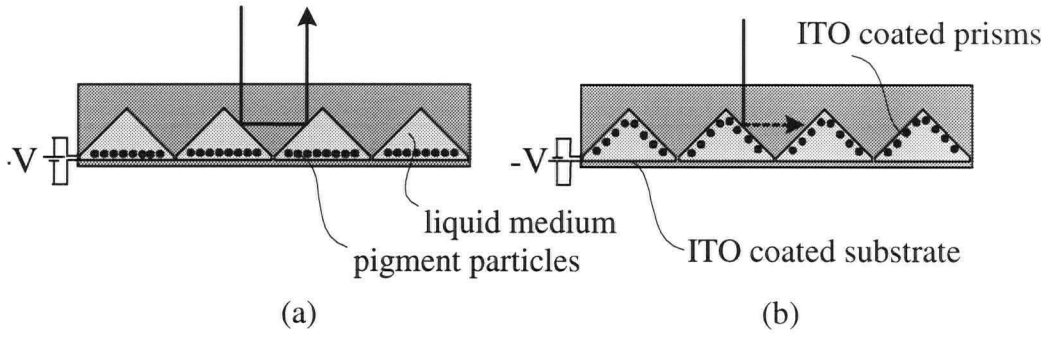

Figure 3-10. Design of an FTIR device actuated by electrophoresis

Application of an electrical potential difference between the two conductive surfaces generates an electric field throughout the liquid chamber. The pigment particles, which have an effective diameter of about 0.25 μm and an electrophoretic mobility of approximately 10^{-10} $m^2V^{-1}s^{-1}$, would then move in response to the field. Depending on the applied polarity, the particles would either move away from the prismatic surface, as shown in Figure 3-10(a), in which case the incident light would be reflected by TIR, or they would move into optical contact with the prismatic surface to frustrate TIR, as depicted in Figure 3-10(b).

The rear electrode is segmented between adjacent channels so that the pigments within each channel can be independently controlled. If the electrode were further segmented along the

length of the channel, the absorption of light within particular regions could be controlled to form a desired image in a pixelated fashion.

For the purpose of discussion in the next few sections, some terminology to describe the important regions of the device is introduced in Figure 3-11. As is clear from Figure 3-11(a), each prismatic electrophoretic channel is bordered by two neighbouring micro-prism reflective structures. Thus, when one electrophoretic channel is actuated by pulling the particles into the evanescent wave, as shown in Figure 3-11(b), it causes light to be absorbed in each of the two adjacent reflective structures. These reflective structures together form the absorption zone associated with that channel.

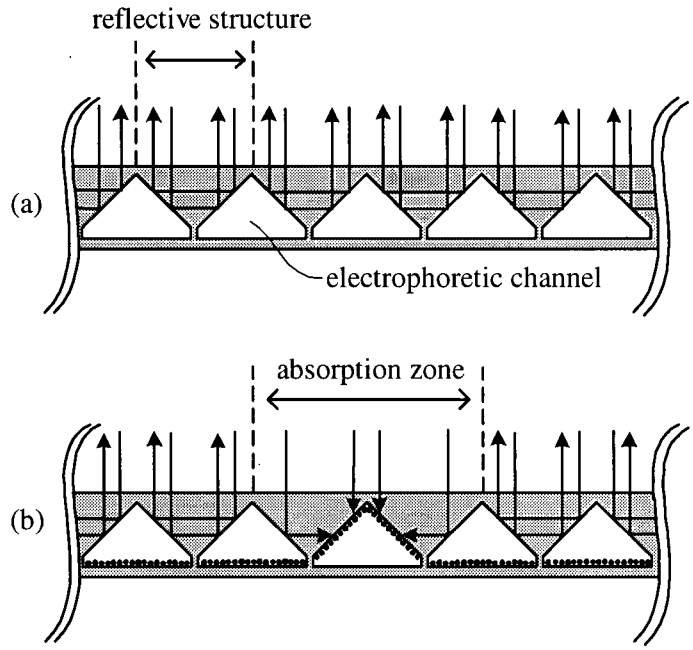

Figure 3-11. Selective absorption by electrophoretic channels

As detailed in Section 3.10, it is possible to achieve reflectance values intermediate between the completely reflective and completely absorptive states. This so-called grey scale behaviour is required for a practical device.

3.10 Grey-scale control of reflectance

Section 2.3 discussed the ability to achieve a complete gamut of colours by varying the relative amount of three primary colours. In terms of a TIR-based reflective image device, this requires the ability to yield not only full reflectance and absorption states, but also the continuous range of reflectance values intermediate between these two extremes. This is known as grey scale control. The continuous range of reflectance values is important both for full colour and monochrome devices.

There are at least two methods by which grey scale control could be achieved using frustrated TIR. Both methods rely on the fact that the amount of absorption caused by the pigment particles depends on the degree of interaction between the evanescent energy and the particles.

The first method, known as time dithering, would be appropriate in a system where the particles could be moved very quickly in and out of the evanescent wave region. These very mobile particles would be subjected to a reasonably high frequency (about 100 Hz) applied field so that they were oscillated in and out of the evanescent zone. By varying the amplitude and/or the duty cycle of the field, the fraction of one cycle that the particles would spend in the evanescent zone, thus causing absorption, could be controlled.

A second approach requires a particle system where the degree to which a particle penetrates into the evanescent wave zone depends, in a continuous manner, on the strength of the applied field. A system might exhibit this behaviour if the particles or the TIR surface were, for example, coated with an optically thick layer of a polymer material with a spring-like characteristic. In this case, in an applied field of a given strength, the particle would exert a force on this spring-like layer until it reached a position where the magnitude of the spring force equaled that of the applied force and would remain there as long as that field strength was applied. If the field was increased, the particle would move further into the evanescent zone until the forces again balanced and it settled into its new position. As a result, the level of absorption could quite accurately be controlled in such a system. The particle system tested in Chapter 5 showed a similar field-dependent behaviour, but for a somewhat different reason. This will be discussed in detail in Section 5.5.1.

3.11 Prevention of particle clustering by encapsulation

It has been observed by numerous researchers that particles in suspension under repeated cycles of applied electric field tend to congregate into loose clusters, leaving areas of high particle concentration amidst regions of almost pure solvent.[71] In preliminary tests during the course of this study, the same behaviour was encountered in the perfluorinated hydrocarbon suspensions.

Particle clusters are formed by the fluid motion within the cell. These clusters consist of loosely bound particles that can be readily redispersed. The tendency for clusters to form depends on the voltage and frequency of the applied waveform, and redispersion can generally be accomplished by varying the operating voltage or frequency. The size and pattern of the pigment clusters depends on the suspension composition, cell geometry, and switching operation.

In sample cells constructed and tested during the course of this study, these particle clusters often formed. In these sample cells, a particle suspension was housed between two parallel glass microscopes slide, coated on the inner surface with a layer of transparent conductor such as indium tin oxide (ITO), forming electrodes on either side of the fluid chamber. A time-varying voltage was applied across the electrodes, and the suspended particles repeatedly responded by electrophoretically moving back and forth across the cell. Initially, the particles would be uniformly dispersed in the suspension, so there was no visible non-uniformity on the surface of the sample cell. When the voltage was applied, the particle clusters would begin to form, and evolve as the switching continued. A CCD camera was positioned about 0.1 m above the cell and the images of the particle clusters were captured. The images captured for one typical sample cell are shown in Figure 3-12. In this case, white latex particles suspended in perfluorinated hydrocarbon liquid were enclosed in a 60 μm thick cell, and switched by a 25 V, 0.25 Hz square waveform.

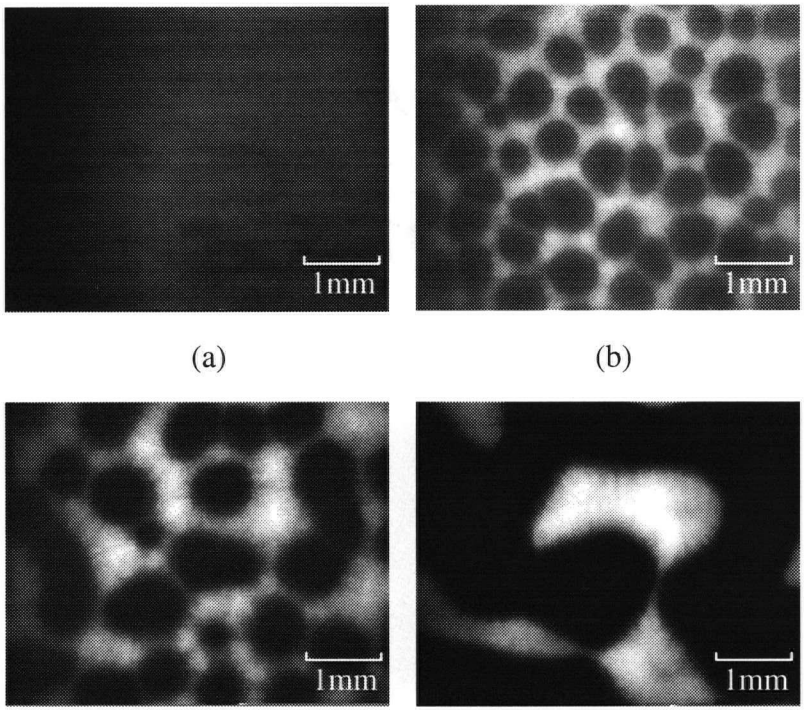

Figure 3-12. Particle clusters formed after (a) 0s, (b) 10s, (c) 40s and (d) 180s

This is a complex problem, thought to result from fluid disturbances in the vicinity of the moving particles during their transit across the cell. Fluid turbulence, as a result of particle motion, is thought to lead to pigment clusters, the size and pattern of which are related to the amount of charge in the suspension.[72,73] Although the details of this phenomenon have been intensely studied by numerous groups, they are not well understood. However, it is widely agreed that such clustering behaviour can cause serious performance degradation and should be avoided as much as possible.

It has since been established that clustering problems can be substantially avoided by encapsulating small volumes of the suspension and thereby restricting the migration of the particles, as mentioned in Section 2.5.2.[74] This idea can be incorporated in the TIR-based device by minimizing the separation distance between the peaks of the micro-prisms and the flat rear substrate. In Figure 3-10, for example, the prism tips are shown attached to the

substrate, thus completely preventing the fluid contained in one resulting prismatic channel from flowing into neighbouring channels. This achieves encapsulation in one dimension and additional encapsulation along the prism channels could also be achieved by a variety of polymer micro-replication techniques.

Although actual TIR-based reflective image devices must incorporate micro-prismatic structures, a simpler system was designed for measuring the absorption characteristics of the electrophoretic particles. For this purpose, test cells were made from a simple arrangement of glass microscope slides, thus avoiding any complicated optical effects arising from interactions with the microstructured surfaces. However, throughout the course of this research, it was advantageous to avoid particle clustering to minimize non-uniformity in the reflectance of the surface and, for practical purposes, to extend the useful lifetime of each cell. This was done by enclosing the suspension within a region between one flat surface and one microstructured surface that restricts particle motion. This will be explained in greater detail in Section 4.1. This resulted in a reasonably uniform surface reflectance, even after repeated cycling of the particles.

Experiments performed with these sample cells demonstrated that a hermetic seal between adjacent fluid micro-volumes is not necessary to substantially restrict the particle motion. However, as will be addressed in the following section, there are other practical reasons why a hermetic seal may be desirable.

3.12 Subtractive colour filtering in a full-colour image display

A second goal of this research program was to extend the concept of a reflective image device employing frustrated TIR to the creation of full colour. This section describes a new subtractive colour filtering approach that was devised to achieve this goal. In this approach, the spectral reflectance properties of the pigments cause them to behave as spectrally selective filters. Thus, using pigments with appropriate subtractive colour absorption characteristics, the colour of the reflected light can be controlled. This section outlines the use of subtractive colour filtering in a TIR-based reflectance device, describes a configuration of a full-colour device, and explains its operation.

3.12.1 Subtractive colour filtering in an FTIR image display

As discussed in Section 2.3.4, the available colour gamut is determined by the spectral absorption characteristics of a set of cyan, magenta and yellow filters, and any colour within this gamut can be achieved by suitably absorbing white light using these three filters. Ideally, in a full colour display based on TIR, each reflective structure would incorporate one controllable filter for each of the three subtractive colours so that all three filters could be individually controlled on each reflective structure. One potential method of accomplishing this would use reflective structures having three facets, such as the so-called "corner-cube" geometry in which the three reflective facets are mutually perpendicular. In this arrangement, the absorption of light could be controlled using a different subtractive colour filter on each of the three facets. Unfortunately, at present there is no practical way to fabricate such a device. Section 3.12.2 describes an alternative method for subtractively generating full-colour images using the more feasible linear geometry that was depicted in Figure 3-11.[75,76]

3.12.2 Construction of a full-colour FTIR image display

The construction geometry that was devised to generate full-colour images bears considerable similarity to that previously presented in the monochrome version discussed in Section 3.9. In the new full colour embodiment, the sealed prismatic channels are alternately (and cyclically) filled with cyan, magenta and yellow pigment suspensions, labeled in Figure 3-13 as *c*, *m* and *y*. A printed, striped filter layer covers the top of each reflective structure; the coloured filter stripes in Figure 3-13 are labeled by *C*, *M* and *Y* corresponding to their colour. The stripe colours are assigned such that the complementary colour stripe is positioned over each reflective structure. In other words, filter *Y* is adjacent to channels *m* and *c*, *M* to channels *c* and *y*, and *C* to channels *y* and *m*. Thus, each reflective structure has the ability to absorb each of the three primary colours red, green and blue. In each structure, one of these bands is always absorbed but the other two can be selectively absorbed in order to yield a desired net colour.

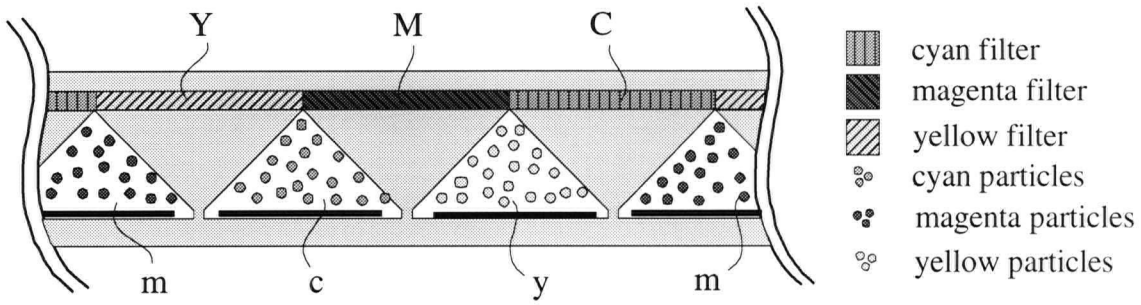

Figure 3-13. Schematic of a full-colour TIR-based reflective image device

Each filter, whether permanent or controllable, can be described in terms of its spectral transmittance function. In this discussion, $C(\lambda)$, $M(\lambda)$ and $Y(\lambda)$ will be used to denote the spectral transmittance functions of the permanent filter regions C, M and Y. Similarly, $c(\lambda)$, $m(\lambda)$ and $y(\lambda)$ denote the effective spectral transmittance functions of the electrophoretic particle systems contained in channels c, m and y. Ideally, the spectral characteristics of the permanent filter will be similar to those of the electrophoretic pigments, so that $C(\lambda) \cong c(\lambda)$, $M(\lambda) \cong m(\lambda)$ and $Y(\lambda) \cong y(\lambda)$.

It is important to note that although the design of a full-colour TIR-based reflective image device has been presented here, the actual fabrication of such a structure would be a great feat of micro-fabrication that would require substantial investment. The complexity and expense involved in such an endeavour is not unreasonable in terms of current liquid crystal display manufacturing practices. (For instance, the investment required to develop and manufacture the driving circuitry alone in a typical laptop computer display is astounding, since each individual pixel is modulated by a thin film transistor printed on the active matrix backplane.) However, this level of effort and expense is undoubtedly outside the scope of this thesis.

The purpose of this work was to establish the feasibility of the individual components of the system, in order to evaluate the practicality of this technique in the development of a real display. To accomplish this, currently available, but imperfect, micro-prismatic films, as well as experimental pigment suspensions were evaluated as a practical method for controlling TIR in the micro-prisms. Given the required investment, it is not possible to

analyze a fully assembled colour reflective image device as presented in this section. However, as will be discussed in later chapters, the results in this thesis demonstrate that this is a valid approach, and presents an opportunity for further study in a wide range of areas.

3.12.3 Operation of device

Consider the situation depicted in Figure 3-14, generating the net colour red. In this case, the magenta and yellow pigments are actuated, but the cyan pigments are not. For simplification, the intensity of light in each of the three different wavelength bands, red, green and blue, is represented by the presence or absence of a single correspondingly coloured light ray. Of course, as mentioned previously, intermediate values would also be used in a real device to produce non-saturated colours.

An examination of the leftmost reflective structure (beneath filter *Y*) shows that the blue ray is absorbed by yellow filter *Y* and the red and green rays pass through the filter. The green ray is then absorbed by the magenta particles in contact with the prismatic facet. However, since the absorption in the red band is negligible for the magenta pigment, the red ray undergoes TIR at this facet and travels toward the second facet, where it again reflects and exits through the yellow filter. As a result, the region defined by this reflective structure will appear red. In terms of the spectral transmittance functions, the net spectral reflectance, $\rho_Y(\lambda)$, of the region can be written as the product of the two spectral transmittance functions of the filters, or

$$\rho_Y(\lambda) = Y(\lambda)m(\lambda) \tag{3-3}$$

Similarly in the centermost reflective structure, magenta filter *M* passes the red and blue rays but absorbs the green. Both red and blue rays reflect at the first facet and travel toward the second facet, where the blue ray is absorbed by the actuated yellow pigment particles in electrophoretic channel *y*. Again, only the red ray exits this reflective structure, and the region will appear red. The net spectral reflectance of this region can be written as:

$$\rho_M(\lambda) = M(\lambda)y(\lambda) \tag{3-4}$$

Finally, in the rightmost reflective structure, the red ray is absorbed by cyan filter *C*, and the blue and green rays are absorbed by the actuated particles in electrophoretic channels *y* and *m*. Since all the light rays are absorbed in this reflective structure, this region will appear near-black, and the spectral reflectance function can be written as:

$$\rho_C(\lambda) = C(\lambda)y(\lambda)m(\lambda) \tag{3-5}$$

Recalling that the reflective units have a centre-to-centre separation of only 50 to 100 μm, these individual differently coloured bands would be unresolvable by the viewer, so the colours would appear blended together as a net resultant colour. This resulting colour can be specified by calculating the average spectral reflectance function, $\rho_{average}(\lambda)$:

$$\rho_{average}(\lambda) = \frac{1}{3}(\rho_Y(\lambda) + \rho_M(\lambda) + \rho_C(\lambda)) \tag{3-6}$$

The chromaticity coordinates and surface reflectance can be calculated accordingly, using the standard method outlined in Section 2.3.2. In this particular example, the net result is that essentially all of the blue and green light is absorbed and two thirds of the red light is reflected, yielding a net red reflectance which is 67% of that of a pure red reflector.

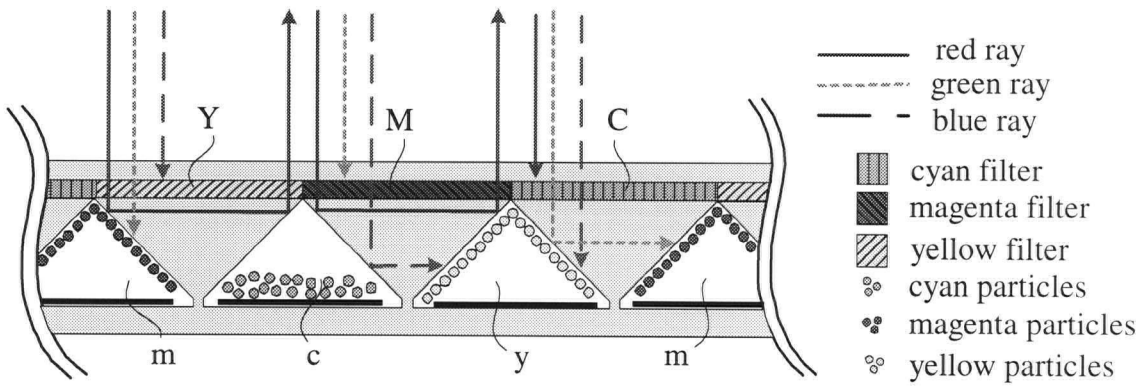

Figure 3-14. Actuation of an FTIR device, demonstrating a net red colour

Similar arguments can be used to show how a net yellow colour is displayed on the surface. In this case, only the yellow pigments in electrophoretic channel *y* are actuated. As depicted in Figure 3-15, in the leftmost reflective structure, blue light rays are absorbed and the red and green rays are reflected, so this portion of the sheet would appear yellow. In the centermost structure, both blue and green rays are absorbed, leaving a red coloured appearance. Finally, the rightmost reflective structure will appear green since the red and blue rays are absorbed. The combination of one third of the total area appearing yellow, one third appearing red and the remaining one third appearing green will be a net colour of yellow with a reflectance of 67% of that of a pure yellow reflector.

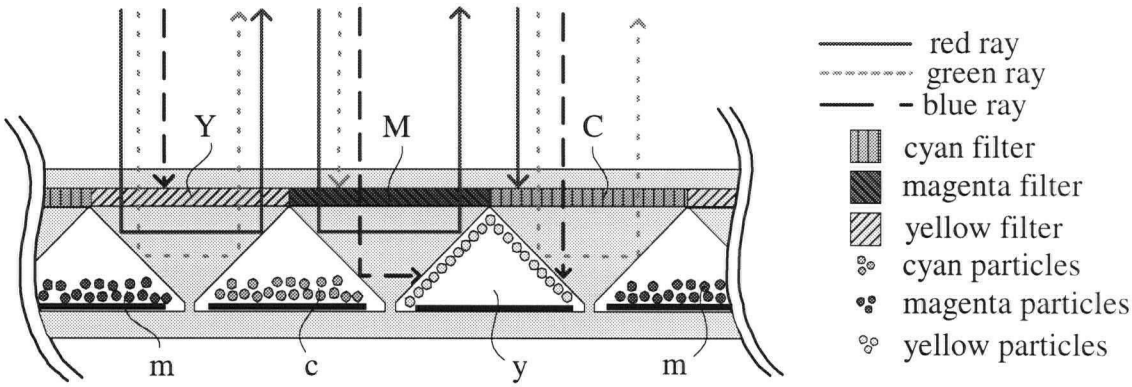

Figure 3-15. Actuation of an FTIR device yielding a net yellow colour

A complete description, presented in terms of the net spectral reflectance functions in Table 3-4, shows that the actuation of combinations of the electrophoretic channels generates net colours in the same manner as conventional subtractive colour filtering, as discussed in Section 2.3.4.

Status of channels			Resultant spectral reflectance, $\rho(\lambda)$			Net colour
y	m	c	$\rho_Y(\lambda)$	$\rho_M(\lambda)$	$\rho_C(\lambda)$	
0	0	0	$Y(\lambda)$	$M(\lambda)$	$C(\lambda)$	White (W)
1	0	0	$Y(\lambda)$	$M(\lambda)y(\lambda)$	$C(\lambda)y(\lambda)$	Yellow (Y)
0	1	0	$Y(\lambda)m(\lambda)$	$M(\lambda)$	$C(\lambda)m(\lambda)$	Magenta (M)
0	0	1	$Y(\lambda)c(\lambda)$	$M(\lambda)c(\lambda)$	$C(\lambda)$	Cyan (C)
0	1	1	$Y(\lambda)m(\lambda)c(\lambda)$	$M(\lambda)c(\lambda)$	$C(\lambda)m(\lambda)$	Blue (B)
1	0	1	$Y(\lambda)c(\lambda)$	$M(\lambda)c(\lambda)y(\lambda)$	$C(\lambda)y(\lambda)$	Green (G)
1	1	0	$Y(\lambda)m(\lambda)$	$M(\lambda)y(\lambda)$	$C(\lambda)y(\lambda)m(\lambda)$	Red (R)
1	1	1	$Y(\lambda)m(\lambda)c(\lambda)$	$M(\lambda)c(\lambda)y(\lambda)$	$C(\lambda)y(\lambda)m(\lambda)$	Black (K)

Table 3-4. Net colour resulting from actuation of electrophoretic channels

This chapter has discussed the critical issues faced during the novel design of a practical reflective colour image display based on TIR in microstructured reflective sheets. It was determined that undesirable surface energy effects could be overcome by using a liquid at the TIR interface to prevent direct physical contact between the absorbing material and the TIR surface. Although the optical properties of the liquid make it more difficult to achieve TIR, a unique layered prismatic geometry, taking advantage of the three-dimensional effective refractive index ratio enhancement effect, in combination with low index perfluorinated hydrocarbon liquid, makes it possible to achieve TIR in the system using readily available, polycarbonate microstructured materials. There are a number of possible absorbers which could be used to frustrate TIR in this system, the most promising of which is a suspension of absorptive pigment particles, which can move by electrophoresis in response to an applied electric field. These pigments can be chosen with specific spectral absorption characteristics, and arranged in the system to generate, when actuated, a full colour reflective image.

The frustration of TIR by electrophoresis of these coloured pigment particles represents the first demonstration of spectrally selective electrically controlled attenuation of TIR. The significance of this result may extend beyond the bound of its usefulness in a reflective image device, as described in this thesis. The ability to easily and quickly move an absorbing material into and out of optical contact with the interface to selectively absorb certain wavelengths of light while reflecting others is a key result of this work. The detailed experimental analysis of this effect is presented in the following two chapters.

4 SPECTRALLY SELECTIVE REFLECTANCE BY PIGMENTS

As explained in detail in Section 3.12, the absorption characteristics of the pigment particles in the electrophoretic suspension are crucial to achieving spectrally selective reflectance control. This chapter presents the experimental design for measurement of these absorption characteristics and the experimental analysis for some typical pigment suspensions.

4.1 Experimental measurement of spectral characteristics

A primary goal of this research has been to demonstrate modulation of total internal reflection by absorbing light energy, in particular by means of electrophoresis of pigment particles. In many practical applications, TIR occurs as a result of interaction of light with prismatic microstructures, and the combination of interactions with these reflective structures and the pigment particles can be quite complex. To properly evaluate the performance of these particles, it is necessary to simplify the experiment by separating the effects of the microstructures from the effects of the pigments. For this reason, the experiments performed in these next two chapters make use of high quality, large glass optical structures to produce the reflections, rather than less perfect polymeric microstructured surfaces.

Section 3.12 described the use of static colour filters with the controllable electrophoretic pigment channels in a full-colour reflective image device based on modulated TIR. In that arrangement, the light is appropriately filtered first as it passes through the permanent filter overlay, so the spectral transmittance of the filter is important. The light then reflects at the prismatic facets and thus encounters the pigment system. If the pigments are present at the interface, only certain wavelengths of light will be reflected, since the others will be absorbed by the pigments, so the light is again filtered as a result of this interaction. Therefore, the reflectance of the light at this facet is spectrally equivalent to the transmittance through a similarly coloured transmission filter located at the interface. As a result, although the light is undergoing reflection rather than transmission, the pigment filter will be described in terms of its effective spectral transmittance characteristics.

The effective spectral transmittance characteristics of the filters and the pigment systems were measured using a spectroradiometric telecolorimeter as the primary analysis instrument in an appropriate optical set-up, as described below.

4.1.1 Spectral analysis instrument

The measurement of light intensity and the analysis of colour across the electromagnetic spectrum from 380 to 780 nm were performed using a fast scanning, spectroradiometric telecolorimeter. The particular instrument used throughout the course of this study was the PR®-650 Spectrascan®.[77] Using this device, light passes through an objective lens and encounters a 1° aperture, followed by a shutter mechanism. Light traveling through the aperture and shutter strikes a concave holographic diffraction grating polychromator which diffracts light and focuses the resulting spectrum onto a photodiode array, in a manner such that the spectrum is permanently aligned with the elements in the detector array and, with careful calibration, the intensity of light in 4 nm increments across the spectral band is accurately known. Figure 4-1, adapted from the PR®-650 Spectrascan® manual, is a basic schematic of this arrangement.

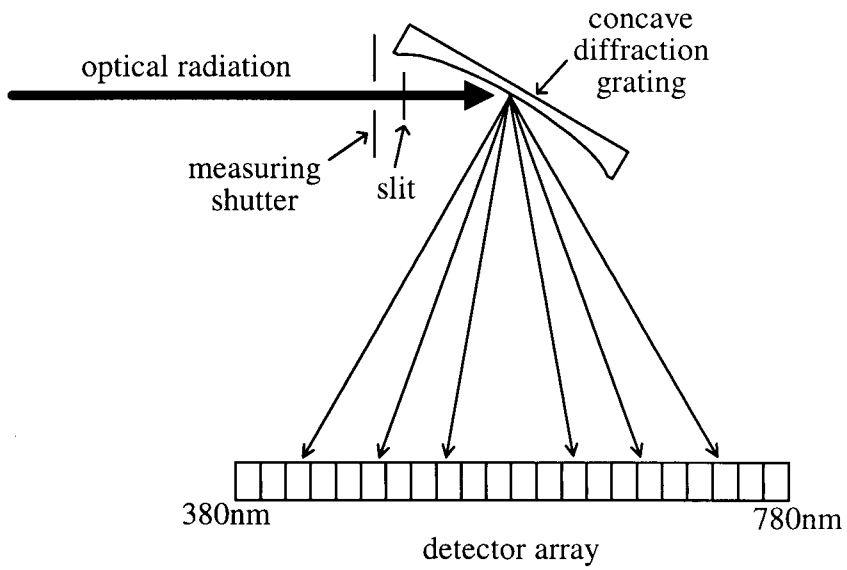

Figure 4-1. Operation of a spectroradiometric telecolorimeter

This instrument is a useful tool in measuring the spectral transmittance characteristics of the various filters, and effective filters, in the experimental system. It has been incorporated into the experimental set-up for the measurements presented in the following sections.

4.1.2 Set-up for measuring transmittance of static filters

As mentioned previously, the spectral transmittance of subtractive colour filters are important for a number of reasons, in particular for predicting the resultant spectral reflectance of the full colour reflective image device. A simple experimental set-up was used to measure the transmittance of the filters, as shown schematically in Figure 4-2. Here, a uniform, broadband, diffuse luminance source was directed at normal incidence toward the spectroradiometric telecolorimeter, separated by a distance of about 0.3 m. First, a background measurement was taken without a filter. The filter to be measured was then placed between the source and the detector, positioned about 0.05 m from the source. The readings with the filter were divided by the background readings to yield the spectral transmittance at each wavelength.

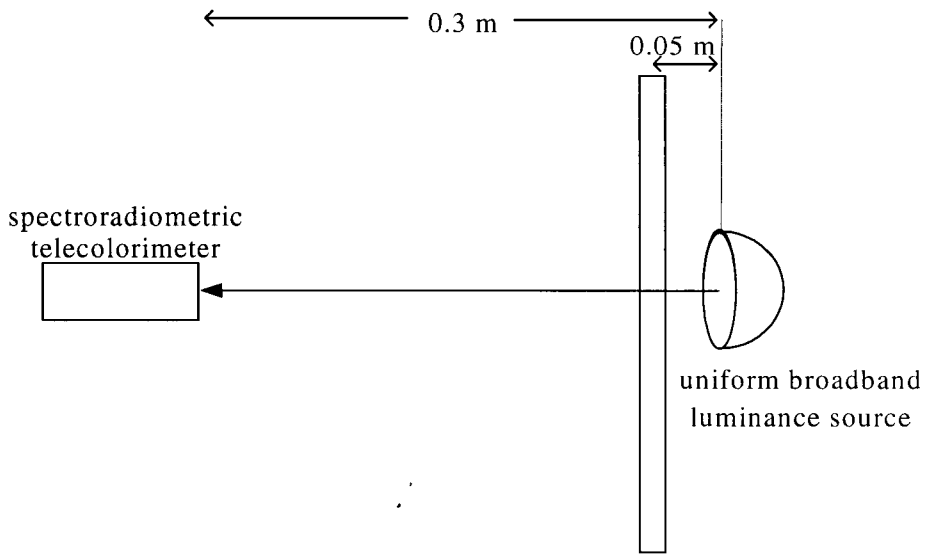

Figure 4-2. Set-up for measuring spectral transmittance of filters

This simple procedure was repeated for each of three subtractive coloured photographic filters. The effective spectral transmittance measurements for the electrophoretic pigment systems was somewhat more complicated as it required the construction of a test cell to house the electrophoretic suspension and apply the appropriate electric field. The next section describes the method devised to construct these cells.

4.1.3 Test cell construction

To measure the effective spectral transmittance of various pigment suspensions, a test cell was designed. Once optimized, this became a standard assembly throughout this study, and a large quantity was used on a regular basis. A cell consisted of two 25 mm x 75 mm glass microscope slides, each coated on one surface with a thin layer of indium tin oxide (ITO). (This coating was typically applied by sputtering, a standard thin film deposition technique, and such coated glass pieces are available from a number of commercial sources.[78]) This highly transparent conducting layer, approximately 50 nm thick, had a typical transmission coefficient of greater than 0.97 and a surface resistance of about 100 Ω/square. On one slide, two small holes, as shown in Figure 4-3(a), each about 1 mm in diameter, were sandblasted through the slide. These acted as fluid ports for filling the cell with the pigment suspension.

The test cell was constructed by placing the two ITO surfaces facing one another, but offset by a few millimeters to expose a region where electrical contact was made to the ITO surface of each slide, and a wire lead was secured to the conductive film using a small amount of conductive epoxy. This assembly is depicted in a side view of the cell in Figure 4-3(b). The front surface had to be made from a transparent material such as glass, as it was necessary for the light to transmit through it, but the rear surface did not need to be transparent since the light did not reach it. However, the ITO coated glass slide was appropriate since the surface was known to be uniformly smooth and conductive, and it introduced no additional substances into the system.

The slides were spaced a known distance apart by a spacer ring positioned near the edge. This spacer material was chosen depending on the desired gap thickness; for very thin cells, a layer of 10 μm polyester film was used, whereas for thicker cells, a layer of 60 μm thick

polyester tape was used. The size of the spacer was wide enough to provide a uniform gap, but sufficiently narrow that it did not interfere with the fluid ports. The edges of the slides were then sealed on all four sides using clear, non-conductive epoxy. This resulted in a hermetic seal around the edge of the cell, impermeable to both the fluid suspension and air.

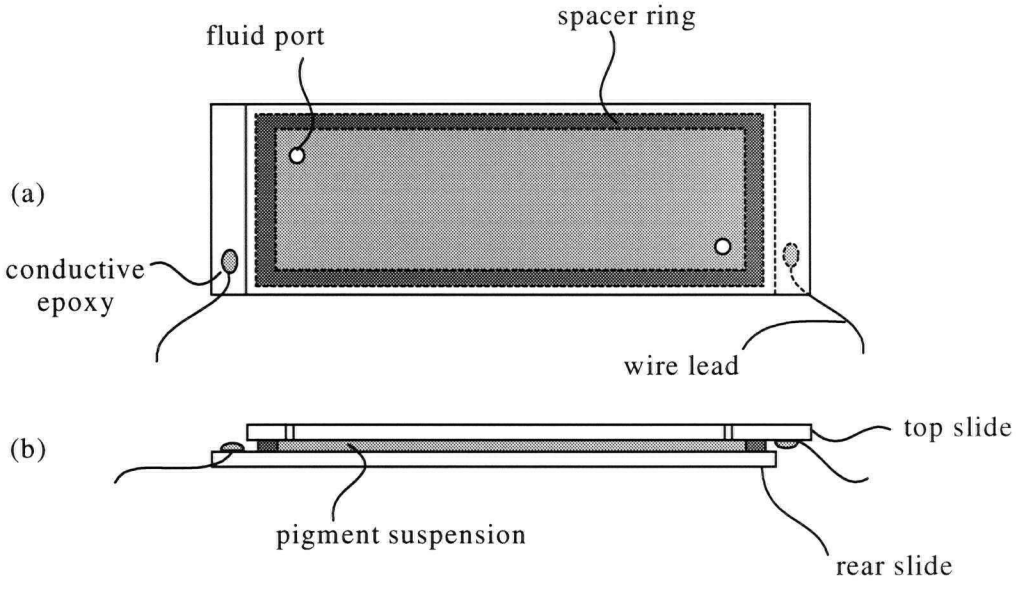

Figure 4-3. Top (a) and side (b) views of assembled electrophoretic test cells

The pigment suspension to be tested was introduced into the chamber by adding droplets through one of the fluid ports using a small gauge needle or pipette. Since the cell gap was quite narrow, the fluid was drawn between the slides quite effectively by capillary action. The fluid was added through one fluid port until all of the air bubbles were evacuated through the second port. Once the cell was filled, the ports were sealed using the clear epoxy.

In many measurements using these test cells, it was desirable to maintain uniformity in pigment distribution and prevent the problems associated with particle clumping described in Section 3.11. For this reason, the rear glass slide was sometimes replaced by a length of prismatic microstructured material, also coated with ITO and positioned so that the prism tips were almost in contact with the flat top surface to create prismatic channels, as shown in the cross-sectional segment in Figure 4-4. It was desirable to minimize the separation distance between the prism and the flat surface and, since the microstructured material is somewhat

flexible, it was necessary to include a spacer material within the active region of the test cell, as well as around the edges, to prevent the sheet from sagging in the center and making electrical contact with the flat top surface. This was accomplished by dusting the flat surface with a random distribution of approximately 50 μm diameter glass micro-spheres. These micro-prisms were 25 μm high, with a tip-to-tip spacing of 50 μm, so the micro-spheres fit snugly into the valleys between the prisms. A sufficient amount of pressure was applied to slightly embed the micro-spheres into the somewhat pliable microstructured sheet, to prevent them from moving, as well as decrease the gap distance.

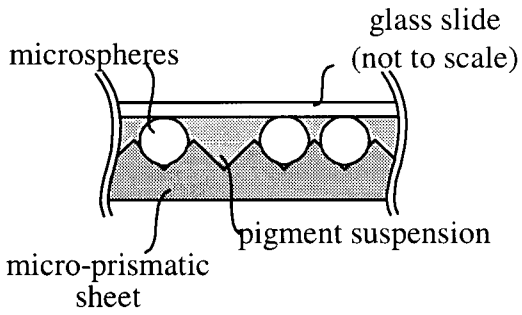

Figure 4-4. Modified test cell incorporating micro-prisms

It was determined, by constructing a number of samples, that about 20% coverage of the active area by a single layer of micro-spheres was sufficient to maintain a reasonably uniform gap separation, but did not restrict the flow of the pigment suspension into the cell when it was filled. This new assembly confined the pigment particles primarily within the prismatic channels and prevented the deterioration associated with particle clumping. In this case, the prismatic structure was required to restrict particle migration, rather than for any unique optical function; in fact, since they were located on the rear surface of the cell, they did not interact with the incident light at all.

In the experimental set-ups using these test cells, as described in Sections 4.2 and 5.2, the incident light was directed through the flat top surface of the test cell, thus avoiding any complications arising from interaction with imperfect polymeric optical microstructures. This allowed an analysis of the behaviour of the pigment suspensions, independent of contributions resulting from the reflective microstructured sheets.

4.1.4 Set-up for measuring TIR-attenuation by pigment systems

The attenuation of TIR was measured as a function of wavelength for electrophoretic pigment samples, when these pigments were electrostatically moved into contact with the TIR surface. The suspension was sealed inside a test cell and placed underneath a right angle glass prism, shown schematically in Figure 4-5(a). This prism is required to ensure that TIR occurs at the glass/fluid interface in the cell. The critical angle, θ_c, for this interface is 58.3°, so light rays incident on this interface at angle θ greater than 58.3° can undergo TIR. Figure 4-5(b) shows why the prism in Figure 4-5(a) is needed. In this case, light rays travel through air, with index n_1=1.0, striking a flat slab of glass, n_2=1.5, which is backed by a fluid medium with index n_3=1.276. The rays are refracted as they enter the glass medium and there is no incident angle, ϕ, for which refracted rays will exceed θ_c at the rear surface. With the addition of the prism, the angular requirements are changed so that light rays incident on the side facets are refracted such that for some angles the ray will undergo TIR at the rear facet. Specifically, in the design in Figure 4-5(a), light rays striking the prism at an angle, ϕ, greater than 65° with respect to the vertical are refracted such that they undergo TIR at the rear surface.

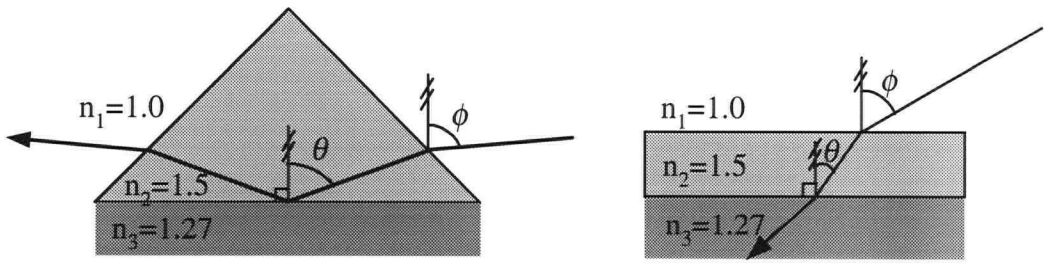

Figure 4-5. Achieving TIR by refraction through a prism

Many of the experimental set-ups described in this thesis took advantage of this geometrical approach by attaching the test cell to the rear surface of a prism, as shown in Figure 4-6. The region between the top surface of the test cell and the prism was coated with a thin layer of paraffin oil, which has an index of refraction of 1.51, approximately the same as that of the two neighbouring glass surfaces. This index-matching layer was necessary to ensure that

incident light rays passing through the glass prism maintained the same angle and were not reflected by an air gap as they passed into the top glass surface of the cell.

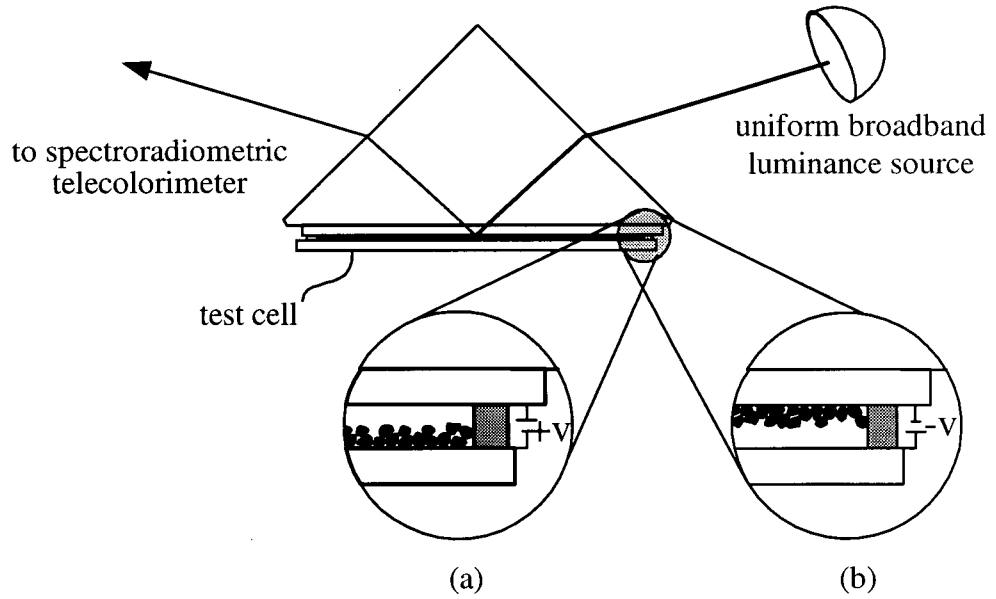

Figure 4-6. Measuring attenuation in (a) TIR and (b) frustrated TIR states

As discussed in detail previously in Chapter 3, the particles moved in and out of the evanescent wave region in response to the field applied across the cell. As in Figure 4-6(a), maximum reflectance was achieved when the particles were moved away from the top glass surface, since the positively charged particles moved away from the top electrode. When the polarity of the voltage, and hence the direction of the field, was reversed, as in Figure 4-6(b), the positively charged particles moved toward the interface to absorb the light energy, minimizing reflectance.

To determine the spectral attenuation caused by the pigments in this arrangement, the wavelength distribution of the reflected light was measured by the spectroradiometric telecolorimeter when the pigment particles were held fixed at the TIR surface by a field of constant strength. The instrument does not collect data quickly enough to resolve rapidly fluctuating reflectance data. For this reason, measurements of the electrophoretic pigment system were taken after all of the pigments had moved into contact with the interface so that the system was in a steady state.

Light from a uniform, broadband, diffuse light box, with a luminance of about 1000 cd m^{-2}, was directed on the prism set-up. The spectroradiometric telecolorimeter was positioned accurately at ϕ=68°, (corresponding to θ=60°, or 1.7° greater than the critical angle), to detect the reflected rays, and measured the spectral distribution of the light reflected when the electrophoretic particle system was held in the absorbing state. Examples of such measurements are presented in the next section. For comparison, spectra were also recorded for the non-absorbing state, and with the prism alone to ensure perfect reflection.

4.2 Experimental measurements of spectral transmittance

The design of a full-colour reflective image device, as described in Section 3.12, incorporates both photographic quality transmission filters and electrophoretic particle systems which effectively act as transmission filters. The spectral transmittance characteristics of these filters are required to calculate the achievable colour gamut. The measured spectral transmittance characteristics for some samples of both photographic filters and electrophoretic particle systems are presented in this section.

4.2.1 Spectral transmittance characteristics of photographic filters

The spectral transmittance characteristics were measured for three commercially available photographic subtractive colour transmission filters.[79] Figure 4-7 shows the transmittance characteristics measured for these filters, normalized by dividing by the intensity in the absence of the filter.

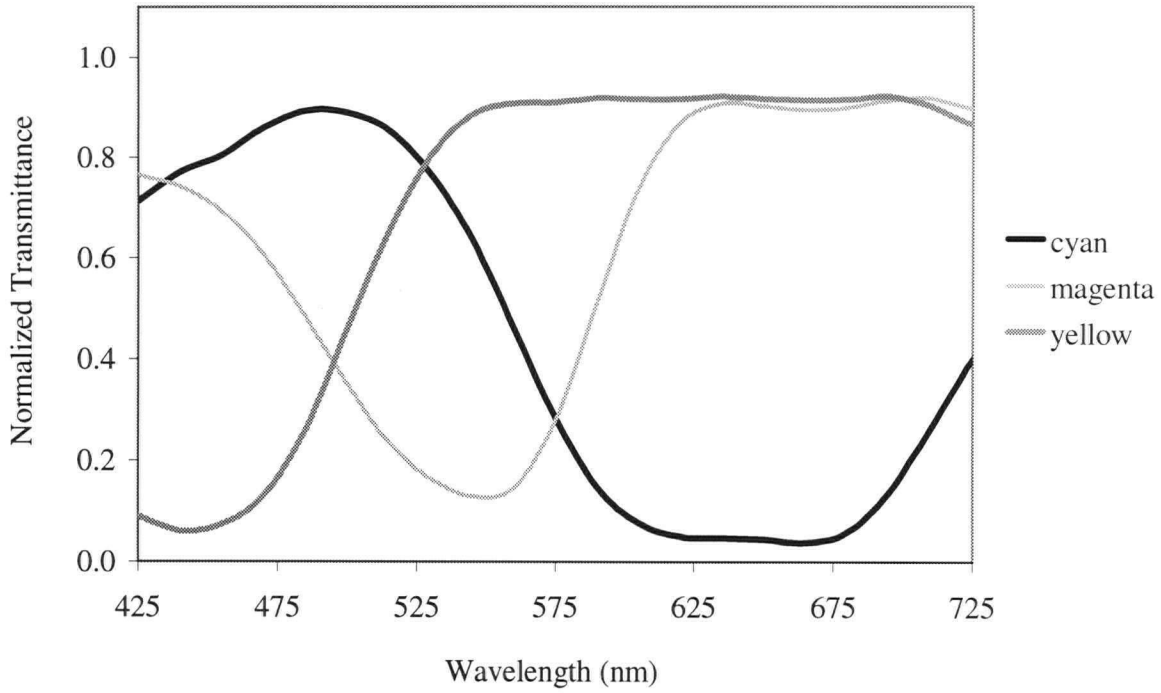

Figure 4-7. Spectral transmittance measured for photographic filters

For the cyan filter, as expected, there was limited transmittance of light (in other words, a high degree of absorption) in the red band, whereas the transmission is high in the blue and the green bands. Similarly, the yellow filter exhibits almost complete transmission of light in the green and red bands, but only low transmittance across the blue band. The magenta filter also exhibits reasonably high transmittance in the red and blue bands. In its absorptive green band, this filter shows fairly low transmittance. The average transmittance of these filters in the blue (450-500 nm), green (500-580 nm) and red (580-700 nm) wavelength bands are shown in Figure 4-8. (It is worth noting that the maximum transmittance is about 92%, since the remaining 8% of the light intensity is lost to partial reflections on the surface of the filters.)

None of these filters exhibits perfect transmittance characteristics since the wavelength cutoff is not sharp. Nevertheless, as will be demonstrated in Sections 4.2.3 and 4.2.4, in combination with the electrophoretic pigments, these filters yield an adequate colour gamut. In applications where a higher degree of spectral purity is desired, filters with sharper transmission cut-offs could enable a slightly larger gamut.

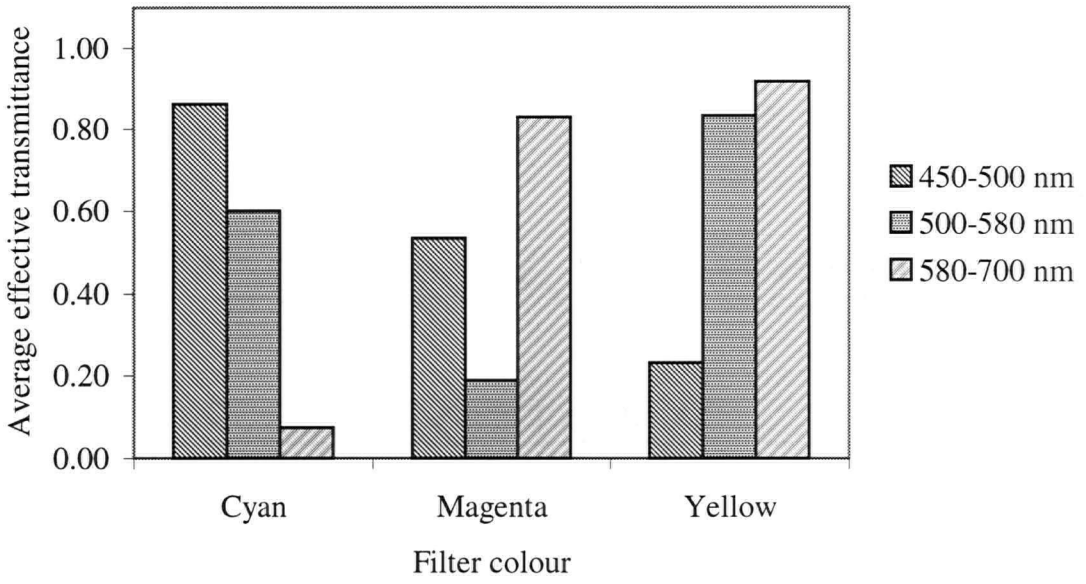

Figure 4-8. Average transmittance of photographic filters

4.2.2 Effective spectral transmittance characteristics of pigment systems

The effective transmittance of the cyan, magenta and yellow pigment systems, detailed in Section 3.7, was obtained from the TIR attenuation experiments described in Section 4.1.4. Figure 4-9 depicts these results. Each of the electrophoretic pigment systems absorbs about 80% of the light in the desired wavelength band. This is an acceptable level of absorption, although the transmittance of wavelengths outside this band is not as high as that of the photographic filters.

Of the three different pigment systems, the cyan suspension offers the best spectral characteristics, with low transmittance of about 24% in the red band, and substantially higher transmittance in the blue and green bands. The yellow pigment provides equally good absorption in the blue, with transmittance of only 19%, however the transmission outside of the absorptive band, while acceptable, is not as high as that of the cyan. The magenta particles are highly absorptive in the green band, with transmittance of 16%, but also exhibit a substantial amount of absorption in the blue. The net result is that the magenta particles have a more red appearance than, for example, the magenta filter described in the previous section. These transmittance values are summarized in Figure 4-10, where the average

effective transmittance in each wavelength band is compared for the different pigment colours.

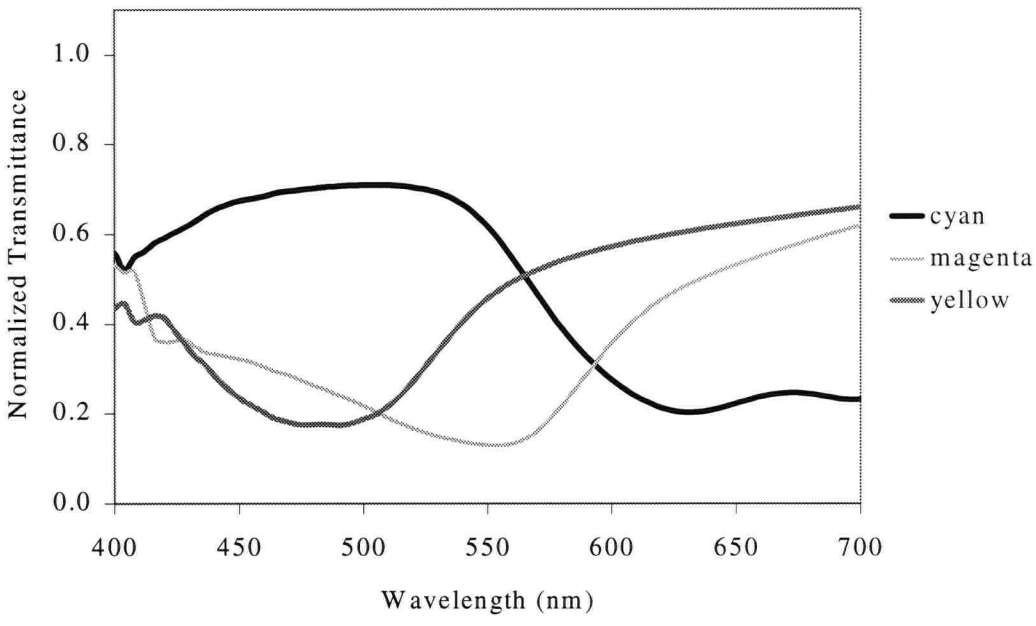

Figure 4-9. Effective transmittance of pigment systems

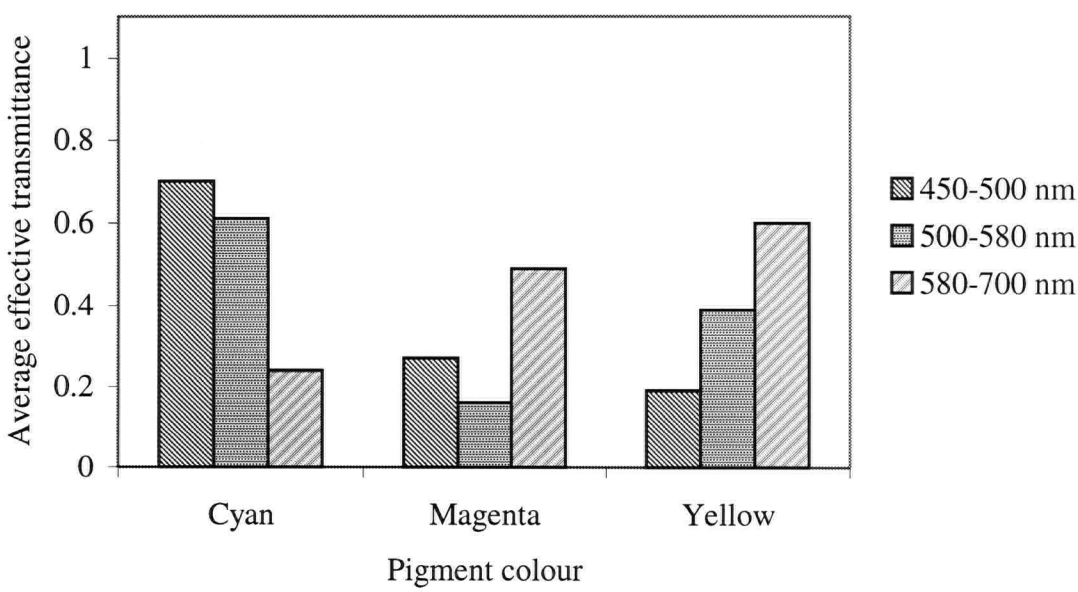

Figure 4-10. Average effective transmittance for pigment system

Although these transmittance characteristics are less than ideal, these initial pigment suspensions are the first demonstration of controlled spectrally selective frustration of total

internal reflection in an optical device. These pigment suspensions work in this manner because the particles are optically small, so that they are essentially non-scattering yet sufficiently absorptive that when moved toward the interface, they achieve a high net absorption. Chapter 6 gives a more detailed description of this phenomenon, including models for the interaction of the light with various particle density distributions.

A suspension of carbon black particles was also prepared, as described in Section 3.7. This suspension was used in a number of experiments where a spectrally selective response was unimportant. These black particles provided significant broadband absorption of the light, and resulted in a very low reflectance level in the frustrated state. The effective spectral transmittance of this particle system was measured using the same procedure as for the coloured pigment samples. The results shown in Figure 4-11 confirm that the carbon black particles are capable of frustrating TIR across the visible spectrum. This particle suspension is useful not only in experimental analysis of the system, but also in the development of a monochrome, high contrast reflective image device.

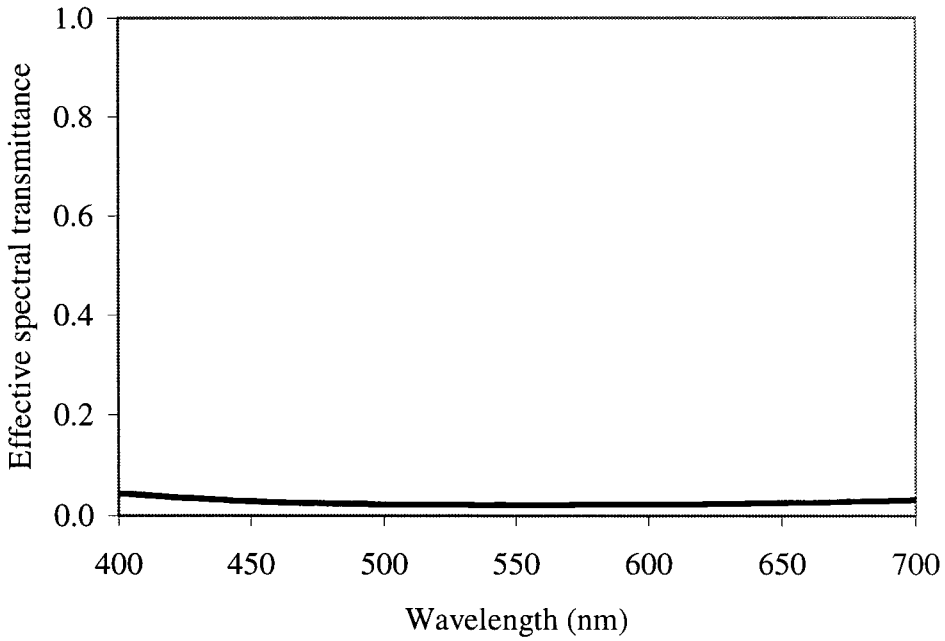

Figure 4-11. Effective spectral transmittance of carbon black system

The absorption characteristics of the initial subtractive coloured electrophoretic pigment suspensions are not ideal, but they could be used in a full-colour TIR-based reflective image

device to generate an adequate colour gamut, as discussed in further detail in the following sections. As the first suspension designed for the modulation of TIR, they show promising new results. In addition, it appears promising that modifications can be made to the pigment suspensions to further improve the spectral response and resultant colour gamut.

4.2.3 Combined spectral reflectance of system

As explained in Section 3.12.3, the spectral transmittance of the filters, $C(\lambda)$, $M(\lambda)$, and $Y(\lambda)$, combine with the spectral transmittance of the pigment systems, $c(\lambda)$, $m(\lambda)$, and $y(\lambda)$, to produce an overall spectral reflectance of the device, as detailed earlier in Table 3-4.

The chromaticity coordinates predicted for the combinations of the photographic filters and electrophoretic pigment systems were calculated as described in Section 2.3.2, demonstrated in the sample calculation provided in Appendix D. The values of the chromaticity coordinates x and y, as well as the luminous reflectance values ρ, are presented in Table 4-1. These values are calculated for the current electrophoretic pigment systems and for an ideal pigment system that would have spectral transmittance characteristics approximately equivalent to those of the filters shown in Figure 4-7.

Net colour	CIE coordinates (current)			CIE coordinates (ideal)		
	x	y	ρ	x	y	ρ
White (W)	0.318	0.332	0.595	0.318	0.332	0.595
Yellow (Y)	0.398	0.415	0.419	0.417	0.475	0.546
Magenta (M)	0.345	0.245	0.221	0.343	0.232	0.280
Cyan (C)	0.233	0.318	0.373	0.193	0.306	0.359
Blue (B)	0.241	0.213	0.109	0.183	0.166	0.121
Green (G)	0.300	0.423	0.231	0.251	0.546	0.311
Red (R)	0.450	0.316	0.136	0.502	0.374	0.250
Black (K)	0.329	0.297	0.059	0.268	0.402	0.093

Table 4-1. Calculated chromaticity coordinates and luminous reflectance

These chromaticity coordinates demonstrate that the system is capable of generating colours over a reasonable range of the spectrum. This is further indicated by the colour gamut presented in the next section.

4.2.4 Achievable colour gamut

The chromaticity coordinates shown in Table 4-1 are presented in Figure 4-12 on the standard CIE chromaticity diagram. The gamut predicted using the current electrophoretic particle system is shown by the solid line on the diagram, and the area of this colour gamut represents an acceptable range of colours. The gamut predicted for an ideal particle system is larger than the gamut achieved with the current suspensions, and is almost as large as those found in additive, phosphor-based colour imaging systems.

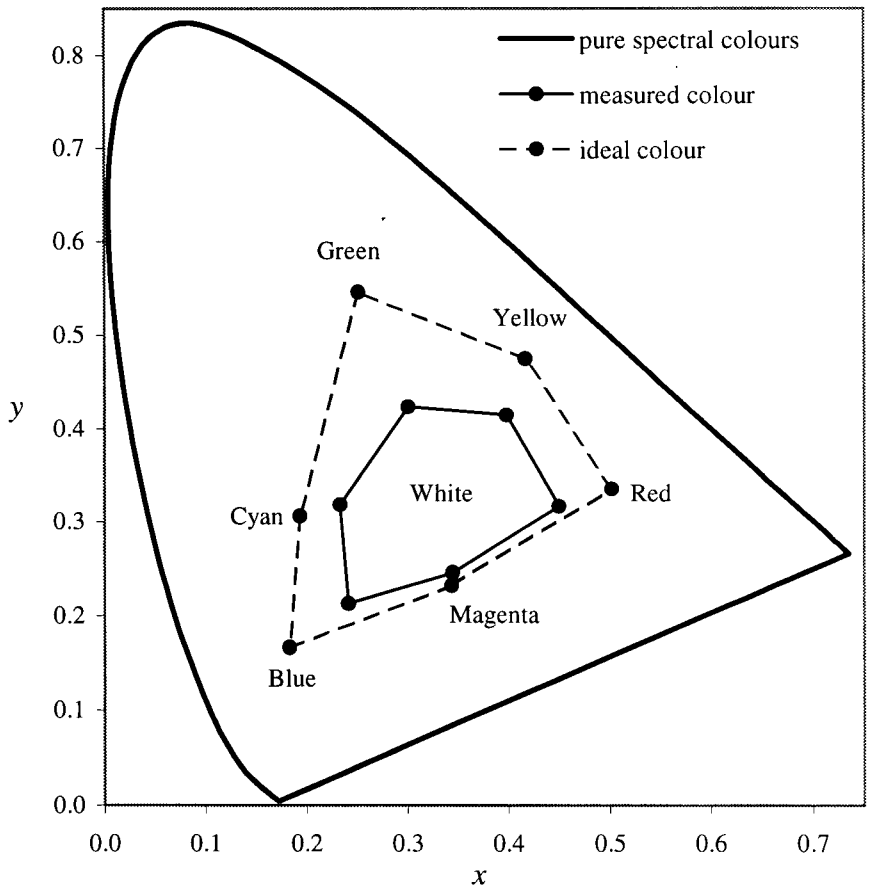

Figure 4-12. Measured colour gamut

Having demonstrated the potential for a full colour display, it is now appropriate to study in greater depth the physics responsible for achieving the large observed change in reflectance of this new electrophoretic system.

5 REFLECTANCE MODULATION BY PIGMENT PARTICLES

In addition to the wavelength dependent reflectance measurements presented in the previous chapter, the time-varying reflectance modulation by the pigment particles provides information about the overall absorption capabilities, the electrophoretic mobility and the electrostatic charge of the particles. From these results, we can infer the time-varying particle density distribution.

5.1 Measuring reflectance

As described previously in Section 2.1, TIR depends on incident angle, so it is important that the angle at which the reflectance of the system is measured be accurately controlled. This is a not a trivial issue in this study, since accurate control of the detection angle requires substantial collimation of the light, which reduces the intensity of the measured signal.

The detection system constructed for this purpose used a TSL251 light-to-voltage optical sensor, a monolithic silicon integrated circuit containing a photodiode, an operational amplifier and various feedback components.[80] This sensor operates linearly over an irradiance range from 0.001 to 1 mWm^{-2}, which includes the luminance values expected in these experiments. This was convenient, since it meant that complicated calibration of the detector was not required. This signal was fed into a linear amplifier, with the controllable gain adjusted accordingly to maximize the signal. The specification of the optical sensor is provided in Appendix D.

As shown in Figure 5-1, the optical sensor was mounted inside near the end of a hollow tube measuring 200 mm long and 7.5 mm in diameter. The inner surface of the tube was threaded to provide a roughened surface and painted black so that light rays were absorbed even at glancing angles, unless they fell within the desired detection cone. The opposite end of the tube was fitted with a mask arrangement, consisting of two black caps, each with a 1.5 mm hole drilled in the end, and the mask was aligned concentric with the collimating tube and the optical sensor within.

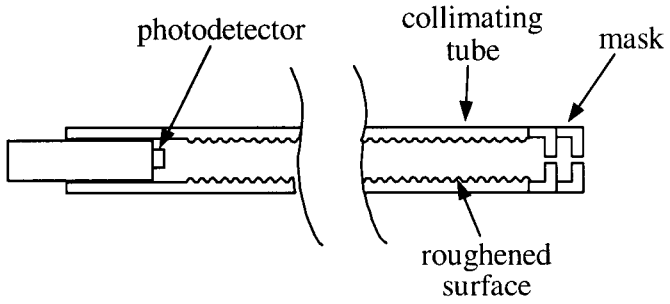

Figure 5-1. Cross-sectional view of light collimating tube

This collimated detector had an angular response full width half max of about ±1°, as shown in Appendix G, and is a key component of the experimental set-up described in the following section.

5.2 Design of the reflectance modulation experiment

As in the spectral measurements described in Section 4.1.4, it is important to study TIR without the added complexity of the micro-prisms that would be used in a real device. Therefore, a large, right angle prism was again attached to the test cell, as in Figure 4-6, to ensure that incident light directed at the cell undergoes TIR.

It is well known, as described in Section 2.1.3, that there are some interesting angular effects near the critical angle, within about 0.2°, where the evanescent wave penetration depth is substantially increased. Given this, it was initially postulated that there could be a correlation between the level of absorption and the evanescent wave penetration depth. However, to measure light intensity within such a restricted angular range, while ensuring that contributions from light rays outside this range do not interfere with the signal, an extremely tightly collimated detector would be required, having over an order of magnitude finer range than the one described in the previous section. This restriction would reduce the optical signal by several orders of magnitude, and would make time-resolved detection very difficult. In order to fully explore a possible correlation between the absorption and penetration depth, it would be necessary to make this compromise. However, as described later in this chapter, there is no evidence of such a direct correlation and this unexpected

result will be more fully addressed and explained in Chapter 6. For this reason, a more practical level of collimation was employed in the measurement described below.

As described earlier, the refraction of light rays through the angled facet of the prism enables the TIR conditions to be met at the liquid/glass interface of the test cell. For the experimental results presented in this chapter, light rays striking the interface within an angular range of ϕ=68° to 85° were measured. As a result of the refraction caused the prism facet, this input range corresponded to an internal angle of incidence ranging from θ=60° to 70°. The extremes of this angular range are depicted schematically in Figure 5-2.

The minimum angle in this selected range, θ=60°, was 1.7° greater than the critical angle of 58.3°. This was a sufficient extent beyond the critical angle that the entire angular acceptance range of the detector (±1°) was beyond critical. The constraint at the other end of the range was a practical one, since more glancing incidence would require an impractically narrow beam. This range provides a substantial variation of angle that yields useful information about the physics of the system.

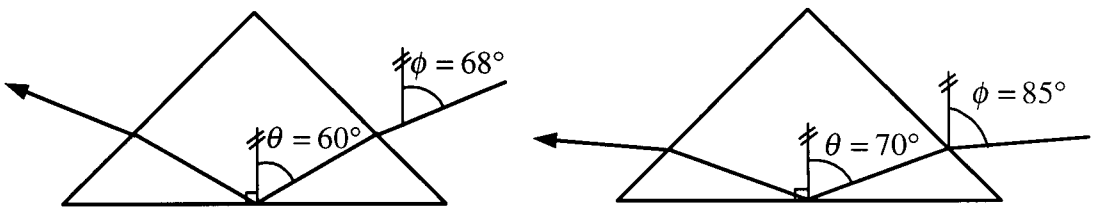

Figure 5-2. Extent of angular range measurements

For each angle, the reflectance was measured as a function of time in response to programmed variations of applied field, using a customized computer controlled power supply and data acquisition system. The system, run on a PC, included a GPIB-PCIIA board to apply a controlled voltage across the cell through a Stanford Research Systems DS335 function generator and an Advantech PCL-818HG A/D converter data acquisition card to sample, at a specified frequency, the reflectance signal measured by the light detector circuit, as shown schematically in Figure 5-3.

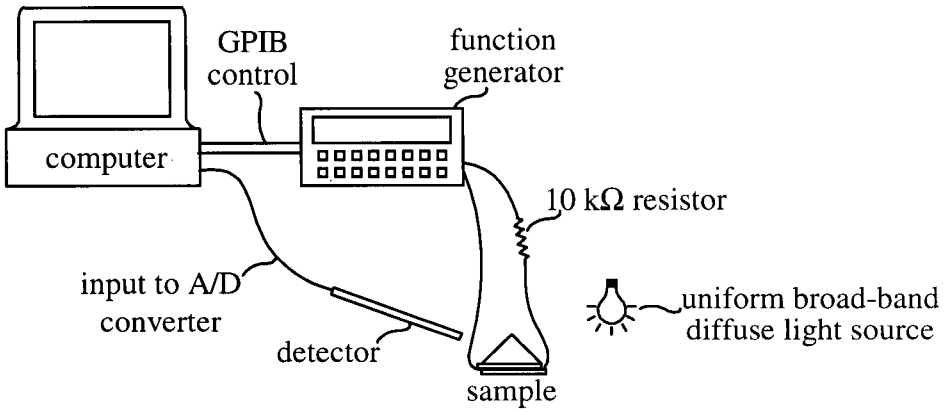

Figure 5-3. Schematic diagram of data acquisition system

The control program was written using Visual Basic programming language. Initially, the waveform shape, frequency and amplitude for the function generator were selected, as well as the desired sample rate of the reflectance measurements. The voltage was applied across the cell by the function generator, and the data acquisition system sequentially sampled the applied voltage and the optical sensor amplifier voltage and recorded the measurements, with the corresponding time step, in a data file. In some of the experiments, the voltage across a 10 kΩ resistor connected in series with the test cell was also recorded, providing a measurement of the current flow through the cell in response to the applied voltage. This control and data acquisition system was used to generate all the data plots presented in this chapter.

In many of the experimental results presented here, the wavelength range of the incident light was restricted by placing a multi-layer, spectrally selective transmission filter in front of the collimating tube of the photodetector apparatus, as depicted in Figure 5-4. Three filters, blue, green and red, with peak transmittance at 475 nm, 515 nm and 660 nm, respectively, were used in these experiments. The complete spectral transmittance characteristics for these filters are provided in Appendix H.

In addition to the coloured filters, an infrared filter was affixed to the end of the collimating tube. As shown in the specification of the optical sensor in Appendix H, the detector is primarily responsive in the infrared band, from 700nm to 800nm, which causes a significant signal in response to radiation with wavelengths well outside the visible range of interest in

this study. The IR filter, whose transmittance characteristic is also shown in Appendix H, reduces the signal due to incident IR radiation, therefore maximizing the signal due to radiation within the visible band.

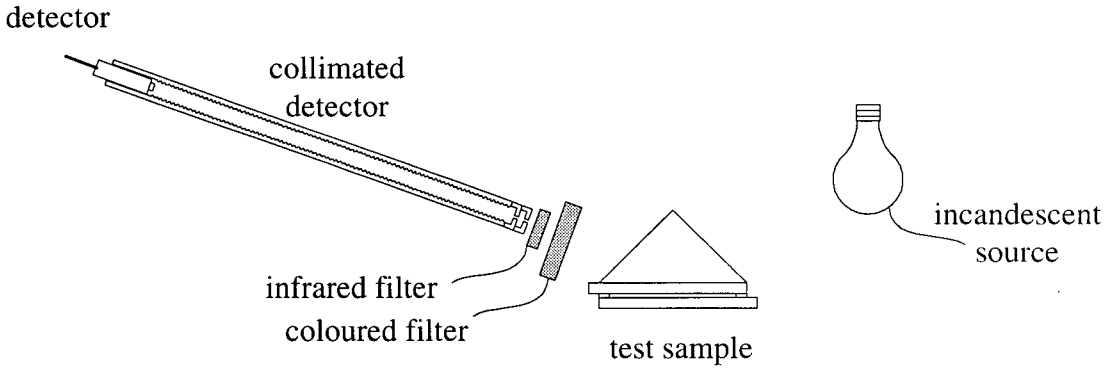

Figure 5-4. Position of filters

For each of these experimental trials, a diffuse, incandescent bulb powered by a regulated DC power supply was used as the light source. The luminance of this source, as a function of wavelength, is shown in Appendix I. The source was placed approximately 0.2 m from the facet of the prism attached to the test cell, as depicted in Figure 5-4, and the height of the bulb was adjusted so that the brightest region of the bulb surface was aligned with the detector, to maximize the level of illumination and thus, maximize the signal from the optical sensor.

In the preceding discussions, numerous factors have been mentioned that influence particle behaviour, including the waveform, voltage, and frequency of the applied voltage and the wavelength and the angle of incident light. A review of all possible permutations of these factors would be very lengthy and of little value. Rather, a representative sample of these combinations is provided in the next section to facilitate a better understanding of the overall system behaviour.

5.3 Time-varying reflectance modulation

A useful presentation of the frustrated TIR system shows the reflectance changing as a function of time, in response to a specified time-varying electric field, for example a square

wave. This is particularly relevant to the application of the particle systems to a reflective image device, where time-varying control of the reflectance is a key feature.

Figure 5-5 shows a representative plot of reflectance versus time in response to a square wave applied voltage waveform, of frequency, f=0.1 Hz and amplitude, V_p=10 V. The suspension used in this system contained carbon black particles, approximately 120 nm in diameter, prepared as described in Section 3.7, contained in a cell constructed with a top flat surface and a rear micro-prismatic surface. The average gap thickness was 30 μm and the active area was 900 mm^2. The electrophoretic mobility, μ, of these particles is approximately $1x10^{-10}$ $m^2V^{-1}s^{-1}$, so under this applied field of $1.7x10^5$ Vm^{-1}, the particles will move at $1.7x10^{-5}$ ms^{-1} thus it will take an average particle about 1.7 s to cross the gap thickness. (Real displays would use smaller gaps to achieve faster response, ultimately limited only by the 0.25 μm effective thickness of the evanescent wave itself.)

A green filter, with a transmission peak at 515 nm, was placed in front of the detector, and the collimated detector tube was positioned at $\phi = 68°$, corresponding to an angle of incidence at the TIR interface of $\theta = 60°$, 1.7° greater than the critical angle, ensuring that TIR will occur. The overall reflectance of the system was somewhat reduced by the bulk absorption in the prism, the glass slides, and the ITO coating. The exact absorption factor varied from sample to sample, but these factors together resulted in a loss of at most 10%. In the data presented in this chapter, the normalized reflectance was calculated as the ratio of the optical sensor voltage to the maximum voltage measured with the same optical configuration, but no black particles present in the suspension. This normalization procedure takes into account the light loss resulting from the external factors.

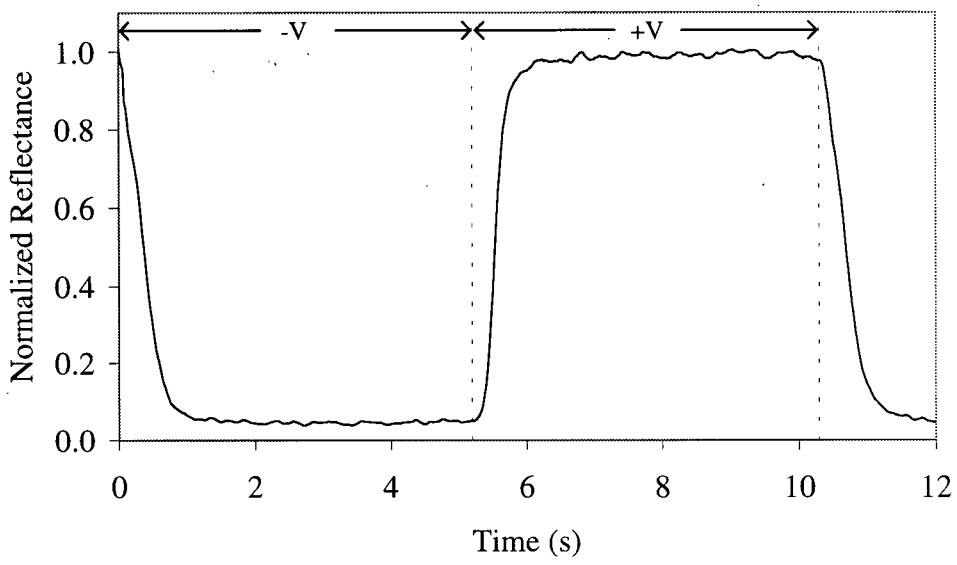

Figure 5-5. Reflectance modulated by electrophoresis of black particles

Referring to the plot in Figure 5-5, initially, at time $t<0$, the applied voltage was +10 V, corresponding to an applied electric field of 1.7×10^5 Vm^{-1}, and the positively-charged particles were therefore held near the rear of the cell, well outside the evanescent wave region, resulting in a maximum reflectance of 1.0. At time $t=0$, the applied field was reversed to -1.7×10^5 Vm^{-1} and the particles migrated across the cell. As they migrated, they entered the region near the TIR interface and absorbed some of the incident light. (It is important to note that if the test cell had been constructed using two flat surfaces, the gap thickness would be uniform, and there would be a measured time delay as the particles migrated across the gap before entering the optically active evanescent zone. However, this particular sample was constructed using a micro-prismatic rear surface, which resulted in a highly non-uniform gap thickness. When the direction of the applied field was reversed, particles in the narrowest region of the gap migrated almost immediately into the evanescent zone, so no time delay was observed.)

The degree of absorption increased as the number of particles near the interface increased. By $t=1.0$ s, the reflectance reached a steady state of 0.05. At $t=5.2$ s, the applied field was restored to 1.7×10^5 Vm^{-1}, and the particles pulled away from the TIR interface. By $t=6.2$ s, the maximum reflection was again reached.

The time required to switch from the maximum reflectance state to the minimum reflectance state depends on the electrophoretic mobility of the particles (and hence their size and electrostatic charge), as well as the magnitude of the applied field. However, this is a complicated function since the reflectance changes only when the particles move within the optically active region near the interface, resulting in a non-linear relationship between reflectance and position. This is further complicated by the fact that the reflectance depends not only on the number of particles near the interface, but also on their distribution. Despite these complications, the time required to achieve the minimum reflectance provides an indication, but not a direct measurement, of the electrophoretic mobility.

As mentioned above, the minimum reflectance is reached after approximately 1.0 s. The average distance traveled by a particle in the cell is about 30 μm, corresponding to an average electrophoretic mobility of about 2×10^{-10} $m^2V^{-1}s^{-1}$. (It should be noted that, as discussed in more detail in Chapter 6, the particles almost certainly slow down as they move closer to the surface, so this estimate of mobility is probably somewhat less that the bulk value.) The electrophoretic mobility has been similarly calculated from time-varying reflectance data for the cyan, magenta and yellow particle suspensions formulated for this study, and these estimates compared favourably with value of 1.6×10^{-10} $m^2V^{-1}s^{-1}$ estimated from the visual separation experiment described in Section 3.7. The mobility estimates are provided in Table 5-1.

Particle colour	Electrophoretic mobility estimate $m^2V^{-1}s^{-1}$
Black	1.8×10^{-10}
Cyan	3.5×10^{-10}
Magenta	1.4×10^{-10}
Yellow	1.2×10^{-10}

Table 5-1. Electrophoretic mobility estimates

Figure 5-6 demonstrates modulated reflectance at a much higher frequency of 20 Hz. In this experiment, the magenta particles were contained in a test cell with an average gap thickness

of about 20 μm, and subjected to an applied field of 1.3 x 10^6 V/m. A reflectance modulation of about 35% was observed.

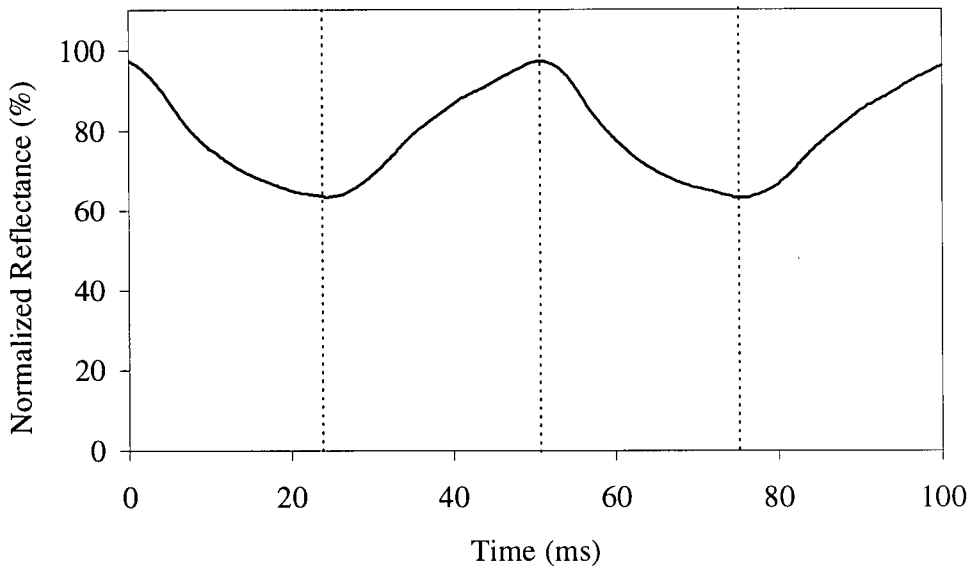

Figure 5-6. Higher frequency modulation of TIR

Under this field, the system should reach the minimum reflectance state after about 100 ms, but it is clear from the plot in Figure 5-6 that at this modulation frequency, full reflectance modulation is not achieved.

A maximum response speed was tested for a number of samples and it was found that in a number of cases, the response time was about an order of magnitude longer than anticipated. In Section 3.7, it was explained that these experimental suspensions are formulated using a liquid dispersant. In fact, an excess quantity of dispersant was used, as it seems to be necessary to prevent irreversible deposition of particles on the electrodes. It is postulated that these excess dispersant molecules may also be responsible for the anomalously slow switching speed by forming micellar structures that impede the movement of the particles near the interface. This is a complicated issue that is not investigated in detail in this thesis. However, the same phenomenon is thought to be responsible for some interesting field-dependent effects discussed in detail in Section 5.5.1.

The measurement of reflectance as a function of time, in response to an applied field, will be the primary format for analyzing particle behaviour throughout the rest of this chapter.

5.4 Measurement of current flow and charge transfer

The movement of the pigment particles was apparent in the previous section in terms of the light absorption caused by the particles as they moved in response to an applied electric field. Since these particles are electrostatically charged, their movement can also be observed in terms of the current, or flow of charges, in the cell. The current through the cell was measured by recording the voltage across a 10 kΩ resistor connected in series with the cell. Based on the simple Ohm's law relationship, $V=IR$, the current through the resistor, and hence through the cell, was calculated.

In order to interpret the current measurements, it will be helpful to briefly review the electrostatic problem of a charge distribution moving within a parallel plate capacitor. Figure 5-7 shows this situation, where charge q is distributed on the particle as a uniform planar distribution, and is positioned a distance x from one side of a parallel plate capacitor of area A and gap d.

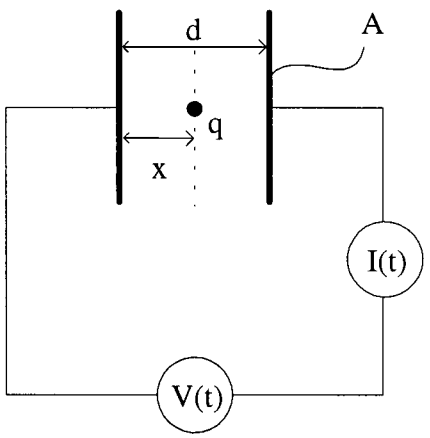

Figure 5-7. Parallel plate capacitor system

The capacitance is still given by:

$$C = \varepsilon_o \frac{A}{d} \qquad \textbf{(5-1)}$$

but the surface charge q modifies the charge on the plates, such that the charge displacement in the capacitor, Q, is given by

$$Q = CV + q\frac{2x}{d} \tag{5-2}$$

Interestingly, this means that the motion of charged particles in the capacitor cause movement of charge in the external circuit, just as if they were "part of" the circuit itself.

Differentiating (5-2) with respect to time yields the expected current:

$$I(t) = C\frac{dV(t)}{dt} + 2\frac{q}{d}\frac{dx}{dt} \tag{5-3}$$

Thus, a square wave applied voltage would be expected to generate a brief current spike, followed by a current corresponding to the particle motion.

Figure 5-8 shows that the current measured in a typical cell is consistent with this prediction. The current increased dramatically when the direction of the field was reversed, since all of the electrostatically charged particles and ions in the cell moved in response to this field. The initial pulse associated with the capacitive term in (5-3) above occurs on a time frame shorter than the measurement interval and does not appear in this data, as was verified by carrying out the same measurement in a cell containing no particles. The initial electrophoretic current typically reached a peak of greater than 4 μA, and died off after about 1.0 s. The reflectance data, superimposed on the current data, shows that the minimum current flow and maximum absorption were achieved at the same time, further indicating that this peak current was the result of the motion of the electrophoretic particles. When all of the particles reached the region near the TIR interface and stopped moving, they could no longer contribute to the cell current.

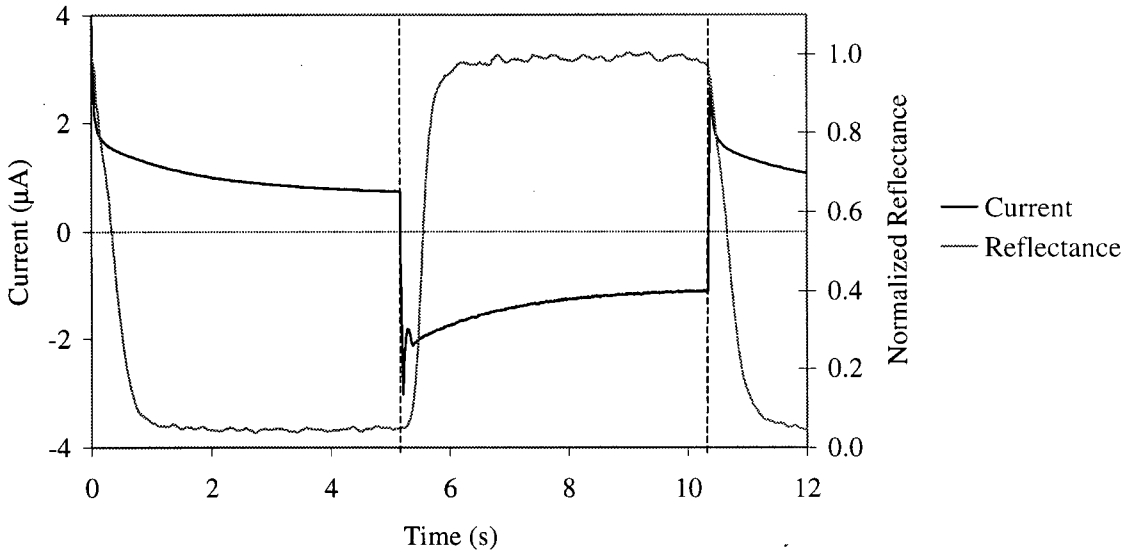

Figure 5-8. Comparison of reflectance and current

In a perfectly insulating suspension, the current flow would drop to zero once the particles stopped at the opposite side of the cell. However, as seen in Figure 5-8, there is a residual current of about 1 μA, corresponding to a residual conductance of about $3x10^{-15}$ $\Omega^{-1}m^{-1}$. This residual current could persist for a long period of time, in excess of three hours at least, although it did seem to drop very slowly over very long times.

It is possible that this residual current is caused by unnecessary conductive species in the suspension, likely resulting from the formulation process. At some point, it would be desirable to further investigate this residual conductivity, both out of curiosity and because it would cause an undesirable power draw and possibly chemical degradation of the electrode surfaces. However, for the purposes of this thesis, the residual current does not affect the results and will not be further addressed.

5.5 Factors influencing reflectance modulation

As mentioned previously, the behaviour of electrophoretic pigment particles in a reflective image device is influenced by a number of factors. This section explores the effect of varying those factors that can be externally controlled.

5.5.1 Intensity of applied field

As described in Section 2.4.2, the speed at which the electrophoretic particles move depends on the magnitude of the applied field. In the case of a reflective image device, it was expected that this dependence would be apparent in terms of the optical switching rate.

5.5.1.1 Square wave field variation

To confirm that the switching speed depended on the field strength, the amplitude of an applied square wave voltage signal was varied between $1.7x10^4$ Vm^{-1} and $1.7x10^5$ Vm^{-1}, for the system of 120 nm absorptive carbon black particles, at a wavelength of 500 nm and incident angle θ=60°.

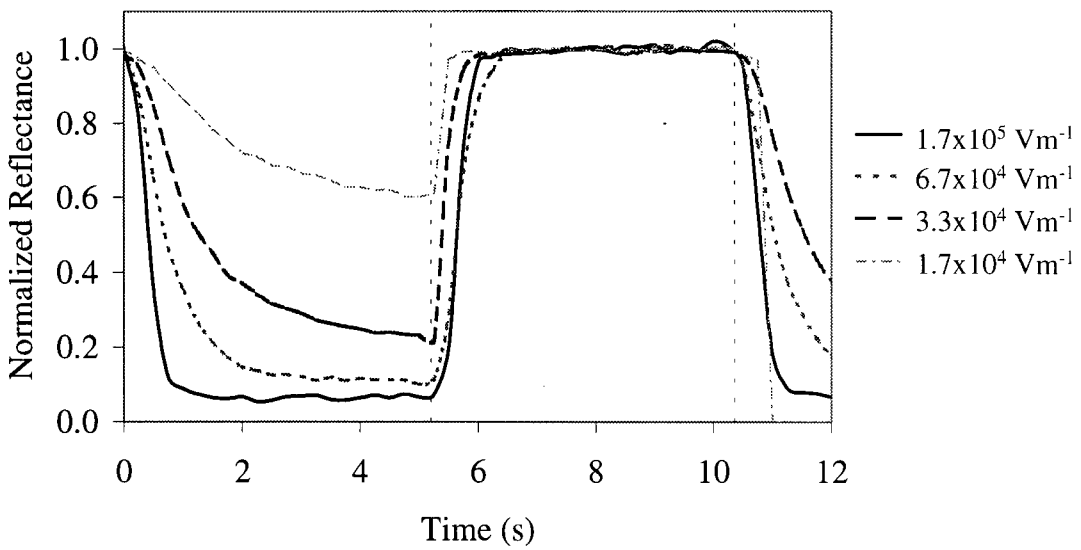

Figure 5-9. Reflectance versus time for various intensities of applied field

The time required for the system to change reflectance states was indeed longer for weaker fields. Based on this data, Table 5-2 presents the approximate time required to reach the minimum level of reflectance. Although the electrophoretic mobility of the particles is generally considered to be a constant, this does not necessarily imply that there would be a simple relationship between the field and the time to reach the minimum reflectance. The interaction of the light rays with the layer of particles at the interface is complicated, since it depends not only on the number of particles, but also on their density of packing, as

discussed in detail in Chapter 6. Furthermore, since the density of the particle layer may depend on the strength of the applied field, it is not practical to predict the exact time required for the system to achieve the maximum absorption state for a given applied field. However, the times measured at these four different field strengths indicate that the particles do move more slowly as the field is decreased.

Field magnitude (Vm^{-1})	Time to reach minimum absorption (s)
$1.7x10^5$	1.1
$6.7x10^4$	2.2
$3.3x10^4$	3.5
$1.7x10^4$	4.7

Table 5-2. Estimate of switching time in response to different fields

One surprising result from this experiment is an additional field-dependent characteristic of this particle system. It can be seen in Figure 5-9 that the eventual steady-state reflectance level reached by this system depends on the intensity of the applied field. This is counterintuitive, as one might expect that in a purely field-driven electrophoretic system, even a very weak applied field would cause the particles to eventually move into the optically active region near the interface and yield a minimum reflectance state, that is independent of the applied field. (The minimum reflectance value that can be achieved by this system, about 6%, is represented by solid black line in Figure 5-9. The field magnitude of $1.7x10^5$ Vm^{-1} was experimentally determined to be the minimum field required to reach this absorptive state, and higher field magnitudes were shown to produce the same overall result.) The observed field-dependent effect may be especially useful in producing intermediate reflectance levels, as was discussed in Section 3.9.

The reasons for this effect are not yet known. One possibility is that the excess dispersant molecules used to prevent the film formation self-assemble into micelles that in turn coat the surfaces. According to this model, as the particles moved toward the interface, they would encounter a layer of these micelles and, under a weak electric field, the particles would not be able to force through the micellar layer to occupy a position closer to the TIR interface. As the field strength was increased, the particles would embed themselves further into the layer, moving closer to the interface and thus absorbing more of the incident light.

While this field-dependent effect could be important for use as a grey scale control mechanism in actual displays, the determination of the exact nature of the mechanism lies outside the scope of this thesis.

5.5.1.2 Time-varying triangular wave field

The field-dependent behaviour of the particles was further explored by applying a field that cycled linearly from $-3x10^5$ to $+3x10^5$ V/m, at a rate of about $5x10^3$ $Vm^{-1}s^{-1}$, (corresponding to a very low oscillation frequency of $8x10^{-3}$ Hz) such that essentially steady-state reflectance values are achieved at each field value. The resulting curve in Figure 5-10 clearly shows a hysteretic behaviour. This example used magenta particles, measured at a wavelength of 650 nm, at $\theta = 60°$.

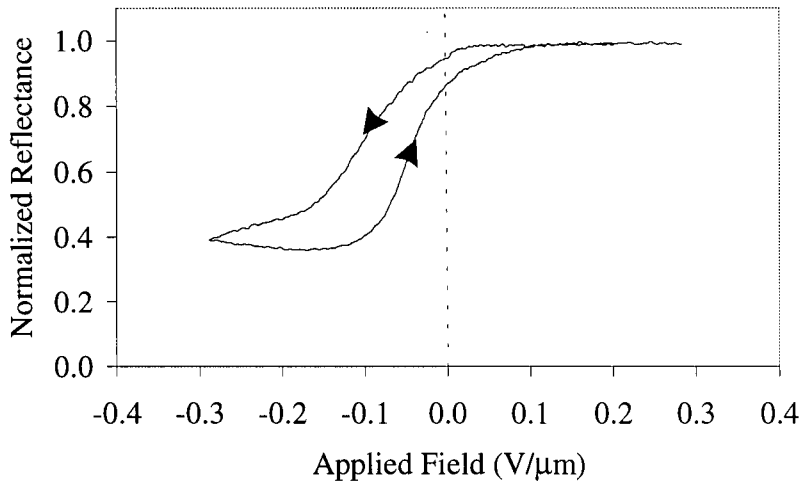

Figure 5-10. Reflectance in response to slowly varying applied field

The non-zero width of the hysteresis curve indicates that there is some effect that prevents the particles from freely moving away from the interface until a sufficiently strong reverse field is reached. Returning to the possibility of micellar structures coating the surfaces, these micelles could be responsible for this second effect as well. Again, although this behaviour could be an important area for further study, it will not be further investigated in this thesis. The effect of varying the number of particles in the system was considered next.

5.5.2 Concentration of particles

In the simplest view of the absorption of incident light by frustrated TIR, one would expect that to achieve maximum absorption, particles would have to be packed into the very thin evanescent wave region so that they could absorb the light. This would imply that for effective absorption, the particles would require absorption coefficients of order 10^7 m^{-1}, since the absorption would occur over a sub-micron distance. This has substantial practical implications, so a first step was to check the validity of this simple view.

In that regard, there is a simple implication that can be tested. In the angular range explored in this experiment, the evanescent wave thickness is about 0.25 μm. In the carbon black suspension, where the particles have an average diameter of about 0.12 μm, this means that at most two layers of particles would be required for maximum frustration of TIR. This hypothesis was tested by varying the quantity of carbon black particles in the cell, over a wide range, and comparing the resulting reflectance levels.

This study required an estimate of the number of particles present in one packed layer at the interface, which depends on both the size of the particles and the extent to which they pack closely together. As explained in Section 2.4.3, it is difficult to determine exactly the size of the particles, but a reasonable estimate was obtained from dynamic light scattering experiments. The exact packing fraction of the particles in a uniformly packed layer at the interface is unknown but, again, a reasonable estimate is that the particles will pack with a packing fraction of about 0.3. With these two estimates, the number of particles required for one layer was calculated. The area and volume of the cell were measured to be 9.0×10^{-4} m^2 and 5.4×10^{-8} m^3, respectively. Similarly, the cross-sectional area and volume of an average particle were estimated to be 1.1×10^{-14} m^2 and 8.6×10^{-22} m^3, respectively. As a result, the number of particles in one layer at the TIR surface of the cell is about 6.3×10^{10}, corresponding in this cell to a particle concentration of about 1.4×10^{-3} $g\,ml^{-1}$.

The reflectance was measured, using the time-varying reflectance measurement procedure described in Section 5.2, for three different particle concentrations: 2.8×10^{-4} $g\,ml^{-1}$, corresponding to 20% of a complete layer at the interface, 2.8×10^{-3} $g\,ml^{-1}$, or 2 layers, and 2.8×10^{-2} $g\,ml^{-1}$, or 20 layers. If the simplistic absorption model described above was correct,

the level of absorption achieved for the 0.2 layer case would be about 10% of the maximum value which should be achieved by both the 2 layer concentration (which fills the evanescent wave), and also the 20 layer case. That is, the additional 18 layers in the 20-layer system would be superfluous and would have no effect.

The response curves for these three particle concentration levels are shown in Figure 5-11. There is a slight degree of absorption, about 5%, by the 0.2 layer concentration of particles. With approximately 2 layers of particles, there is improved absorption, around 30%, but it is still very limited. The highly concentrated suspension, on the other hand, shows a very dramatic increase in absorption, to greater than 90%. This is the maximum level possible for this system and further addition of particles has no effect.

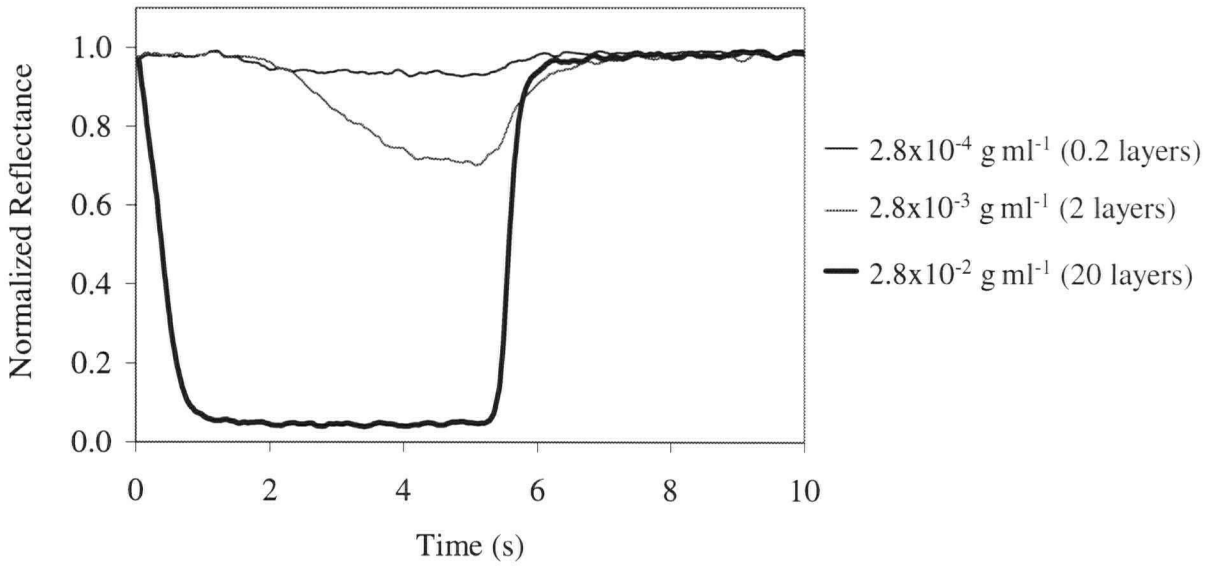

Figure 5-11. Modulation by different concentrations of particles

Clearly, the evanescent wave description of frustrating TIR by a very thin layer of highly absorptive particles is insufficient to describe the absorption behaviour summarized in Figure 5-11. As will be explained in Chapter 6, the absorption is thought instead to result from longer-range optical paths through a density gradient of moderately absorbing particles.

5.5.3 Wavelength of incident light

As described in Section 2.1.3, the evanescent wave penetration depth is directly proportional to wavelength. In this research, at the interface between the perfluorinated hydrocarbon liquid and glass, the penetration depth at an incident angle of 63°, (about 5° greater than the critical angle), is 0.23 μm for red light, whereas for blue light it is about 0.17 μm. The angular dependence of the penetration depth at different wavelengths is shown in Appendix J. The simple view of absorption "in the evanescent wave" would suggest that the absorption would be wavelength dependent as a larger evanescent wave would yield a larger effective path length for absorption. Therefore, this hypothesis was explored as well.

For this purpose, the carbon black suspension, with a high concentration of particles (2.8×10^{-2} g ml^{-1}), was contained in a test cell exactly as described in the previous sections. The time-varying reflectance was measured using the experimental approach described in Section 5.2, with coloured filters in front of the collimated detector. Three specific coloured filters, blue, green and red, were used, having peak transmittance values at 475 nm, 515 nm and 600 nm, respectively. (The spectral transmittance characteristics of these filters are provided in Appendix H.) Carbon black particles were used as the absorptive material for this experiment since they absorb light equally well for all wavelengths in the visible band so that any variation of the absorption as a function of wavelength would be a result of the interaction with the particles and not the particles themselves. The results of the experiment are shown in Figure 5-12.

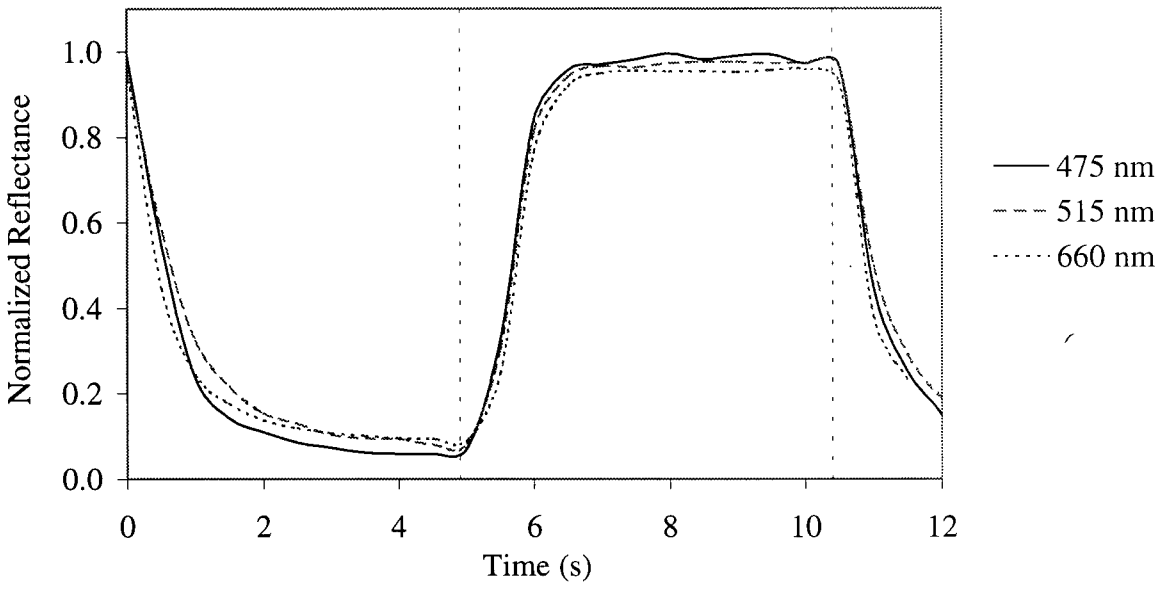

Figure 5-12. Reflectance at different wavelengths of incident light

It is clear from these reflectance measurements that there is virtually no difference in the response of the system for the three different wavelengths of incident light. This further shows that the simple "evanescent wave absorption" view fails to describe the absorption as the particles move into optical contact with the TIR interface. Chapter 6 presents a more complete description that resolves this apparent inconsistency.

Carbon black particles were used in this experiment because of their wavelength-independent absorption characteristics. However, as indicated by the discussion in Section 3.12, particles that selectively absorb light in selected wavelength bands would be required in a full-colour reflective image device. The capabilities of the cyan, magenta and yellow pigment particle suspensions that were developed for this purpose were demonstrated in Section 4.2.2. There, the reflectance of a test sample was reported as a function of wavelength, but without time resolution. In the following section, the reflectance measurements, as a function of time, are presented for the same three coloured suspension samples.

5.5.4 Particles with different spectral absorption characteristics

The time-varying reflectance was measured in order to compare the effect of particles with different spectral absorption characteristics at the same wavelength of incident light. Specifically, the cyan, magenta and yellow suspensions were contained in separate test cells, and the reflectance of red light, with peak intensity at 660 nm was measured, as depicted in Figure 5-13. The concentration of particles in each test cell had been adjusted so that an estimated twenty layers of particles were packed along the interface when the system was held in the absorptive state.

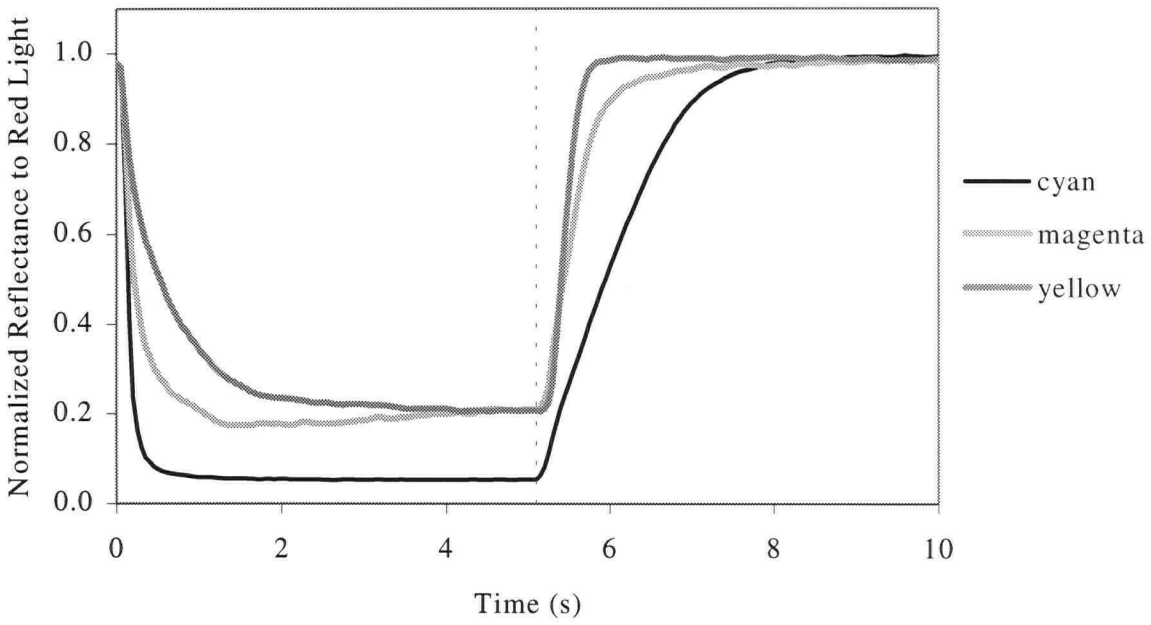

Figure 5-13. Modulation by particles with different spectral absorption

As anticipated, the cyan suspension showed the maximum level of absorption, consistent with the spectral transmittance characteristics shown earlier which has a high level of absorption in the red band. The magenta particle suspension also showed significant absorption in the red band, as did the yellow suspension. These results are consistent with the steady state measurements reported in Section 4.2.2, as were the analogous measurements under green and blue light.

This experiment demonstrates electrophoretic behaviour for all three pigments that is somewhat similar, a result that is not surprising since the same dispersant was used in each sample. However, since the particle chemistry differed substantially in each case, this result was by no means assured. Not surprisingly, the switching speed and saturation behaviour differ somewhat, presumably because each type of particle has a different mean size and shape.

Up to this point, all of the time-varying reflectance measurements were taken at a single incident angle of θ=60°, slightly greater than the critical angle of θ_c=58.3°. The next section reports reflectance measurements in response to variation of the incident angle.

5.5.6 Reflectance at different angles of incidence

The time-varying reflectance was measured for a number of incident angles. Again, the same test sample of carbon black particles was used, as described in Section 5.3. The time-varying reflectance response was measured at twelve different angular positions, between θ=60° and θ=69°. (Beyond θ=69°, the measurements become geometrically impractical, as described in Section 5.2.) From this data, the reflectance values were compiled at different time intervals following a change in the applied field that caused the particles to move toward the interface. These results are shown in Figure 5-14. Again, the carbon black particles were used to frustrate TIR, and the peak wavelength of detected light was chosen to be λ=515 nm, approximately in the center of the visible band. It is important to note that these measurements were all taken on the same cell, and that it was in what might be called a "dynamic steady state" response to the applied square wave voltage. Although the response at the different angles could not be measured simultaneously, they were extremely reproducible, so the variation in response from angle to angle, while small, are definitely real and must be explained.

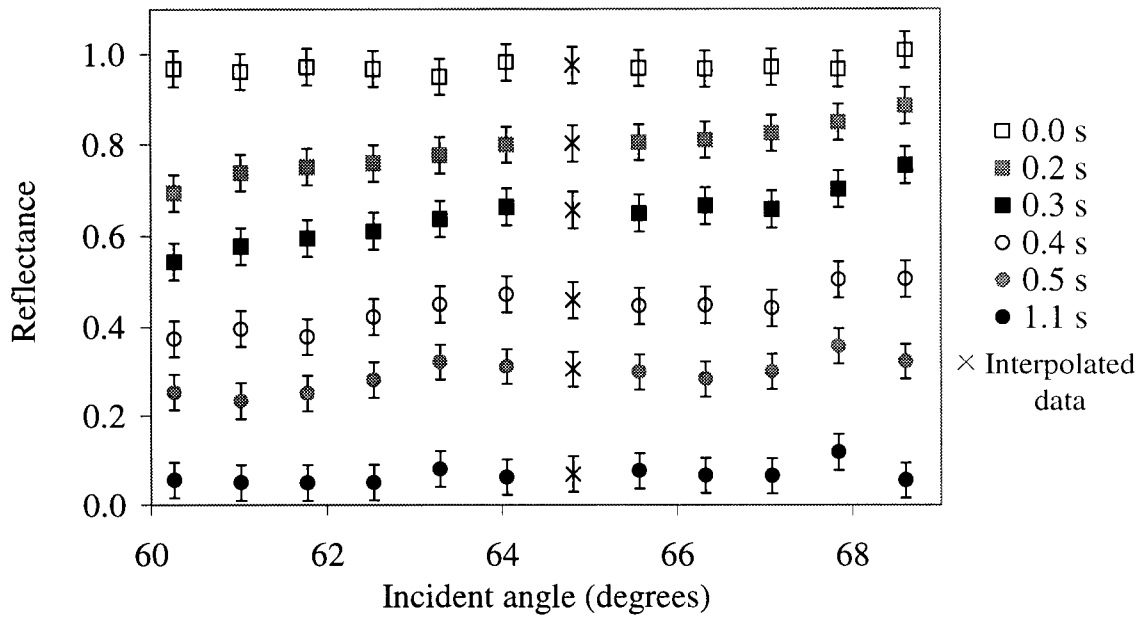

Figure 5-14. Reflectance at different angles of incidence

Prior to time t=0 s, the particles were pulled away from the interface by the applied electric field, and the reflectance value was maximum, consistently near 100% for all incident angles. At t=0 s, the appropriate voltage was applied to pull the particles toward the interface. As time progressed, more particles moved toward the interface, and the reflectance level decreased until, finally, at t=1.1 s, the reflectance reached a minimum value of about 6%.

As depicted in Figure 5-14, there was a definite increase in reflectance (in other words, a decrease in the amount of absorption) as the incident angle increased. Since the reflectance was shown in Section 5.5.3 to be independent of angle, variations in the evanescent wave penetration depth across this range cannot be responsible for this angle-dependent result, since if the penetration depth were key to the level of absorption, there would be an equally strong wavelength dependence. Clearly, some other mechanism is responsible for this behaviour, and a more sophisticated understanding is required. This is the subject of the next chapter.

6 MODELLING THE PARTICLE DYNAMICS

Section 3.8 presented a simplistic description of absorption of light by electrophoretic particles moving into the evanescent wave zone associated with TIR. This view would suggest that the degree of absorption should be determined by the number of absorptive particles that could pack into the thickness of the evanescent wave. This would predict absorption that is largely independent of incident angle, but substantially dependent on wavelength. Further, there would be no dependence on the number of particles, as long as there were enough to fill the evanescent wave zone. Briefly, the measurements presented in Chapter 5 were inconsistent with all three of these expectations. The absorption was *not* wavelength dependent (unless coloured pigments were used), *were* angle dependent, and maximum absorption required a particle layer ten times the thickness of the evanescent wave.

A consistent, and intuitively reasonable, alternate model has been developed to explain the observations. This model is based on the assumption that as the particles migrate toward the interface to frustrate TIR, they form a density distribution in the liquid that is highest near the interface and decreases toward zero away from the interface. Since these pigment particles have a much higher index of refraction than the surrounding liquid, they locally increase the effective index depending on the fraction of the total volume that they occupy, as explained in detail in the following section. Therefore, variations in the particle density near the interface result in corresponding variations in the effective refractive index in this region, which alters the optical properties at the interface and influences the behaviour of incident light rays.

A reasonable model for this density distribution, incorporating a distribution of particles with a maximum density at the interface and tapering approximately exponentially to zero, has been developed to correctly predict the reflectance as a function of angle, in good agreement with the results presented in Section 5.5.6. This model is described in detail in this chapter. As well, the reflectance predictions resulting from a number of alternate particle distributions are compared with the experimental data, to demonstrate that these distributions do not adequately explain the observed behaviour, suggesting that the proposed distribution is likely to be approximately correct.

6.1 Modelling optical path length with continuous index variations

To describe this interpretation of particle behaviour, it is useful to consider the effect on the local refractive index in a region of a distribution pigment particles. The real component of the refractive index of these particles is fairly high, typically between 1.8 and 2.2,[81] and they are moderately absorptive, with a small but significant imaginary component of about 0.2 at their peak absorption wavelength. Since the particles are sub-optical in size, the combination of these small, highly refractive particles surrounded by the low index liquid results in an overall effective index, n_{eff}, for the region which is greater than that of the index of the fluid itself. Determining the exact value of n_{eff} requires a complicated calculation based on the size, shape and location of the individual particles, and little would be gained from performing this calculation here. However, the value can be reasonably approximated by estimating the index contribution of the particles in terms of the fraction of the total volume they occupy. The approximate value of n_{eff} can be expressed in terms of the volume fraction, f, the index of the particles, n_p, and the index of the liquid, n_l.

$$n_{eff} \cong (1-f)n_l + fn_p \qquad \textbf{(6-1)}$$

This estimated value can be used to predict the path a light ray will follow when encountering the interface.

A high density of particles at the interface can substantially change its optical properties. If the particles are not present at the interface, a light ray with an incident angle slightly greater than the critical angle will undergo TIR and only the energy associated with the evanescent wave will penetrate into the second medium. However, the presence of these particles changes the interfacial optical properties and the conditions for TIR, so that a transmitted ray actually passes into the second medium for a while. This ray travels through the absorptive particle region, attenuating along its path, until it reaches the region of low-index fluid containing no particles. At this point, the conditions for TIR are met, so the light ray reflects and returns through the particle layer. This is a more complex picture for frustrated TIR in that the particles influence the distribution of the electromagnetic energy that they then absorb, but it is quite feasible to model this mathematically, as will be shown below. The degree of absorption thus depends on the length of the ray path through the absorptive

particle layer, and since the path is determined by the incident angle as well as the effective refractive index of the particle layer, it seems quite reasonable that the absorption will exhibit both angular-dependent and concentration-dependent behaviour.

The behaviour of the light ray as it interacts with the layer of particles near the interface depends on the effective index in this region, which in turn depends on the distribution of particles. To understand this behaviour, it was important to develop an appropriate model that described how the ray path changed as a function of incident angle as the distribution evolved over time. In the following sections, a number of possible particle distributions were modeled and evaluated based on the level of absorption predicted under certain conditions.

In each of these models, several parameters were held constant. In particular, dielectric constants and corresponding refractive index values were assigned to the various materials in the system, as detailed in Table 6-1. The real and imaginary components, ε_r' and ε_r'', of the dielectric constant (corresponding to real and imaginary components of the refractive index, n' and n'', as in (2-3)) for the particles were chosen as typical values for the pigments studied in these experiments.

Material	Dielectric constant		Refractive index	
	ε_r'	ε_r''	n'	n''
Solid	2.25	0.00	1.50	0.00
Liquid	1.61	0.00	1.276	0.00
Particles	4.00	0.05	2.00	0.22

Table 6-1. Dielectric constants and refractive index values for materials

For each model, the path followed by a light ray was determined by numerical integration. The rays encountered regions of locally different refractive index values and the cumulative degree of absorption was calculated. Specifically, the differential form of Snell's law was applied to calculate the angle of the ray at incrementally different positions along the path. By using a sufficiently small increment, the total path length and the associated degree of absorption in each case were quite accurately predicted. The details of this calculation are explained in Appendix A.

The first particle distribution to be considered was a layer of particles with uniform density and a thickness that increased over time as the particles migrated toward the interface, as described in Section 6.2.

6.2 Uniform density particle layer

The simplest possible particle distribution would be one in which the particles pack into a surface layer with a constant volume packing fraction of f_{max}, as depicted schematically in Figure 6-1. As time, t, increased, the thickness of this layer, a, would increase as more and more particles migrated to this layer.

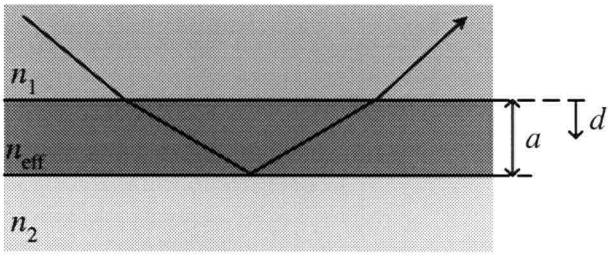

Figure 6-1. Uniform density layer of particles

This is schematically depicted in Figure 6-2, where the particle layer has a thickness a_i at time t_i.

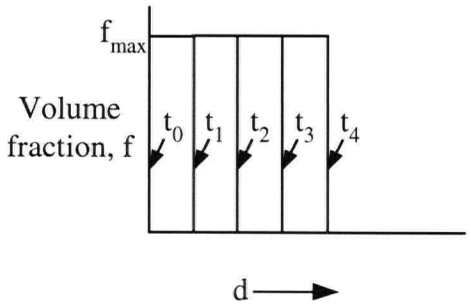

Figure 6-2. Increasing thickness of uniform density particle layer with time

The particle layer causes an increase in the effective index near the interface, and the majority of light rays which otherwise would have undergone TIR are instead transmitted through the interface and traveled through the absorptive particle layer. TIR instead occurs

at the interface between the particle layer and the liquid, and the ray travels back through the layer into the index n_1 material. As schematically demonstrated in Figure 6-3, the length of the ray path increases with the particle layer thickness since the ray had to travel a greater distance to reach the liquid layer and meet the conditions for TIR. Since the intensity attenuates along the ray path, the level of absorption increased as time progressed, as expected and as observed experimentally. (This sketch also shows the existence of a partial reflection from the top surface of the particle layer.)

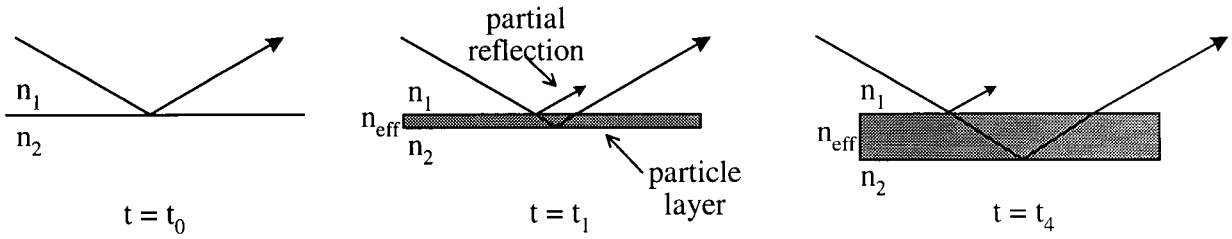

Figure 6-3. Increase in path length as thickness increases

Upon further evaluation, this simple model was found to be inconsistent with the observed angular dependence of the reflectance values. The simple ray diagram presented in Figure 6-4 demonstrates that as the incident angle increases, the path length also increases. As a result, it is expected that a model based on a uniform density layer of particles will predict increased absorption, and therefore decreased reflectance, as the incident angle increases.

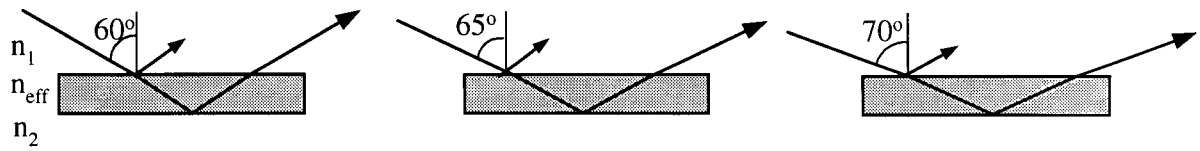

Figure 6-4. Angular dependence on path length in uniform density layer

The reflectance as a function of incident angle was predicted based on this model using Snell's law to determine the angle at which the ray travels through the particle layer, calculating the path length for different layer thickness, and determining the fraction of the light that is absorbed based on the estimated bulk absorption coefficient. (It is worth noting

that while the differential form of Snell's law, as presented in Appendix A, could be used to calculate the ray path in this uniform index layer, the simple form of the relationship in (2-7) is sufficient here.)

The volume fraction of particles, f_{max}, was taken as 0.35, which is a reasonable value for a loosely packed layer of irregularly shaped pigment particles, of varying size distribution. (A tightly packed arrangement of spheres would represent a volume fraction of about 0.75, and it seems reasonable that in a randomly-packed system of mutually repulsive charged particles, the volume fraction would be about half of this value.)

In attempting to model results at successively greater times, the thickness of the model layer was increased to provide the best fit to the data, with the model results shown as lines in Figure 6-5 in comparison to the experimental data points.

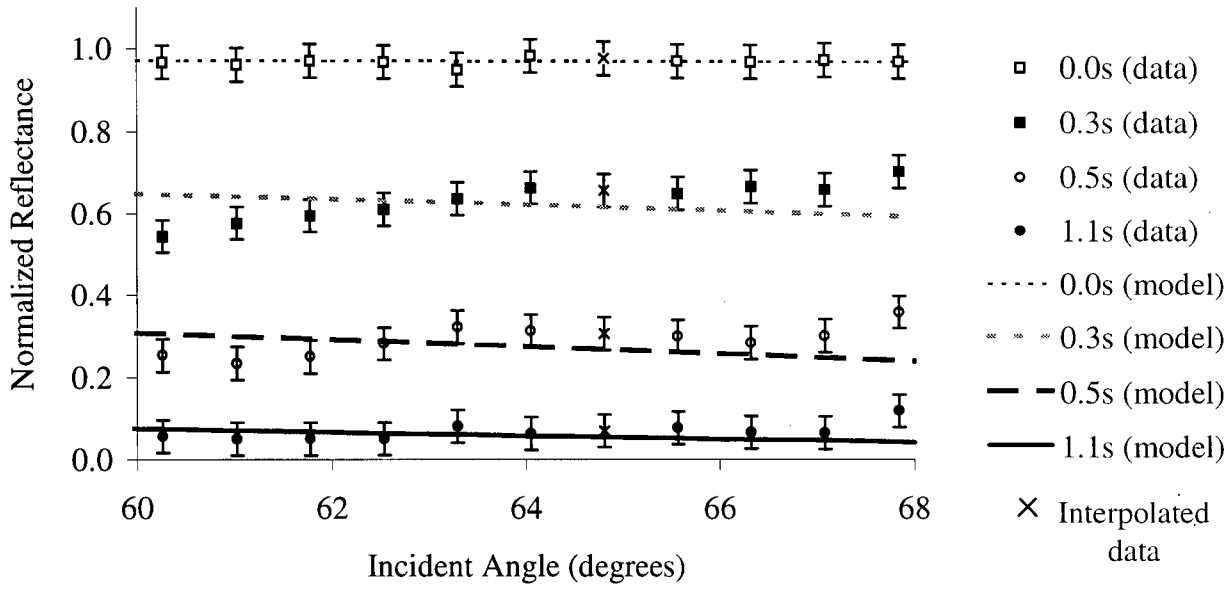

Figure 6-5. Predicted reflectance values using uniform density model

The corresponding particle distributions used to generate these reflectance values are presented in Figure 6-6. It is perhaps worth noting that in each of the models investigated in this chapter, the total volume of the particles increased as the particles migrated toward the interface. Although the total number of particles in a test cell remained constant, only

particles that were close enough to the interface to modify its optical properties were considered as part of the distribution since others did not influence the path of the light ray.

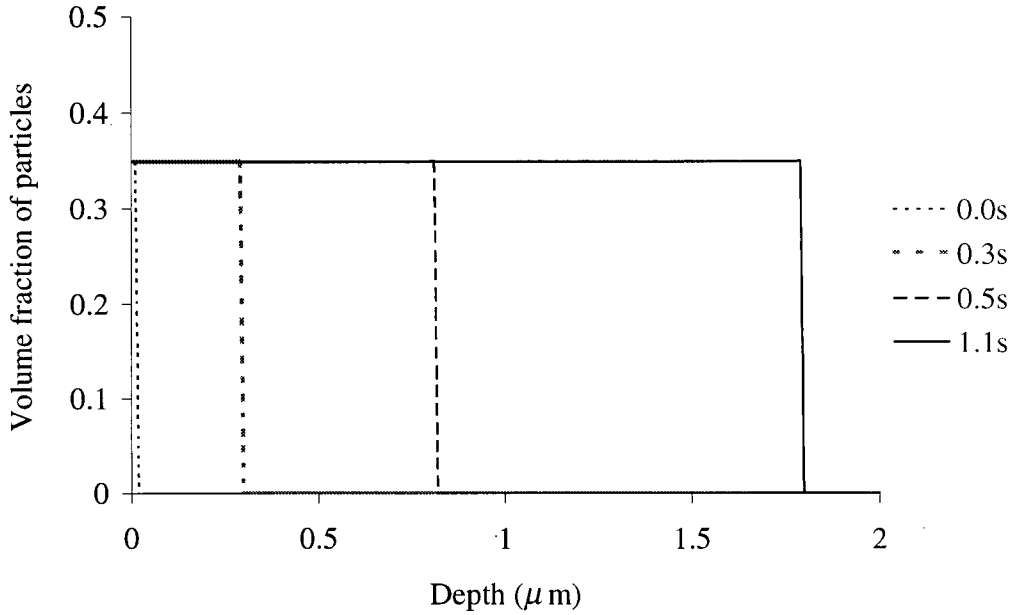

Figure 6-6. Predicted distribution of particles using uniform density model

As shown in Figure 6-5, this model predicts reasonable values of reflectance as a function of angle at the maximum (t=0 s) and the minimum (t=1.1 s) reflectance extremes, but it for intermediate times it incorrectly predicts a decrease in reflectance with increasing incident angle. (This results from the increased path length at greater angles, as mentioned earlier.) Although the increase in the particle layer thickness over time seems reasonable, this model clearly fails to predict the definite observed reflectance increase with angle. Furthermore, in practical terms, there is no reason that the pigment particles would necessarily pack into a layer of uniform density, so it is reasonable to consider some other models incorporating a non-uniform density distribution.

6.3 Non-uniform particle density distribution models

Recognizing that the uniform density particle layer model was insufficient, a number of models were considered based on the assumption that the applied field causes particles to collect at the TIR interface in a layer with a density distribution having a maximum density

near the interface. Intuitively, this seems to be a reasonable assumption, as a particle near the interface could be forced into closer contact with its neighbours by the additional pressure of particles migrating from the fluid into the layer.

The resultant density gradient of higher index particles in the lower index liquid yields a gradient of effective refractive index, and the value of the index can be calculated at specific locations using the relationship described in Section 6.1.

An incident light ray encountering this index gradient will undergo total internal reflection when the ray reaches a location in the particle layer where the effective index is such that the conditions for TIR are met. As a result, TIR occurs at a different position within the particle gradient depending both on the distribution of particles and the angle of incidence. Therefore, as with the uniform density case, it is expected that the reflectance level will depend on both the distribution and the incident angle.

As depicted in Figure 6-7, a ray traveling at a steep angle must travel a relatively long distance into the particle gradient in order to reach a sufficiently low value of effective refractive index that the ray undergoes TIR and returns. Light rays at glancing angles, therefore, need only travel a short distance into the particle layer before the conditions for TIR are met. Consequently, the absorption decreases as the incident angle increases.

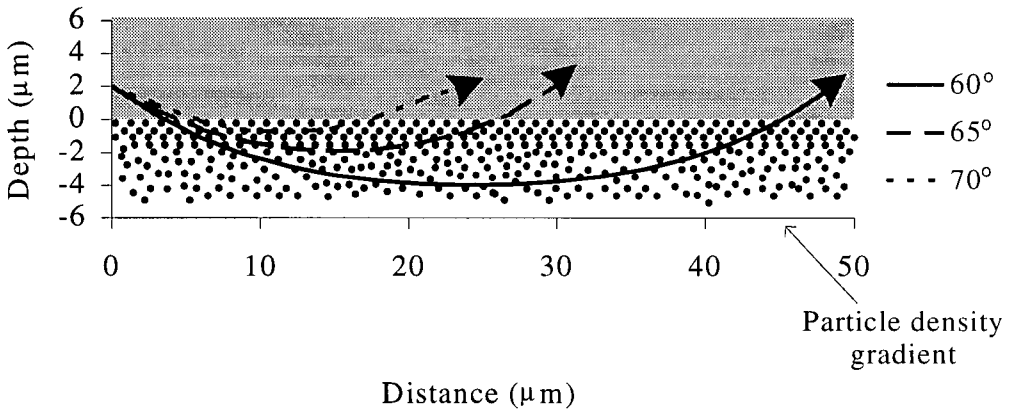

Figure 6-7. Density gradient of particles

It can be seen in Figure 6-7 that the light rays travel some distance parallel to the surface - roughly an order of magnitude greater than the thickness of the index gradient region, between 10 and 50 μm, depending on the incident angle. This shift is small compared to the lateral displacement already arising from the deflection sheet employed in this system (about 50 μm, as will be discussed in more detail in Section 7.1) and neither of these would be visible to an ordinary observer. It is interesting to note that there is also an intrinsic lateral shift associated with TIR even at a discontinuous interface, the so-called Goos-Hänchen shift[82], which is typically of order 0.5 μm for visible light.

Thus, the qualitative angular dependence anticipated by the density gradient model agrees with the experimental observations of Section 5.5.6. A large range of possible density distributions could be appropriate to describe this behaviour; a few of these are discussed in this section.

6.3.1 Linear density gradient distribution

A linear gradient was the simplest one to consider first. In this case, the volume fraction of particles was a maximum, f_{max}, at the interface and decreased linearly, as the distance d from the interface increased until the particle density reached zero at d_{max}. This is schematically depicted in Figure 6-8.

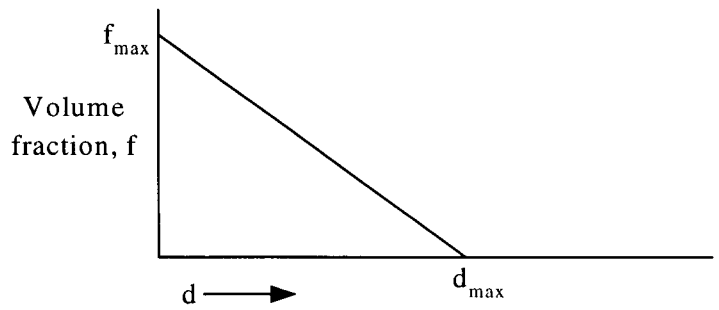

Figure 6-8. Linear density gradient of particles

In order to model the resulting reflectance values under these conditions, the particle volume fraction was calculated, at discrete values of d in 0.05 μm steps throughout the particle layer, using the linear relationship:

$$f = f_{\max} - md \tag{6-2}$$

where f_{max} is the maximum volume fraction and m is the rate of change of the volume fraction. The effective refractive index was then calculated at each position using (6-1). The algorithm employing the differential form of Snell's law, described in Appendix A, was them used to calculate the ray path as a function of incident angle, and the reflectance was predicted. Figure 6-9 compares the predictions of this model to the observed reflectance values. To generate these fits, the maximum volume fraction of the particles and the slope of the gradient were adjusted for each data set, in an attempt to best fit the experimental data.

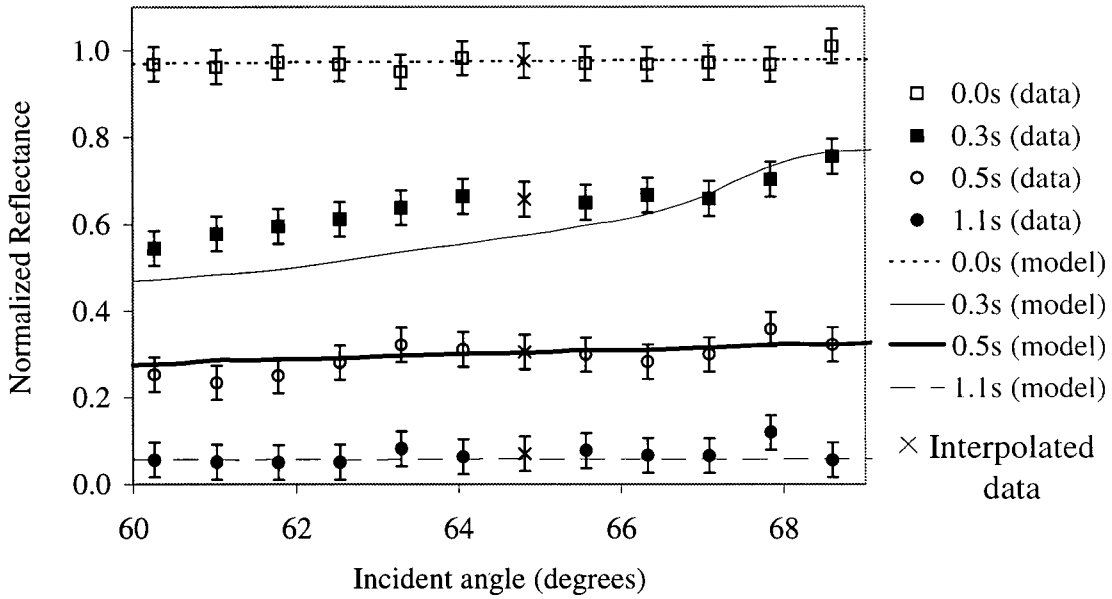

Figure 6-9. Predicted reflectance values using linear density gradient model

This model provides a reasonable prediction of the reflectance in the maximum and minimum states, at t=0 s and t=1.1 s, respectively, but it fails to generate consistent results in the intermediate states. Figure 6-10 shows the distribution used to generate these values.

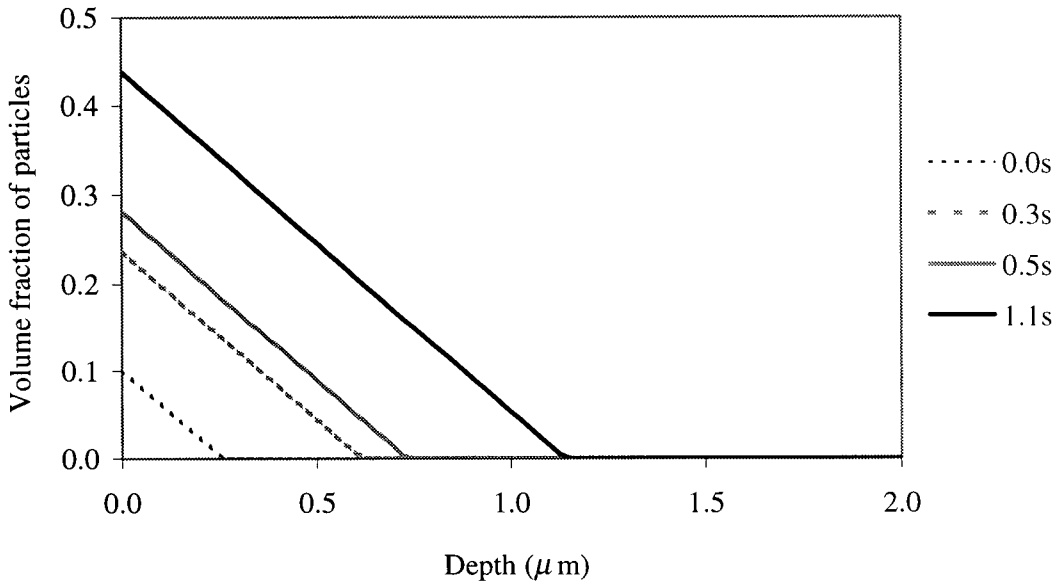

Figure 6-10. Particle distribution predicted by linear density gradient model

Given the inability of this model to predict the angular dependence of the intermediate reflectance values, it is clear that an alternate distribution is required.

6.3.2 Modified linear density gradient

A modified version of the linear density gradient was also considered. This model assumes that there is a maximum possible particle volume fraction for a given particle system, and once this maximum has been reached near the interface, it cannot be exceeded. The resulting distribution, depicted in Figure 6-11, demonstrated a saturation effect where the layer of particles was tightly packed at the interface in a dense layer of thickness d_0.

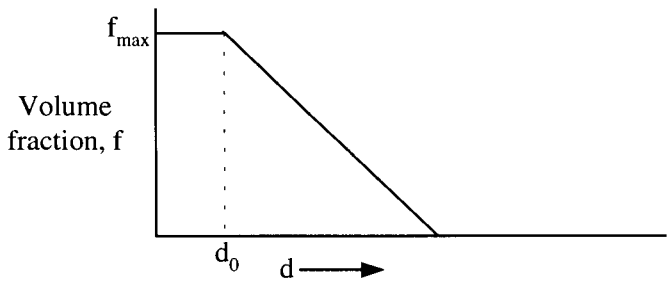

Figure 6-11. Modified linear density gradient of particles

For d values greater than d_0, the particle density decreased linearly, as in the previous model. The volume fraction in this distribution was expressed as:

$$f = \begin{cases} f_{max} & if\ d \le d_0 \\ f_{max} - m(d-t) & if\ d > d_0 \end{cases} \qquad \textbf{(6-3)}$$

Again, the effective index and ray path were calculated using the same procedure as described for the previous model. Figure 6-12 compares the predicted reflectance values, as a function of incident angle, with the same experimental observations as presented before and Figure 6-13 shows the distribution, based on the modified linear model, used to predict the reflectance values.

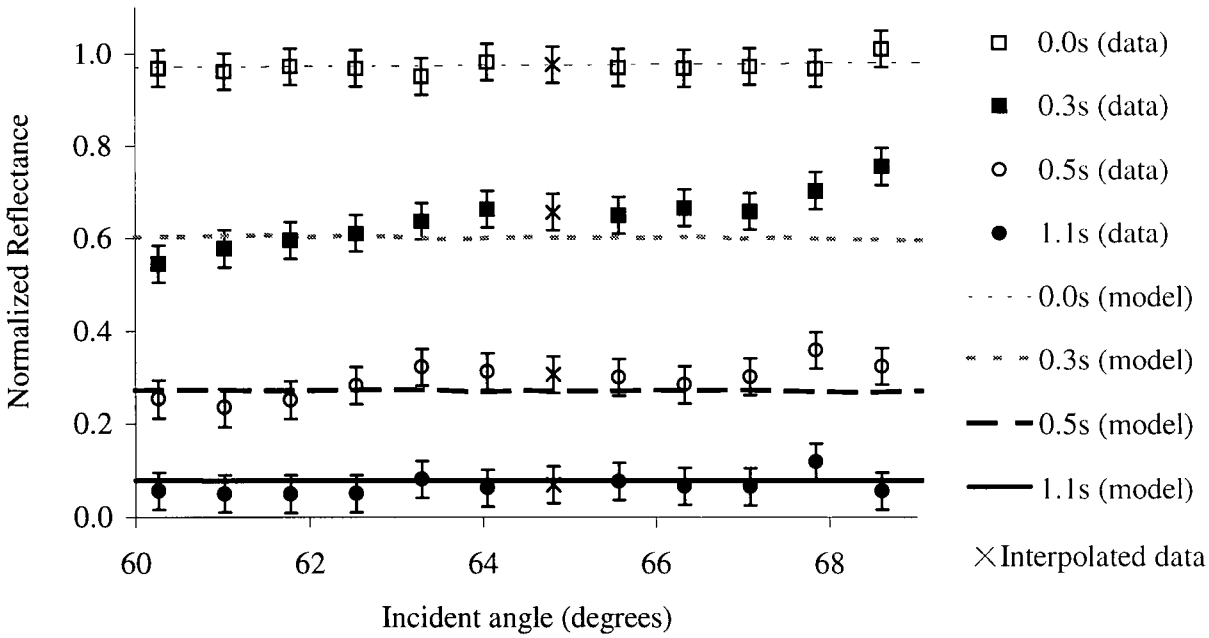

Figure 6-12. Reflectance predicted by modified linear density gradient model

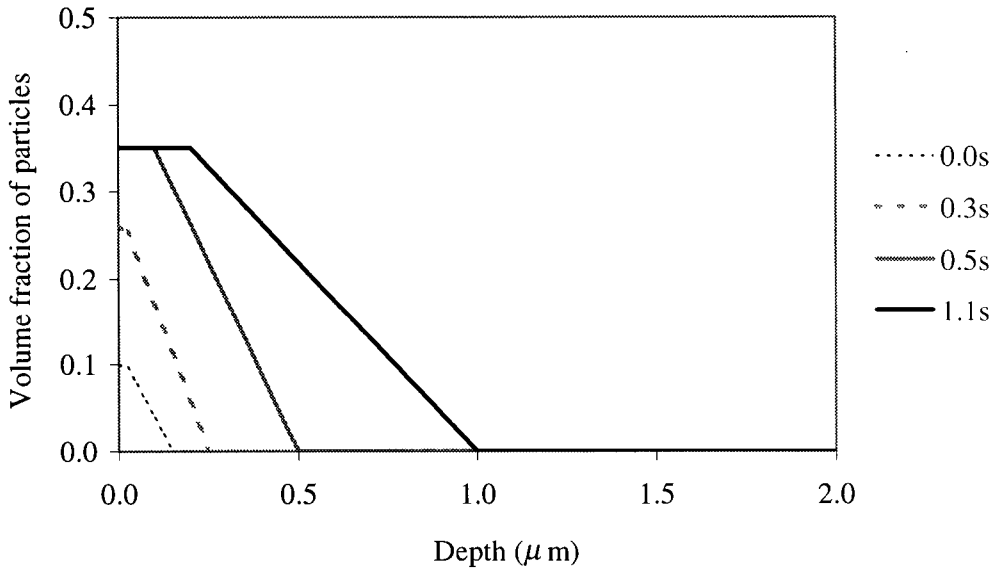

Figure 6-13. Predicted distribution using modified linear density gradient model

Although the particle distribution, in this case, appears more reasonable than the purely linear approach, it is still insufficient to predict the intermediate reflectance values. In the next model, an exponentially tapered distribution was used, which may better represent the true distribution in a physical system.

6.3.3 Exponentially tapered distribution

The fourth possible particle distribution that was investigated incorporates an exponentially tapered function rather than a linear one. In this model, the volume fraction at different locations in the distribution was calculated using:

$$f = f_{\max}\left(\exp\left(\frac{d - V / f_{\max}}{\sigma}\right)+1\right)^{-1} \qquad \textbf{(6-4)}$$

where V is the total volume of particles in the distribution and σ is a parameter, referred to here as the degree of spread, that describes how quickly the distribution changes. (The form of this equation is similar to that of the well-known Fermi-Dirac distribution[83], which describes the typical energy distribution of an ensemble of fermions, which is, of course, a

completely unrelated physical situation.) Several examples of this distribution, having different values of σ, are shown in Figure 6-14.

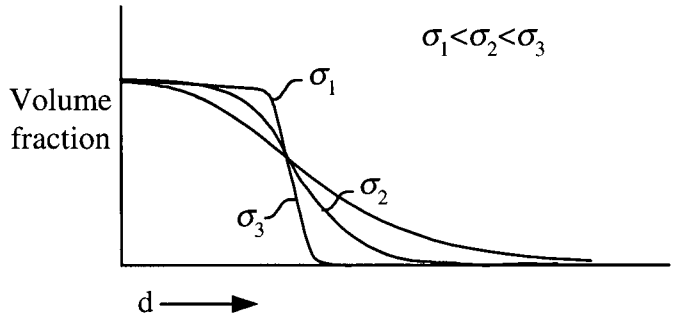

Figure 6-14. Exponentially tapered density gradient of particles

Using the same numerical calculation described in Section 6.2, the absorption corresponding to the path length followed by a light ray was calculated for each angle. The predicted reflectance values are compared to the experimental data in Figure 6-15, and the particle distributions used to generate these fits are shown in Figure 6-16.

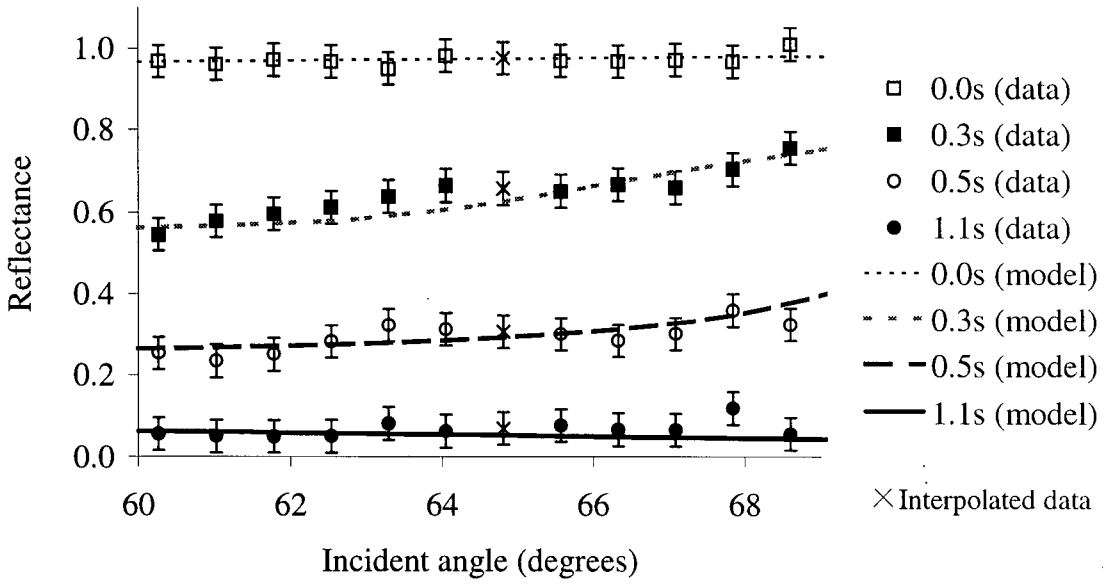

Figure 6-15. Reflectance predicted by exponentially tapered gradient model

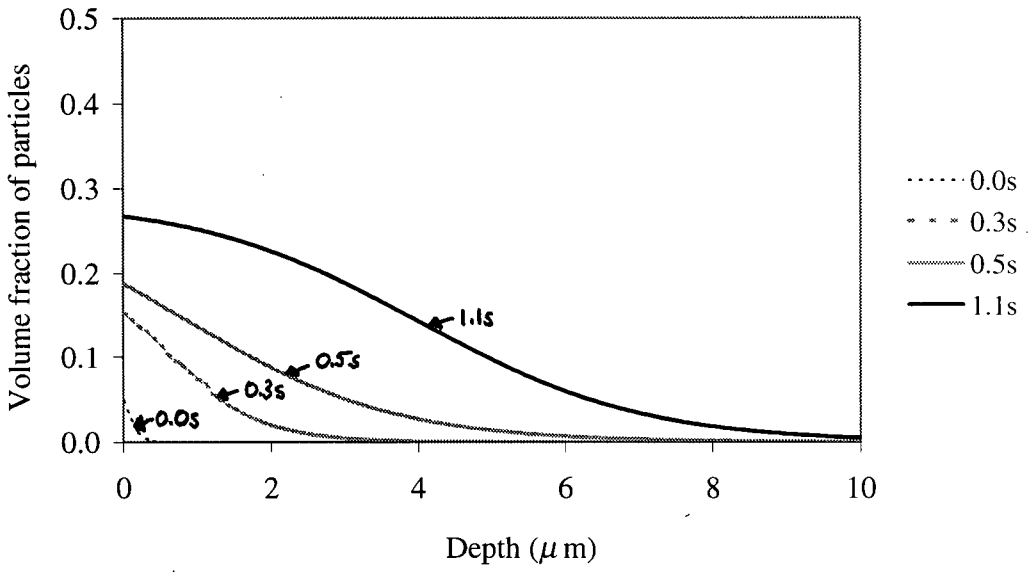

Figure 6-16. Distribution predicted by exponentially tapered gradient model

The predicted reflectance values are in good agreement with the experimental data across all reflectance levels. (Similar curves were plotted and compared well to experimental data for intermediate reflectance levels at intermediate time intervals. For visual clarity, however, only a few such curves are shown in the plot in Figure 6-15.)

This model for the time evolution of the particle distribution appears to be a reasonable one. The maximum volume fraction in the absorptive state at 1.1 s is about 0.28, somewhat less than the value of 0.35 roughly estimated for an assortment of irregularly shaped particles. However, recalling the discussion in Section 5.5.1, the degree of absorption by the pigments depended on the intensity of the applied electric field, and it was postulated that this effect resulted from a layer of micelles at the interface that impeded the motion of the pigments into the evanescent wave region. If this is indeed the case, then the value of the maximum volume fraction generated by the model that resulted in a good fit to the experimental data would depend on the intensity of the electric field applied during the experiment. This value is not the intrinsic maximum volume fraction of the pigment particles themselves, and therefore a slightly lower value than anticipated is perhaps not surprising.

The experimental observations of reflectance as a function of the incident angle of the light have been successfully modeled using an exponentially tapered density distribution of

absorptive pigment particles. This density gradient in the surrounding liquid creates a corresponding gradient of the effective refractive index in this region, thus altering the optical properties near the interface to frustrate TIR. In combination with an arrangement of microstructured optical sheets, such a particle density distribution can be used to modulate TIR for a reflective image device. A number of possible configurations for doing so are investigated in the next chapter.

7 NOVEL OPTICAL CONFIGURATIONS FOR ENHANCING TIR

The previous chapters described many of the issues associated with designing a reflective image device based on the frustration of total internal reflection by pigment particles. As discussed, many undesirable surface energy effects can be overcome using a liquid to prevent direct physical contact between the absorber and the TIR surface. However, this makes the condition for TIR more difficult to ensure. Section 3.6 explained how it is possible to employ TIR at a liquid interface by taking advantage of the three-dimensional refractive index ratio enhancement effect described earlier. This novel technique, devised as a part of this research program, uses a set of layered prismatic sheets to yield a highly reflective surface. This chapter describes the behaviour of the optical system in detail.

The three-dimensional index ratio enhancement effect is apparent if the prismatic sheet, backed by liquid, is viewed at an angle, as depicted earlier as ray A in Figure 2-6, rather than at near perpendicular incidence to the sheet, as depicted as ray B in that figure. In most applications of reflective image devices, such angled viewing is impractical, and it is desirable to have an optical system that allows light at normal incidence to undergo TIR. For this reason, the optical system must include a component that causes TIR for light entering from the normal incidence viewing direction.

As briefly mentioned earlier, a new optical configuration has been devised which makes this practical. The basic idea, shown schematically in Figure 7-1, combines a transmissive light deflecting layer with a light reflecting layer, each layer having a direction of longitudinal symmetry and made from one or more prismatic sheets.[84] The enhanced index ratio effect is caused by stacking the two layers with their symmetry directions oriented perpendicular to one another. As the incoming light rays pass through the deflecting layer, it imparts a component of travel parallel to the symmetry axis of the reflecting sheet to help the rays to undergo TIR. (This is optically equivalent to viewing the reflecting layer at an angle.) The reflecting layer then reflects the light, by TIR, so that it returns toward the deflecting layer. As the reflected rays pass back through the layer, the deflection component of the light ray is cancelled, and it exits the stack traveling exactly opposite to the original incident direction. This recombination is a direct consequence of the reversibility of light rays, where a ray

traveling in one direction through an interface will follow an identical path if it travels through the interface in the reverse direction.

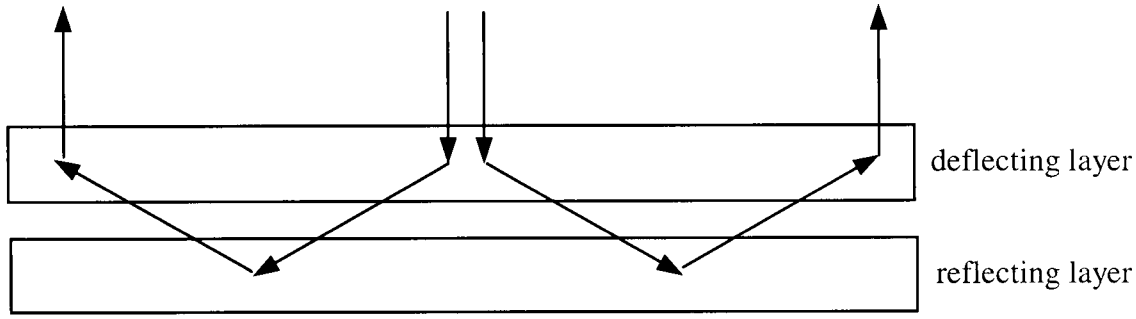

Figure 7-1. Schematic drawing of optical configuration

It is clear, however, from the ray paths shown in Figure 7-1 that using this recombination method, the exiting light rays do not follow the exact path as the entering rays. Rather, the rays return at the same angle, but they are slightly displaced as a result of the deflection. However, since the layers can be made quite thin, this deflection can be limited to less than100 μm, which is an acceptable resolution level for many image device applications.

It should be noted that these prismatic sheets are complex structures, and the behaviour of incident light rays will be strongly dependent on the angle as well as the relative position at which they strike the sheet. In the first sections of this chapter, the characteristics of the optical system are described in terms of the behaviour of one or two sample light rays. This is by no means complete, since a large number of rays under various conditions will be required to fully describe the system. To generate a more complete understanding, Monte Carlo ray tracing, described later in this chapter, was used to simulate the reflectance under realistic illumination conditions.

7.1 Light deflecting layer

The deflecting layer can operate either by refraction or reflection. A linear micro-prismatic sheet, arranged with the prisms facing the viewer, (termed "up" throughout this chapter), as shown in cross-section in Figure 7-2(a), behaves as a refractive light deflector when light from a source shines on it from above. Although this sheet has prismatic structures on the

surface (and therefore many surface normals), these structures are sufficiently small that, macroscopically, the sheet is planar. Thus, a macroscopic surface normal can be meaningfully defined perpendicular to the sheet, as indicated in Figure 7-2.

7.1.1 Refractive mode

In this refractive version of the deflecting layer, a light ray at normal incidence (that is, parallel to the macroscopic surface normal) refracts once when it passes through the prism facet and again when it exits the rear surface of the sheet. Since the illuminated region is typically much larger than the spacing between prisms, an equal amount of light strikes the right-hand and left-hand facets of the prisms. As a result, the incident light is deflected, half of it at a deflection angle $-\alpha$, and the other half at $+\alpha$. This angle depends on the index of refraction, n_1, and the included angle, β, of the prisms.

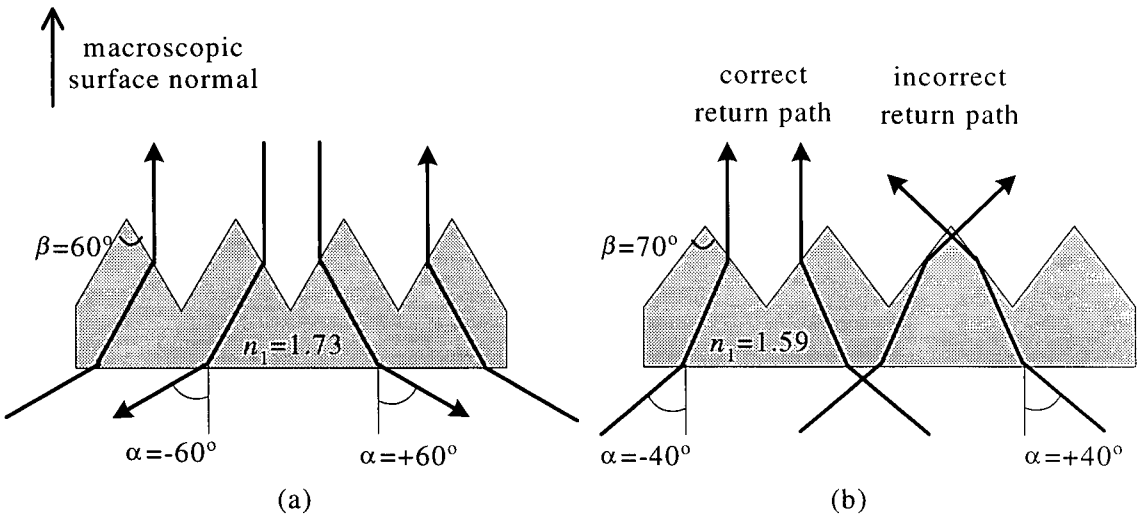

Figure 7-2. Refractive deflecting layer in (a) ideal and (b) non-ideal case

Figure 7-2(a) shows the ideal operation of the refractive deflection sheet. A simple calculation shows that a prismatic sheet fabricated with β=60° and n_1=1.73 will refract light with macroscopic normal incidence such that the refracted ray within the material travels parallel to the opposing prismatic facet, and exits the sheet at α=±60°. This ensures highly efficient recombination of the light rays as they return through the prismatic sheet since the returning light rays also travel parallel to the opposing prismatic facets, ensuring that they all

reach the correct facet to cause refraction into the macroscopic normal direction. (Note that, upon return, the light ray need not intersect the same prismatic facet through which it entered; rather, any facet of the correct orientation will have the same effect. Since the prism sheet is thin, such lateral displacement of the exiting ray is acceptably small.) In this ideal case, all light rays deflected by a left-hand prismatic facet return through a left-hand facet. Similarly, all light rays deflected by a right-hand prismatic facet return through a right-hand facet. As a result, the deflecting layer efficiently deflects and then recombines the light with negligible loss, other than surface partial reflections that can in principle be reduced by anti-reflective coatings.

Currently, optically precise β=60°, n_1=1.73 micro-prisms are not manufactured. However, prismatic sheets with β=70° and n_1=1.59 micro-prisms are available[85], and can be used as the refractive deflecting layer, with some losses. In this case, the refracted ray does not travel exactly parallel to the adjacent prism facet and, as a result, a small but non-negligible fraction of the returning light rays strike the adjacent facet and are not properly recombined. Figure 7-2(b) illustrates this case. The light rays on the left intercept the appropriate prism facet and refract to the original incident angle as desired, whereas the rays on the right intercept the incorrect facet, and so are not properly recombined.

7.1.2 Reflective mode

In the reflective mode, the microstructured surface is oriented with the prisms facing down. Light rays at normal incidence to the flat surface pass without refraction into the prismatic sheet. They then encounter the prismatic facets at a sufficiently large angle for TIR to occur, and the light ray reflects toward the opposing facet, refracting as it exits the sheet. Just as with the refractive case, the incident light beam is split into two beams, as half of the light is deflected at an angle of $-\alpha$ and the other half at $+\alpha$. When these deflected light rays are reflected back towards the prismatic side of the structure, they retrace a similar, reverse path, so that the deflected beams recombine, again with an acceptably small lateral displacement, and exit the sheet.

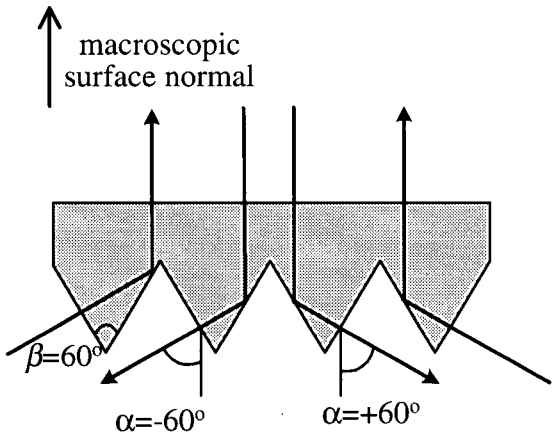

Figure 7-3. Reflective deflecting layer in ideal case

For ideal operation, the sheet should be structured with β=60° micro-prisms, as depicted in Figure 7-3, and the refractive index need only be high enough to cause TIR at the prism facets (polycarbonate material with index n_1=1.59 is suitable, if the backing medium is air, with index n_2=1.0 or perfluorinated hydrocarbon liquid with index n_2=1.276). This ensures that the light ray reflects from the first prism facet at an angle such that it encounters the second facet at normal incidence, and passes through it without refraction, corresponding to a deflection angle α=±60°. Light rays returning to the sheet at this deflection angle encounter the "correct" prism facet; in other words, light rays traveling at a +60° deflection angle encounter only right-hand prism facets, whereas those traveling at a -60° deflection angle encounter only left-hand prism facets. This ensures that the light rays are efficiently recombined. Using β=70°, n_1=1.59 micro-prisms in this reflective mode of the deflecting layer, instead of the β=60° ideal micro-prisms, some losses are incurred because of the partial reflections at the prismatic facets.

The decision to employ the reflective or refractive mode depends on a number of factors, including the desired angular viewing range, as addressed in Section 7.4.

7.2 Light reflecting layer

As mentioned earlier, since the layers in the stack are arranged with their symmetry axes oriented perpendicular to one another, the deflecting layer imparts to the light rays a

component of travel in the direction of symmetry of the reflecting layer. This produces the desired index ratio enhancement effect that allows TIR to occur.

Thus far, the descriptions of a reflective image device presented in earlier chapters have included a prismatic structured TIR surface. However, it is equally appropriate, in optical terms, to make use of a flat TIR surface. The only requirement for the operating principle described here is that the reflecting layer must have at least one direction of translational symmetry, so that the index enhancement effect can be employed. For the linear prismatic structures discussed here, it is clear that one symmetry axis exists. A planar surface also has a direction of symmetry; in fact, it has an infinite number of such directions, and therefore is a possible reflective layer. TIR will occur on the flat surface, provided the angle resulting from interaction of the light with the deflecting layer is sufficiently high to suitably enhance the index ratio at this surface.

There are different advantages to both prismatic and planar TIR surfaces. In terms of the degree of absorption, prismatic surfaces are more effective because each light ray entering the device undergoes two reflections by TIR and, as such, the absorption level is greatly increased. For instance, if the reflectance, in the absorptive state, following one reflection is 10% (i.e. 90% of the light is absorbed), then following the reflection at the second interface, the reflectance will be only 1%.

Despite the enhanced degree of absorption, a prismatic surface is unsuitable in some device configurations. For instance, a number of materials were discussed in Section 3.5 as possible absorbers in a reflective image device based on TIR. As discussed, both conformable, porous elastomers and thin, flexible membranes would be more appropriate for frustrating TIR at a flat interface rather than a structured one. In this configuration, these absorbers would be easier to fabricate and more tolerant of minor variations in surface flatness and the presence of dust particles. The situation is much the opposite for systems using electrophoretic pigment particles to frustrate TIR, in which case it is desirable to enclose the particle suspension in small volumes to prevent pigment clustering problems, as detailed in Section 3.11. In this case, the prismatic geometry is advantageous as it provides a convenient method of encapsulating these small volumes into the linear prismatic channels formed when the prism tips are held in close proximity to the rear substrate. Although the resultant applied

electric fields are non-uniform, and could cause some particle deposition non-uniformity, this is not a big problem as such variations would be invisibly small in the tiny cavities. Experimental results suggest that this behaviour does not limit the apparent degree of absorption across the device surface and ensures long-term stability of the device.

7.3 Layered sheet configurations

There are many possible configurations incorporating the light deflecting and light reflecting layers, combining sheets with different refractive index values, prism structures, and orientations. Each configuration has advantages and disadvantages, in terms of both the optical and practical operation of the device. For instance, there are a number of configurations requiring the refractive mode of the deflecting layer, where the outer surface of the device is microstructured. However, in some applications, these outward-facing prisms may be susceptible to dust collection or damage, so in these cases the reflective mode of the deflecting layer, with the flat outward surface, may be preferred. The orientation of the reflective layer offers similar advantages and disadvantages, as discussed in the previous section. For some absorption mechanisms, having a flat TIR surface is an advantage for mechanical reasons. However, the micro-prismatic TIR surface allows two sequential reflections, therefore a greatly enhanced absorption effect, which may be of interest in applications where the lowest possible reflectance level in the black state is desired.

A few of these configurations, as well as an indication of their relative advantages and disadvantages, will be addressed in detail in this section.

7.3.1 β=90° micro-prism geometry

One simple case, first introduced in Section 3.1 and shown again in Figure 7-4(a), uses a micro-prismatic sheet with β=90°, n_1=1.59 prisms, where the prisms are in contact with a liquid of n_2=1.276. The index ratio, n_1/n_2, for this interface is 1.25, corresponding to a critical angle, θ_c, of 53.0°, so a light ray at perpendicular incidence, striking the prismatic facets at 45°, will not undergo TIR; rather, it will pass through the sheet. However, if the light ray is instead incident on the prismatic facets at a deflection angle of α=32. 5°, the

enhanced index ratio effect from Section 2.2.2 will ensure TIR. Referring to (2-16), κ has a value of approximately 0.843, leading to an effective index ratio of 1.42, and a corresponding effective critical angle of 45°. Thus, light incident on the prismatic facets at an angle α >32.5° will exceed the effective critical angle at the interface and undergo TIR. (Taking into account the refraction at the flat surface of the prismatic sheet, this internal deflection angle α>32.5° in the material corresponds to an external deflection angle, outside the material, of γ>58.7°. While α and γ were calculated here for the purpose of explanation, it is important to remember that the use of κ as a constant value of the system eliminates the need to calculate the resultant angle as the ray passes through the various materials in the system.)

Light rays incident on the structure at this angle are reflected by TIR at each prismatic facet and exit the sheet, as in Figure 7-4(a). The reflection modulates, when frustrated by an typical absorbing material, from a high reflectance value of close to 100% to a low value of easily less than 10%. This results in an acceptable contrast ratio of 10:1, and a very effective optical switch.

However, there is a complication resulting from the Fresnel, or partial, reflections at the top surface. At any interface between two optically dissimilar materials, there will be a partial reflection, the degree of which is determined by a set of equations known as the Fresnel relations. These relations are described in more detail in Appendix K. Primarily, the degree of reflection increases with both the index ratio and the incident angle. In this system, at normal incidence, the partial reflection on the flat surface of the prismatic film will be about 5%, but at the required external deflection angle of 58.7°, the partial reflection is greater than 20%. As shown in Figure 7-4(b), the partial reflection follows the same angular path as the TIR ray, and therefore similarly reaches the detector (or viewer).

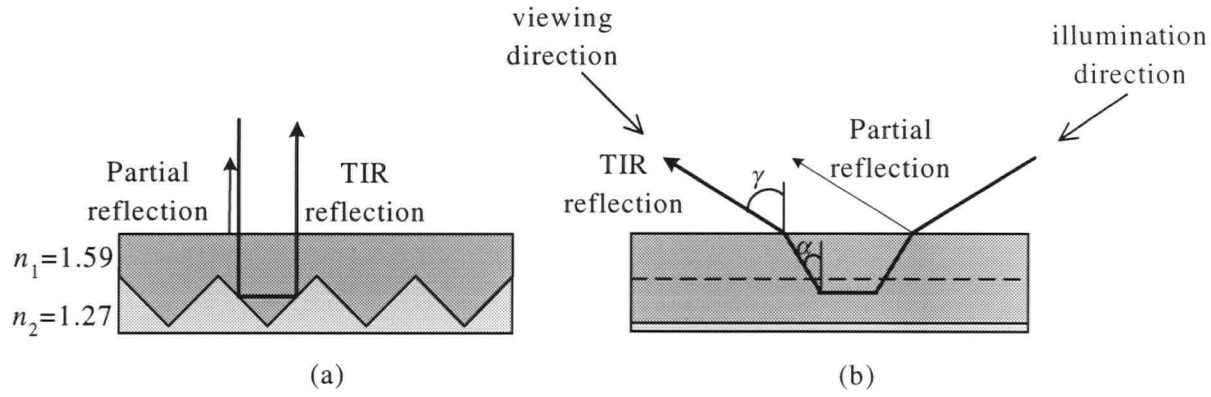

Figure 7-4. Ray path through β=90° micro-prism sheet

The partial reflection is not affected at all by the motion of the absorber and therefore cannot be modulated. So, while the maximum reflectance measured at this angle remains at 100%, the minimum reflectance increases to 30%, and the contrast ratio similarly decreases to about 3:1. Clearly this partial reflection causes an undesirable effect, although it could be at least partially ameliorated through the use of anti-reflection coatings. Such coatings are widely used in optical applications where the glare reduction is important. However, these coatings are often multi-layered, and can be expensive to apply, so an alternate approach to eliminate partial reflection was investigated in the course of this study. As described in the following section, the partial reflection can also be reduced by the addition of a second β=90° micro-prism sheet.

7.3.2 Layered 90°/90° micro-prism geometry

An alternate method to anti-reflection coatings for reducing partial reflections, perhaps more appropriate in this micro-prismatic device, uses a second sheet with β=90° micro-prisms. This sheet is optically bonded to the flat side of the first sheet with the prisms facing up, as in Figure 7-5, but with the longitudinal symmetry direction perpendicular to the first.

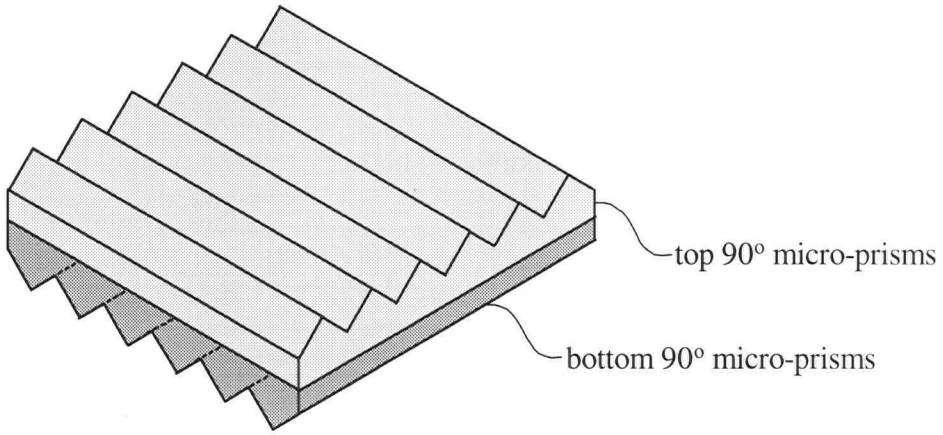

Figure 7-5. Layered structure of 90°/90° micro-prism sheets

When this structure is viewed at α=45°, the incident light rays are approximately perpendicular to the top prism facets, and the rays pass undeflected into the second sheet, so that they undergo TIR at the bottom prismatic surface, as shown in Figure 7-6(a). The partial reflection is reduced to approximately 5% at each interface and, although this small fraction of light is lost, it does not travel toward the viewer, as shown in Figure 7-6(b). The result is that although the maximum reflectance is slightly reduced, the minimum reflectance remains less than 10% and the contrast ratio is high.

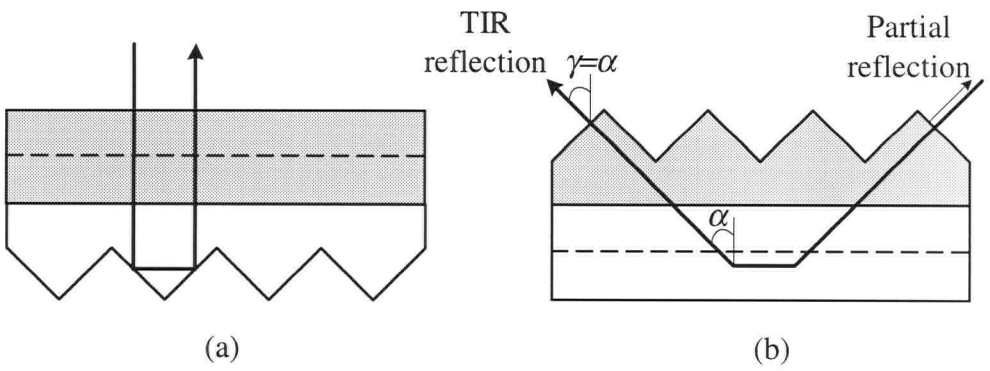

Figure 7-6. Light ray incident on layered 90°/90° micro-prism structure

A second, and important, function of the additional micro-prismatic sheet is that it prevents refraction of the incoming light ray, so that a smaller external value of γ will suffice. This is

so because the light ray enters the facets of the top sheet at nearly perpendicular incidence, and since the two sheets are laminated together using an index-matching adhesive, no further refraction occurs. As a result, the internal deflection angle, α, is the same as the external deflection angle, γ. In many of the prismatic sheet configurations appropriate for a reflective image device based on total internal reflection, this "preservation" of the deflected angle is crucial in order to ensure that TIR occurs over a sufficiently large range of angles.

The 90°/90° layered micro-prism geometry is of particular interest in this study. Not only does this configuration allow the slight partial reflections to be excluded from the field of view, but high quality, precise 90° microstructured films are readily available from commercial sources, so this system can be easily constructed to yield the desired high reflectance. As a result, although there are many possible optical configurations, the 90°/90° layered component of the system is ideal for further study in this thesis.

A 60° deflecting sheet can be placed above the 90°/90° micro-prism geometry to deflect incoming rays to a suitable angle. In this case, the rear 90° sheet is considered as the light-reflecting layer, and the top 90° sheet is considered to be part of the light-deflecting layer. The following section describes the operation of this layered system.

7.3.3 Layered 60°/90°/90° micro-prism geometry

The addition of a top micro-prism sheet to deflect the light, as described in Section 7.1, allows viewing at normal incidence. This deflecting layer is oriented in refractive mode, with the micro-prisms facing up and the flat surface facing the 90°/90° micro-prism structure. This arrangement is shown in Figure 7-7.

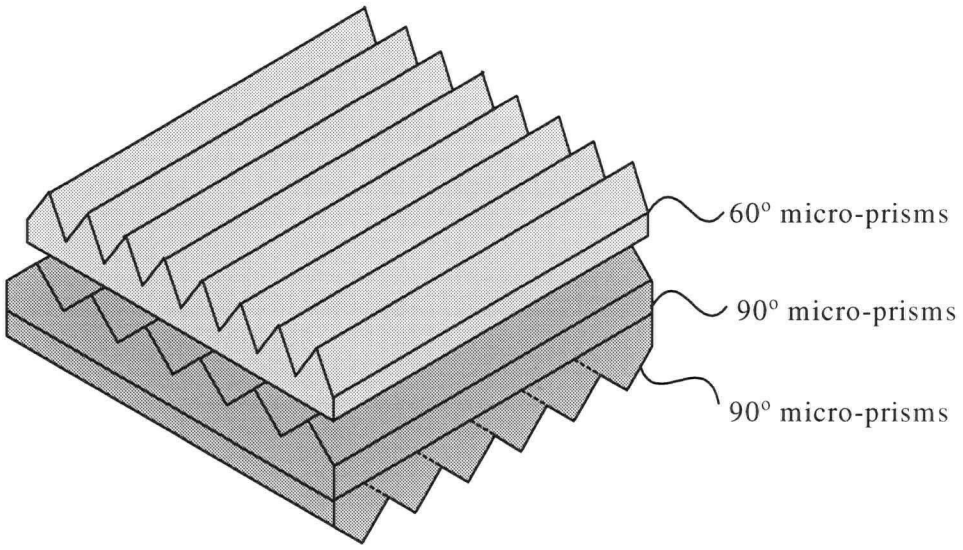

Figure 7-7. Arrangement of 60° and 90° micro-prism sheets

In the ideal operation of this deflecting layer, requiring an included prism angle β=60° and a refractive index value n_1=1.73, the light deflects parallel to the opposing prismatic facet, and does not interfere upon recombination. With an air gap between the top 60° micro-prism sheet and the 90°/90° structure, this results in an external deflection angle, γ=60°. However, this is much greater than the 45° deflection angle required for ideal operation of the 90°/90° structure, as described in Section 7.3.2. To reduce this deflection angle, the region between the sheets is filled with a material of refractive index value intermediate between that of air and polycarbonate, for example, perfluorinated hydrocarbon liquid of index value 1.276. The resulting external deflection angle, γ, as the light ray passes from the deflecting sheet into the fluid layer, is about 43°, and therefore it refracts very little as it enters the top 90° prismatic facets. Thus, a light ray at normal incidence deflects to within the desired angular range, and interacts with the 90°/90° micro-prism structure as described in Section 7.3.2. This ray path is depicted in Figure 7-8.

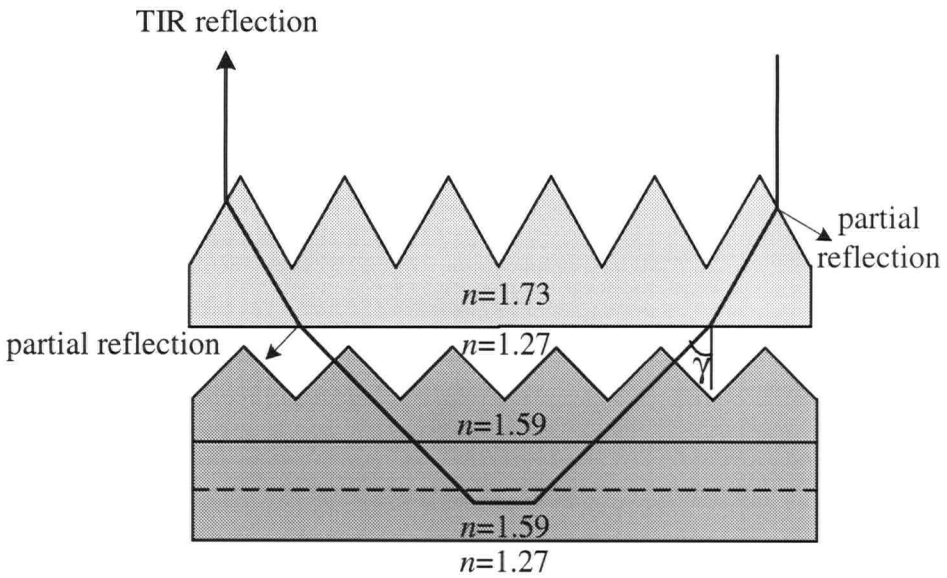

Figure 7-8. Ray path through 60°/90°/90° structure

The addition of the 60° sheet introduces further losses as a result of partial reflections, as shown in the ray diagram in Figure 7-8. These reflections occur both on the micro-prism facets as the ray passes into the optical structure, and on the flat surface as it travels out. The top surface reflection is substantial, about 25%, since the both the refractive index mismatch and the incident angle are large. The partial reflection at the flat surface is about 6%, since it is reduced by the addition of the intermediate index material between the layers, but it is still large enough to affect the contrast ratio. As a result, a practical reflective image device using this optical configuration would require anti-reflective coatings on these two surfaces to minimize the losses.

This is one of many possible optical configurations employing a reflective layer with a prismatic TIR surface. The following section describes the operation of a similar layered arrangement, but having a planar TIR surface, and using only two microstructure sheets, rather than three. This alternate type of geometry may have some practical advantages, as described earlier in Section 7.2.

7.3.4 Interleaved 60°/60° micro-prism geometry

There are a number of optical arrangements that can be used to modulate TIR in a reflective image device, by using a planar TIR surface rather than a structured one. The configuration shown in Figure 7-9 is one of these arrangements. In this configuration, a β=60° micro-prism sheet, with its prisms facing down, is positioned over a second β=60° sheet, with its prisms facing up and meshed, or interleaved, with the prisms on the top sheet.

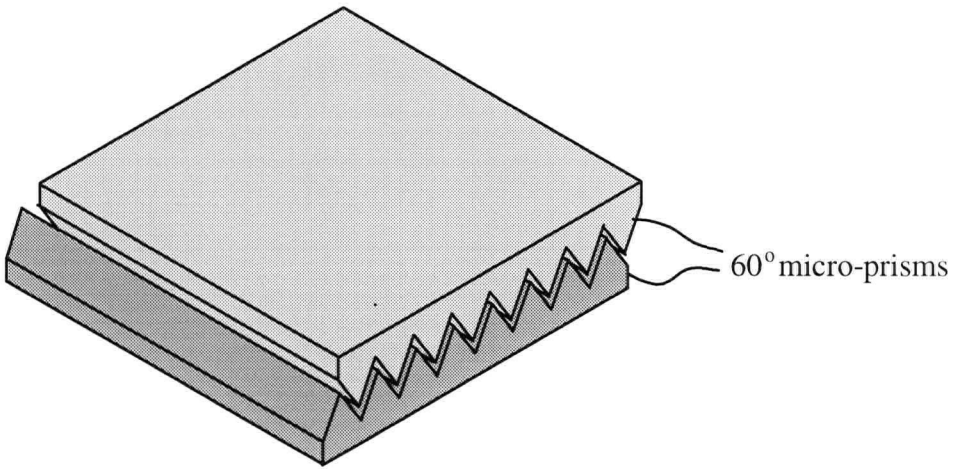

Figure 7-9. Interleaved structure of 60° micro-prism sheets

The effective index of this system is enhanced by positioning the light-deflecting and light-reflecting portions so that they have mutually perpendicular symmetry directions. In the previous two structures, these symmetry directions were easy to discern since both portions contained micro-prismatic surfaces. In this arrangement, this perpendicularity is somewhat subtle, since the two prismatic surfaces have parallel symmetry directions. However, the micro-prisms in this system comprise the light-deflecting portion and the planar rear surface comprises the light-reflecting portion. Therefore, as described earlier in Section 7.2, the planar surface has a direction of symmetry perpendicular to that of the micro-prisms, and the effective index enhancement can be employed.

The top sheet is used in reflective mode to deflect the normally incident light rays by ±60°, as depicted by the ray path in Figure 7-10(a), and the deflected light ray passes essentially without refraction through the opposing facet of the 60° micro-prism to enter the air gap

between the two sheets. The light ray encounters the prismatic facet of the second sheet and enters the material, again essentially without refraction. The ray then travels parallel to the opposite prismatic facet and strikes the planar surface at a sufficiently large angle that it exceeds the critical angle for TIR at this interface. The light ray reflects from the rear surface and follows a similar path as it exits the structure, as shown by the cross-sectional view in Figure 7-10(a).

Figure 7-10(b) demonstrates a number of partial reflections along the light path at other than normal incidence, which reduces the overall contrast between the maximum and minimum reflectance states. However, anti-reflection coating on the prismatic surfaces can be employed to reduce the effect of these undesirable reflections.

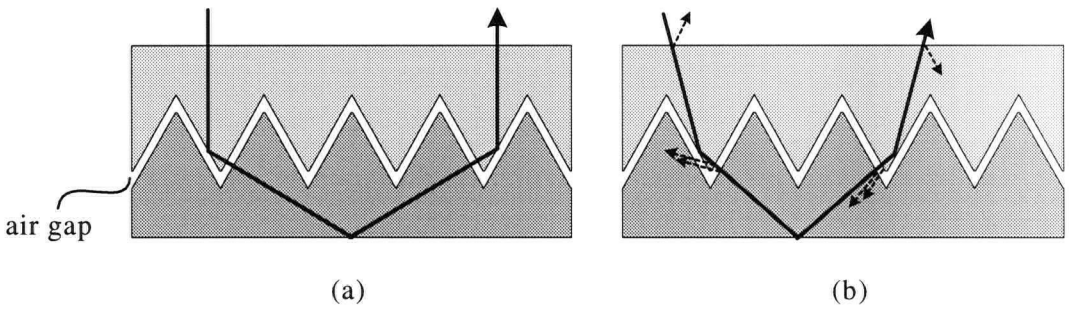

Figure 7-10. Ray path through layered structure of 60° micro-prism sheets

As discussed in Section 7.2, the flat TIR interface offers some advantages in terms of the choice of absorbers and the uniformity of the applied electric field, so it is useful to consider this geometry.

The basic operation of a few optical geometries has been illustrated in this section, based on a few sample light rays. However, for each incident angle, there are many possible ray paths that the light ray could follow, depending on the relative location at which it strikes the assembly, with respect to the prism structures. Some of these ray paths are considered favourable, since they result in TIR at the appropriate interface, whereas others can result in the light ray reflecting prematurely or not reflecting at all. As the incident angle changes, the fraction of favourable ray paths can either increase or decrease, depending on the structure parameters. These changes are difficult to predict because of the complexity of the structure,

so a more complete understanding of the system behaviour requires computer modeling of a large number of incident rays, as discussed in the next section.

7.4 Modeling the system using Monte Carlo ray tracing

In the most obvious approach to computer ray tracing, one could calculate the resulting distribution of the light following a refraction or reflection from a surface, then follow that distribution as it propagates toward the next surface, and so on. In this case, the computational size would grow exponentially, quickly surpassing the capabilities of any available computer. This problem is often encountered in fields of study where the processes involved can only be described by statistics. To compute random processes, a well-known technique known as the Monte Carlo approach is often employed, in which probabilistic selection techniques are used to keep the computation manageable, at the expense of introducing random statistical error of known size.

Throughout the course of the research involved in this thesis, the Monte Carlo approach was applied, using a commercial software package[86], to trace the propagation of a random selection of rays through various arrangements of optical films. Here, reflection and refraction are treated as random processes, and the continuous distribution of light is represented by discrete rays. The refracted and reflected rays are randomly selected, based on the known reflectance values. By ensuring a sufficiently large set of sample rays, the resulting light distribution can be determined with great confidence. This approach was applied to the optical geometries described in Section 7.3.

7.4.1 Model set-up

In these models, the reflectance of the structure was predicted, as a function of the angle of the light source incident on the surface. It was not necessary to quantify the reflectance for all source angles and viewing directions, as described in the discussion on the bi-directional reflectance distribution function in Section 2.2.3, but it was useful to predict, for a few sample configurations, the reflectance over a range of viewing angles.

Since the reflectance of the surface depends on the orientation of the sheet assembly, it will be helpful throughout the rest of this discussion to define a consistent orientation of the assembly in a Cartesian coordinate system. Specifically, the light-deflecting portion is oriented with the linear prisms running horizontally, defining the x-axis, and the light-reflecting portion is oriented with the prisms running vertically, defining the y-axis. It follows, then, that the z-axis is defined by macroscopic surface normal of the sheets. In the models that follow, the sheet assembly remains fixed in position while the angle of the light source is changed.

Figure 7-11 depicts the two angles used to define the source orientation. Figure 7-11(a), shows a top view of the assembly while the light source rotates in the x-z, or horizontal, plane through an angle α_x. Similarly in Figure 7-11(b), the assembly is viewed from the side and the light source is rotated in the y-z, or vertical, plane through an angle α_y. This angular rotation of the source allows evaluation of the surface reflectance over a range of angles.

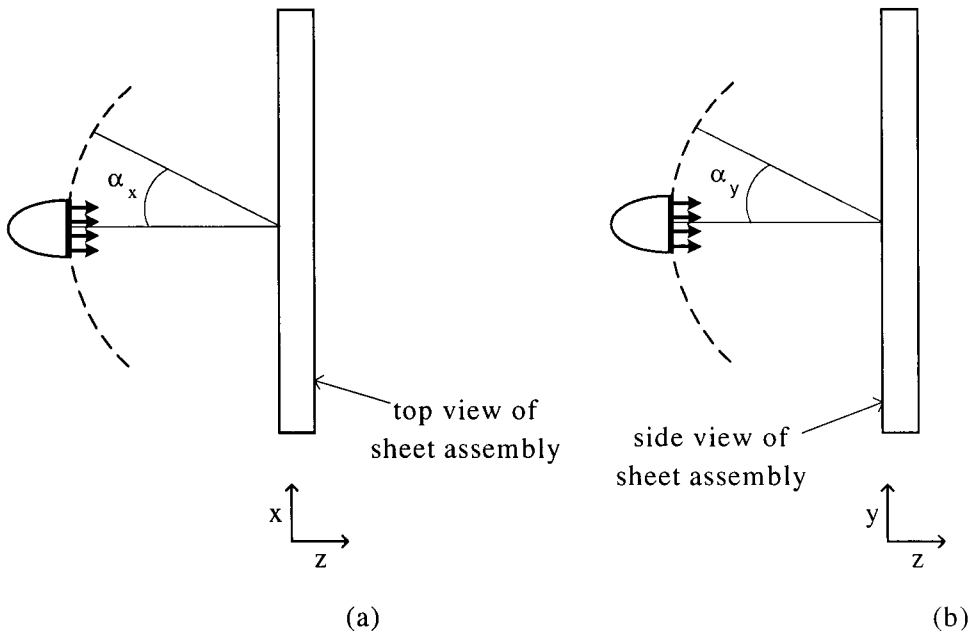

Figure 7-11. Different angular positions of light source

Using the commercial software package, TracePro®, the reflectance of various complicated structures was predicted. These micro-prismatic sheets were drawn using AutoCAD®[87], a three-dimensional computer-aided design program, and then imported into the ray tracing

software, where they were assigned specific optical properties, from a library in the software program, to represent the desired materials.

To model the high reflectance state of the system, the region immediately adjacent to the rear surface was assigned a refractive index value of 1.276, equal to that of perfluorinated hydrocarbon liquid. The low reflectance state was modeled by giving this material an additional imaginary refractive index component sufficiently large to absorb, to the appropriate extent, the light incident on this surface. A typical optical structure, imported into TracePro®, is shown in Appendix L.

In many of the models studied here, the light directed onto the surface was modeled as a highly collimated (less than 1° collimation angle) diffuse, white source. Typically, a set of 5000 random rays was used to generate the predicted reflectance values. During the ray trace analysis, the intensity and position of each ray was calculated as it interacted with the refractive and reflective elements of the structure. The program stores the results in a data file, and the results are then presented in a number of forms depending on the particular analysis. Appendix M shows a sample of typical TracePro® output. As well, a sample of these ray paths can be plotted on the structure, as a visual analysis aid. An example of such a ray diagram is also shown in Appendix M.

7.4.2 Model results

In the analyses discussed in the following section, the reflectance was calculated as the fraction of incident rays striking the large target plane (representing the viewer), as the source was moved through a range of incident angles. Actually, this arrangement is really the converse of the real situation, in that the viewer is normally at one specific location, observing a reflectance from a source that is typically very broad. That arrangement is computationally more difficult in TracePro®, and fortunately is optically equivalent to the "small source-large detector" approach described here, due to the reversibility of light rays.

A large number of different optical structures, with various orientations, prism angles, and material properties, were modeled throughout the course of this study, and a few sample models are discussed in this section. In particular, the predicted reflectance values for the

arrangements described in Section 7.3 are shown. It should be noted that these models represent ideal cases, and demonstrate the potential reflectance achieved using the mutually perpendicular micro-prism geometry approach. Unfortunately, at the current time, these structures cannot be constructed for experimental purposes, as high-quality β=60° micro-prisms are unavailable. As well, these models include high-quality anti-reflective coatings on some surfaces to eliminate partial reflections but, currently, anti-reflective coatings are not yet available on microstructured polymer sheets. (In Section 7.5, an experimental sample was constructed using available, albeit imperfect, micro-prism sheets, and the measured reflectance values substantially agreed with those predicted by the TracePro® model of the structure.) However, despite the fact that the structures modelled in this section cannot be realized at the present time, it is worthwhile to examine the reflectance behaviour to demonstrate the potential of this technique and, hopefully, to support the decision to manufacture these more advanced structures.

7.4.2.1 Layered 90°/90° micro-prism geometry

As discussed earlier in Section 7.3.2, the 90°/90° layered micro-prism geometry shown in Figure 7-5 is an ideal structure since partial reflections from the various surfaces do not interfere with the reflections caused by TIR, and the system can be experimentally constructed using high-quality, commercially available sheets. These two factors made this a useful system to model using TracePro®.

In this model, two prismatic sheets, with included angle β=90°, were assigned a refractive index value of 1.59, and positioned with the flat surfaces in direct contact, and orthogonal directions of symmetry. A large target plane was positioned at α_y=45° to the macroscopic surface normal of the sheets, so that it was parallel to the left-hand facets of the top prisms, as shown in Figure 7-12(a). Maintaining this angle in the vertical plane, the source was then rotated in the horizontal plane, as depicted in Figure 7-12(b), and the reflectance as a function of α_x was calculated as the fraction of incident rays reaching the plane. For each source angle, the maximum reflectance state was modeled by assigning to the region in contact with the rear prisms the properties of a clear perfluorinated hydrocarbon liquid, and the minimum reflectance was modeled by making this rear region absorptive.

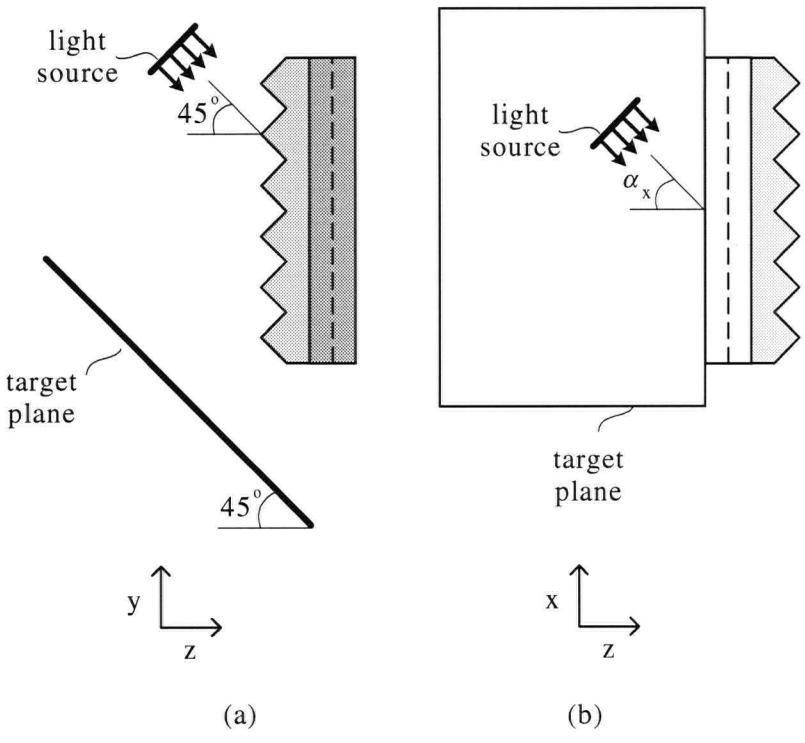

Figure 7-12. Position of light source and target plane for 90°/90° system model

These predicted reflectance values are shown in Figure 7-13. It is not surprising that the maximum reflectance of almost 100% occurs when α_x=0°, since the light rays in this case follow the ideal ray path, as described in Section 7.3.2, with essentially no refraction by the top prisms.

It is important to keep in mind that although the reflectance value represents the total number of light rays that reached the target plane, it does not necessarily mean that all of these rays have followed the desired ray path and undergone TIR. However, if a ray has undergone TIR at the rear prismatic interface, then by adding an imaginary component to the refractive index of the liquid region in contact with this interface, this ray can be absorbed. If, by changing only the imaginary component of the refractive index in this region, a light ray which initially intercepted the target path no longer does so, then it must be true that, in the reflective state, this light ray had undergone TIR at the appropriate interface and, in the absorptive state, it was absorbed at the interface. In this case, the predicted reflectance of the absorptive state is only about 2%, indicating that almost all of the light rays striking the target plane had followed the desired TIR path through the device.

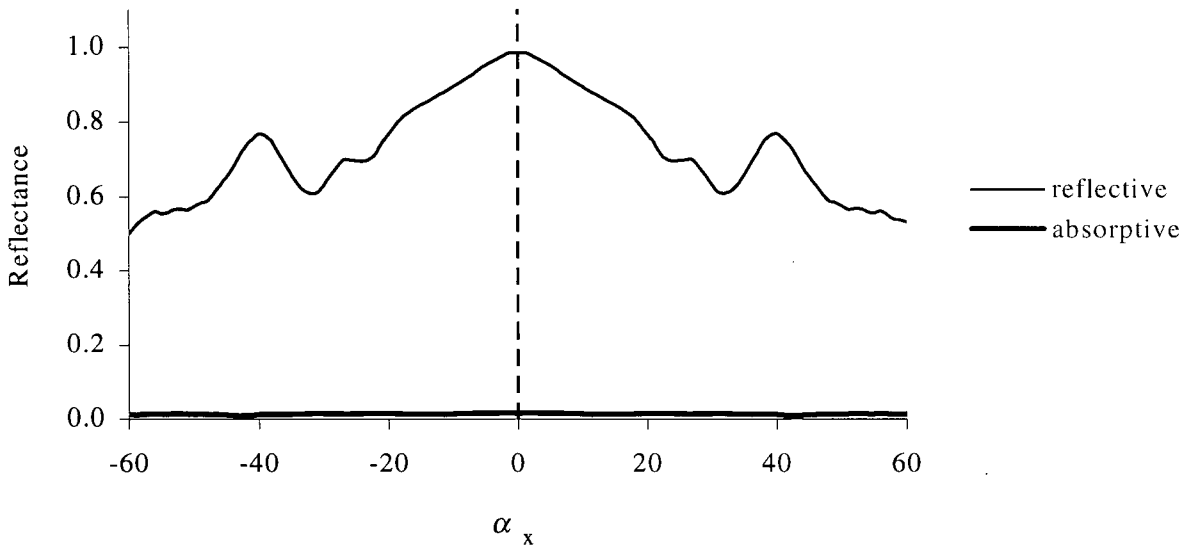

Figure 7-13. Reflectance versus vertical source angle for 90°/90° system

The reflectance remains acceptably high (that is, greater than 70%) over the range of angles α_x between -40° and 40°, and by $\alpha_x = \pm 60°$, the maximum reflectance is less than 50% since the incident light rays at these angles tend not to follow the preferred ray path. As well as this overall decreasing reflectance behaviour, there were a number of local minimum and maximum values of the reflectance within this range, as a result of the interaction with the prism structures. While possible in principle, it would be a lengthy and tedious process to predict the various ray paths responsible for these changes in reflectance. Rather than a detailed investigation of the angular reflectance variation, it is sufficient for this purpose to recognize that the structure behaves as expected.

7.4.2.2 Layered 60°/90°/90° micro-prism geometry

In this model, a micro-prismatic sheet with included angle β=60° was assigned a refractive index value of 1.59 and positioned, with the linear prisms running in the horizontal direction, directly in front of the 90°/90° assembly. The region between the layers was assigned a refractive index value of 1.276, and a large target plane was positioned perpendicular to the

macroscopic surface normal of the sheets. Top and side cross-sectional views of this model configuration are shown in Figure 7-14.

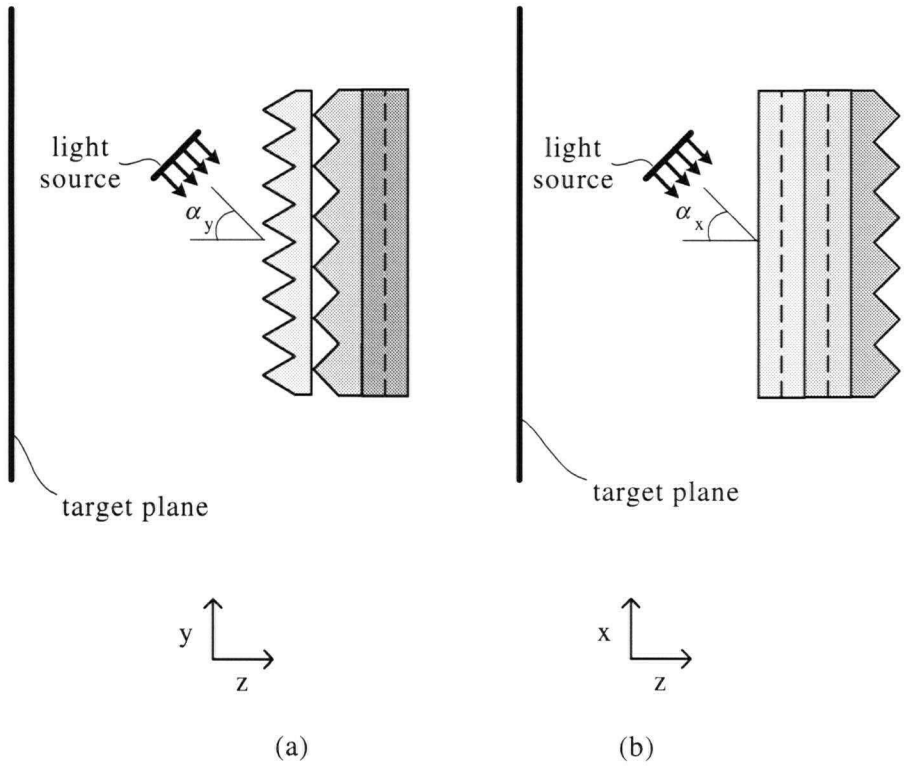

Figure 7-14. Light source and target plane position for 70°/90°/90° system model

The predicted reflectance of the surface as a function of the source angle, α_y, with α_y=0°, is shown in Figure 7-15. In the reflective state, at normal incidence or α_y=0°, the reflectance was predicted to be 80%, (meaning that when the light source was positioned at α_y=0° and α_x=0°, 80% of the incident light rays intercepted the target plane). In the absorptive state, however, the reflectance at normal incidence is predicted to be less than 5%, indicating that most of the initially reflected light rays were absorbed.

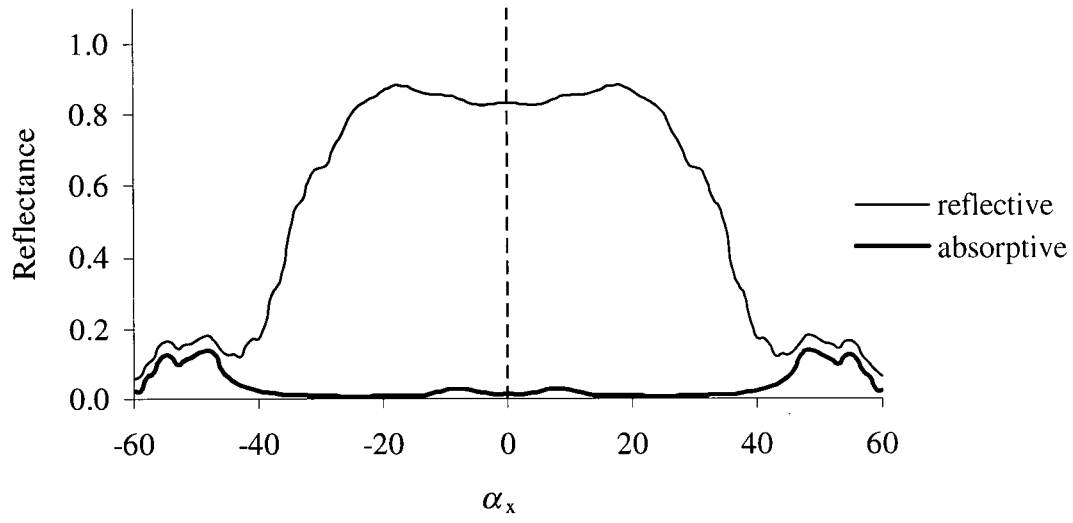

Figure 7-15. Reflectance in vertical plane for 60°/90°/90° system

The reflectance remains at about 80% for the reflective state and 5% for the absorptive as α_y increases to greater than α_y=±25°. For angles outside this range, the maximum reflectance rapidly dropped, because refraction by the various layers causes many of the light rays to strike the TIR interface at angles less than the critical angle, so TIR does not occur, and these light rays do not return to the target plane. In terms of a reflective image device incorporating this structure, 80% reflectance in the range from α_y =-25° to +25° means that a high contrast, bright image will be visible over a fairly wide range of angles, from 25° above to 25° below normal incidence.

The reflectance as a function of α_x (with α_y=0°) was also predicted by the model. These results, shown plotted in Figure 7-16, indicate that, at α_x=0° and α_y=0°, the maximum reflectance was predicted to be 80%, consistent with the measurement obtained at the same angular position for the angular variations of α_y. In this plane, however, the reflectance decreases dramatically as the angle is increased, so that by α_x=±15°, the reflectance is only about 45%. The reflectance then increased as a function of angle until about α_x=±30°, where the reflectance again increased to about 90%.

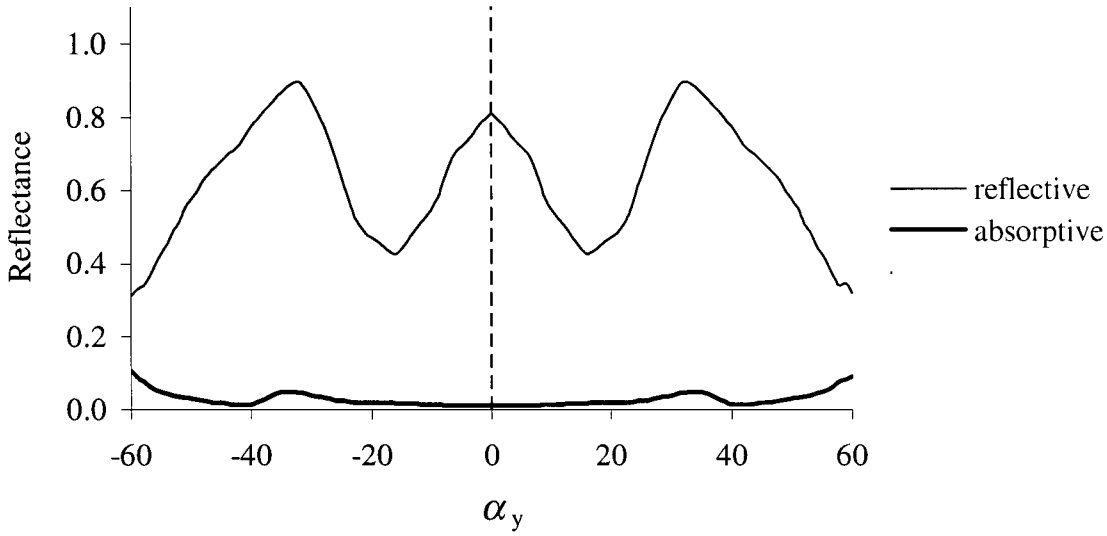

Figure 7-16. Reflectance in horizontal plane for 60°/90°/90° system

Clearly, the angular response predicted for this layered structure is not ideal for a reflective image device, since the dramatic decrease in reflectance at $\alpha_x=\pm 15°$ implies that the viewer would observe a very noticeable decrease in image contrast when viewing the surface somewhat to the left or right of normal incidence. Potentially, this appearance could be reduced with the addition of a small degree of angular scatter to the system to blur out these fine features.

7.4.2.3 Layered 60°/60° micro-prism geometry

This interleaved structure exhibits useful properties in a number of ways, so it is worthwhile to model its reflectance behaviour. To do so, two micro-prismatic sheets, with $\beta=60°$, were positioned with the prismatic surfaces facing each other, and interleaved to form a 20 μm air gap. The prismatic surfaces were assigned the properties of an anti-reflection coating, so that partial reflections at these surfaces were essentially eliminated. As usual, the region in contact with the TIR surface was modeled as a liquid with a refractive index value of 1.276, and a large target plane was positioned perpendicular to the macroscopic surface normal of the sheets, as shown in the cross-sectional views in Figure 7-17.

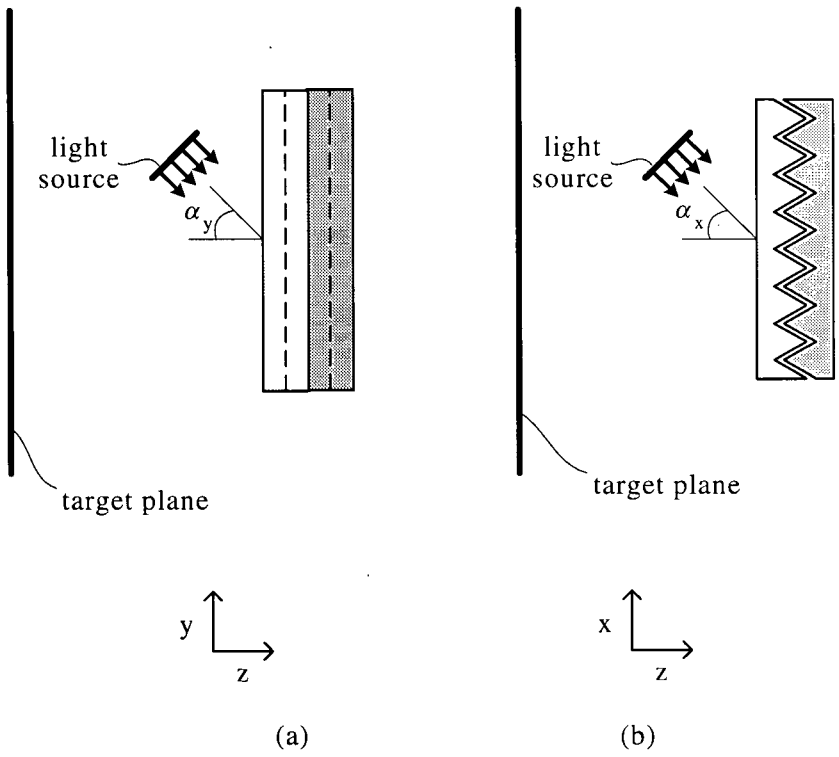

Figure 7-17. Light source and target plane position in interleaved 60°/60° model

The predicted reflectance values are shown for rotation of the source in the horizontal plane, α_x (α_y=0°) in Figure 7-18. At α_x=0° and α_y=0°, the system exhibited near-100% maximum reflectance and, as the source was rotated in the horizontal plane, the reflectance dropped steadily so that by ±20°, the value was reduced to 60%, and at ±50°, it was less than 20%. Across this full angular range, the reflectance of the absorptive state was less that 10%.

The reflectance as a function of source angle α_y, in the vertical plane, (α_x=0°) is near perfect over the range, from α_y=-60° to +60°, as shown in Figure 7-19. This is an expected result, since when the interleaved structure is viewed at α_x=0°, the optical configuration ensures TIR at any angle α_y. While this is true for the special case of α_x=0°, this perfect optical behaviour is not expected for other values of α_x.

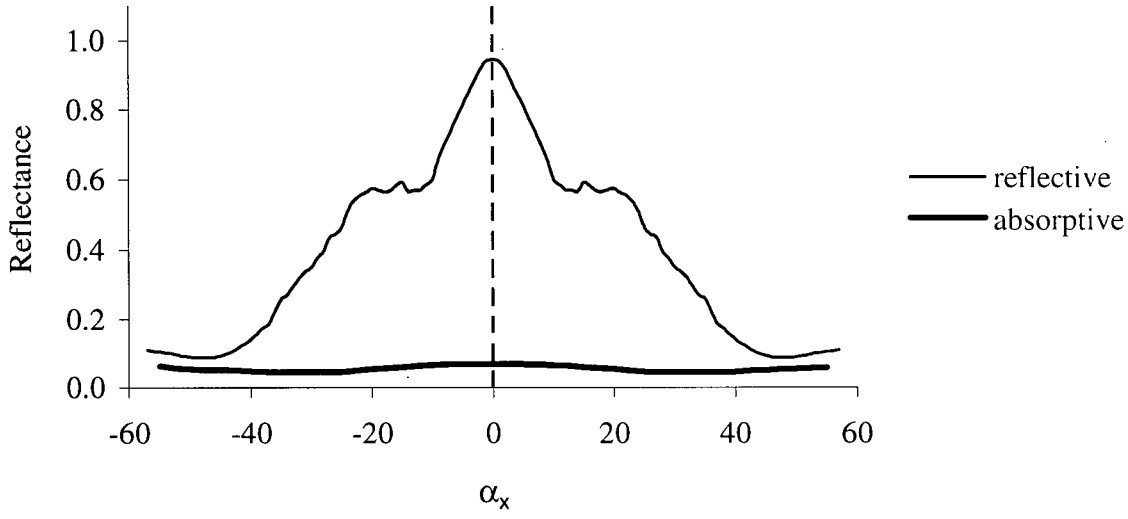

Figure 7-18. Reflectance in horizontal plane for interleaved 60°/60° system

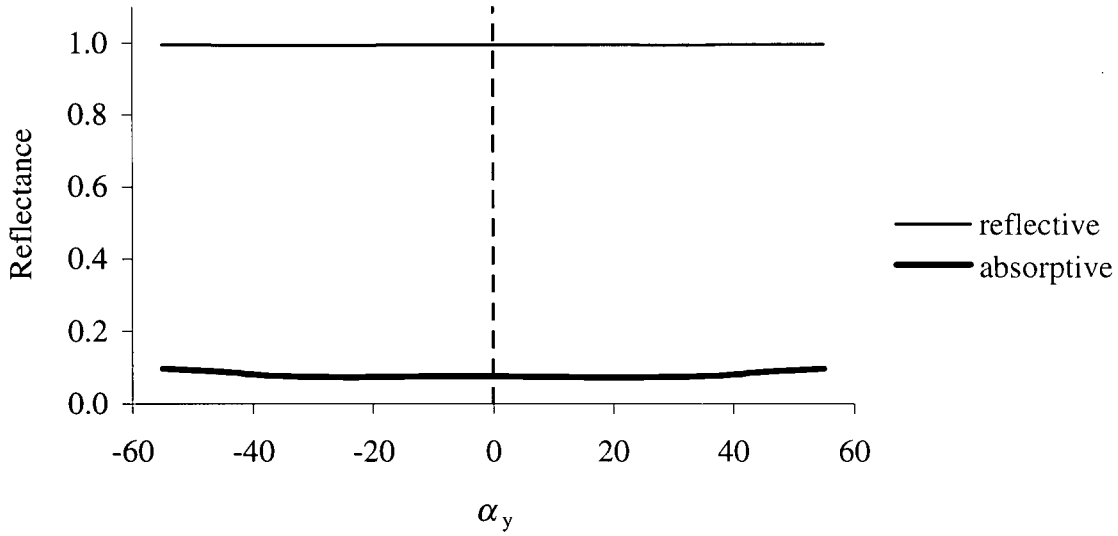

Figure 7-19. Reflectance in vertical plane for interleaved 60°/60° system

Using this raytrace model, the reflectance of the interleaved optical structure was predicted for many combinations of α_x and α_y. These reflectance values are shown in the contour plot in Figure 7-20, as a function of $\cos(\alpha_x)$ and $\cos(\alpha_y)$. As demonstrated by this contour plot, the reflectance is reasonably constant in the vertical plane, but decreases steadily in the horizontal plane as the viewing angle deviates from normal incidence. The plots in Figure

7-18 and Figure 7-19 predict this basic response, and there are no unexpected reflectance values for off-axis viewing angles.

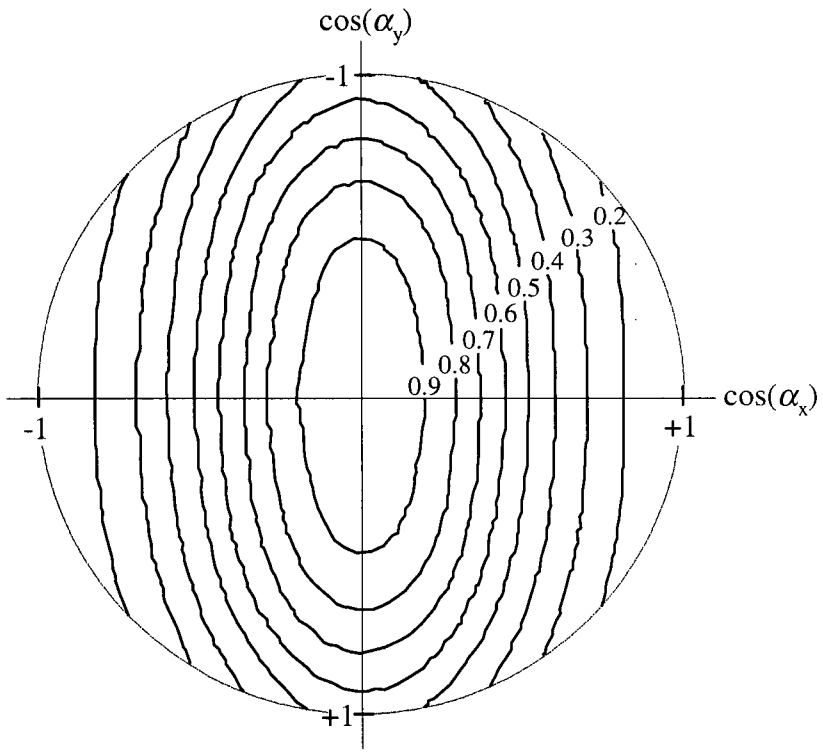

Figure 7-20. Contour plot of reflectance values for interleaved 60°/60° system

The interleaved geometry model predicts a very good angular response in the vertical plane, and a more limited response in the horizontal plane. This system, if incorporated into a reflective image device, would result in reasonably high image quality and, combined with the practical advantages associated with the flat front and rear surfaces of the device, could make the interleaved geometry a preferred structure in some device applications.

The predictions made by the TracePro® models confirm that the layered optical configurations generate high surface reflectance values, and are therefore practical to use in a reflective image device. As mentioned earlier, some micro-prismatic sheets are currently fabricated for use, on a commercial basis, in unrelated optical systems, but the micro-prism structures specifically designed for use in the layered configurations are unfortunately not among these. The ability to fabricate high-quality microstructures is well established, but the

set-up costs associated with the production of an optical sheet with a modified structure profile are very high. So, it is important to fully evaluate various shapes, sizes and orientations of the microstructures, as done in this section, prior to manufacturing such samples, in order to justify the substantial investment.

In the following section, the experimental reflectance measurements of a test sample, constructed using available, non-ideal microstructured sheets, are compared to the model predictions. The validity of the ray tracing predictions are not in doubt, however as a final check, it is important to establish that a ray trace model of a particular structure predicts reflectance values in reasonable agreement with experimental measurements.

7.5 Experimental results of modulated TIR in micro-prisms

As mentioned earlier, a primary purpose of this thesis is to establish the capability of a TIR-based reflective image device to modulate a surface with high contrast between the reflective and absorptive states. In an ideal case, the layered optical structures modelled in the previous section would be incorporated into a test cell, so that the reflectance values could be compared to the model predictions. Unfortunately, it is currently not possible to construct these experimental samples, since the β=60° micro-prism sheets, with optically smooth surfaces, as well as highly efficient anti-reflective coatings, are not available. The ray trace predictions of these structures, adapted so as to be ideal for this application, are necessary to demonstrate their optical potential, in order to justify the investment required to fabricate them. Although the model predictions are considered to be valid, a test was devised to provide experimental verification of the TracePro® results by comparison to a system based on available materials.

The test sample constructed for this experiment used micro-prismatic optical sheets to cause the TIR, as well as an electrophoretic pigment suspension to frustrate it. Therefore, this experiment integrated the various components described up to this point in the thesis, and demonstrated a real TIR-based reflective image device, actuated by pigment electrophoresis.

To construct the experimental sample, a configuration of available microstructured sheets was used which had several "non-ideal" departures from the β=60° micro-prism top sheet in

the layered 60°/90°/90° structure described in Section 7.3.3. The top β=60° sheet was replaced with a β=70° polycarbonate micro-prism sheet, having a prism tip-to-tip separation (or "pitch") of about 250 μm. For the rear layer, two 90° polycarbonate micro-prism sheets, oriented with mutually perpendicular symmetry directions, were laminated together using a 50 μm thick layer of optically clear, double-sided adhesive[88]. The micro-prismatic surface of the rear 90° sheet was coated, by vacuum deposition, with a thin layer of conductive ITO, in order to provide the transparent electrode for electrophoretic control of the pigment particles. (By measuring the reflectance of this 90°/90° structure alone, it was determined that imperfections in the lamination and ITO coating resulted in approximately a 30% loss due to scattering and absorption.) Lastly, instead of an intermediate refractive index material between the two sheets, an air gap was employed, to help make up for the reduced refraction in the top sheet.

A 75 mm x 75 mm sample was constructed using a similar method to the one described for the test cells in Section 4.1.3. In this case, however, the micro-prismatic sheet assembly was used for the top surface of the cell, so that TIR occurred in many tiny prisms, rather than the single large prism, described for the previous experimental technique. The assembly was sealed around the perimeter, using fast-curing epoxy, to a flat rear ITO coated glass surface. Again, approximately 50 μm diameter glass micro-spheres were used to separate the two electrode surfaces. The experimental suspension, in this case the magenta pigment sample, was injected into the cavity between the micro-prism sheets through two small holes that were then sealed.

The reflectance of the TIR and frustrated TIR states was measured for comparison to the model predictions. To take this measurement, the sample was placed inside a 3 m diameter integrating sphere, which was illuminated by a diffuse, broadband light source. The integrating sphere is a hollow, approximately spherical structure, lined with a highly diffusely reflective material. Standard methods for measuring luminance distributions use this structure, since light rays from a source reflect many times inside the sphere, and the luminance measured through a small viewing port in the side of the sphere ensures an accurate measurement regardless of the angular distribution. The sphere provides a highly uniform ambient luminance field that is equivalent to the one modelled in the ray tracing

analysis. The luminous reflectance was measured at a number of angles using a Sekonic Model L-776 luminance meter[89]. (In this measurement, the position of the sample was rotated while the light source and the detector remained fixed. As explained in Section 7.4.2, this is optically equivalent to fixing the detector and the sample in position, and moving the source, as in the model.)

TracePro® was used to predict the reflectance values of this experimental sample, by including the various non-idealities described above. Fresnel reflections were enabled on all surfaces, and some absorption was assigned to the interface between the two 90° micro-prism sheets to account for the losses resulting from the lamination and the ITO coating. The reflectance values predicted by this model are compared to the experimental results in Figure 7-21.

The experimental measurements are shown to be in reasonable agreement with the predicted values. The agreement is not perfect, probably as a result of surface imperfections in the fabricated micro-prisms used in this experiment. The prismatic facets of these sheets are not perfectly smooth; random variations are known to cause some undesirable reflection or refraction of the incident light. Such variations could not be included in the TracePro® model that generated the curves shown in Figure 7-21, and probably account for the small discrepancies between the reflectance measurements and predictions. The sensitivity of the system to these surface variations is not a fundamental limitation of the technique, since micro-prisms with suitably smooth surfaces can certainly be produced.

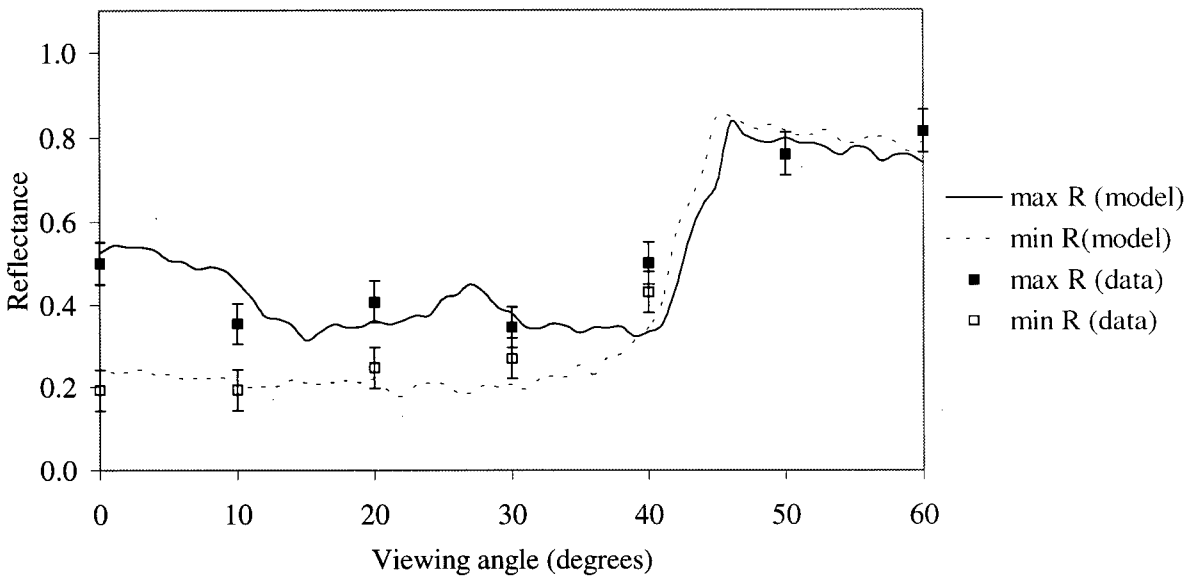

Figure 7-21. Comparison of measured and predicted reflectance values for 70°/90°/90° system

The overall reflectance of this sample is about 50%. A substantial portion of the loss is attributed to scattering or absorption as a result of the lamination and ITO coating procedures. As well, the prism structure is not ideal, since there are some losses associated with the replacement of the 60° prisms by the 70° top sheet. Again, these losses do not represent fundamental limitations of the TIR-based approach. Rather, they are strictly the result of the non-ideal optical geometry of the system employed in this experimental sample. For this reason, there is ample reason to be confident that ideally fabricated devices will indeed yield substantially higher reflectance and contrast.

In previous chapters, the two main device components, namely the absorptive pigment suspensions and the reflective polymeric structures, were analyzed. Specifically, the results presented in Chapters 4 and 5 established the feasibility of spectrally selective control of TIR by electrophoresis of pigment particles and, in this chapter, high surface reflectance using polycarbonate micro-prisms in contact with perfluorinated hydrocarbon liquid. Here, these two main components are combined into one test device and the comparison in Figure 7-21 establishes reasonable agreement between the experiment and the predictions. While this result is expected, this final test was important to demonstrate that this combined system is

compatible with optical switching in an actual micro-prismatic TIR-based reflective image device, and further supports the merit of continued development of this technology.

8 CONCLUSION

A new reflective image device technique, based on spectral control of total internal reflection in prismatic microstructures, has been investigated. Such a device makes use of the fact that TIR, a highly efficient reflection mechanism, can be controlled by moving a light-absorbing material toward or away from the interface at which the reflection occurs. Since this absorber need only move in and out of the microscopically thin evanescent region associated with the TIR, the transition can occur quickly and efficiently. When used in a reflective image device, the result is a high surface reflectance in the so-called "white" regions of an image, in stark contrast with the dark or coloured regions.

To achieve efficient frustration of TIR, the absorbing material must move to within less than 0.25 μm of the surface, but it need not make physical contact with the TIR interface; in fact, physical contact between the two solid materials is undesirable since, as was demonstrated in this study, it requires far more energy to subsequently remove the absorber from the surface. A practical method for preventing adhesion uses a liquid as the second medium, where the surface properties of the system make it energetically favourable for a thin layer of the liquid to remain between the two solid surfaces. This lubricating layer does not impede the frustration of TIR since it need only be a few molecules thick, but it substantially reduces the force required to extract the absorber from the evanescent wave region, making it practical to operate the device with low power consumption.

The results presented in this thesis have also demonstrated that pigment electrophoresis is a practical method for achieving this frustration of TIR. However, the observed reflectance modulation results could not be explained by a simplistic view of the absorption occurring only in the thin evanescent wave region. Rather, a more complete model shows that a concentration gradient of the particles in the region near the TIR surface, about an order of magnitude thicker than the evanescent wave region, is required to ensure sufficient absorption. This concentration gradient produces a corresponding gradient in the effective refractive index, since the higher index pigment particles increase the effective index of the lower index liquid. The presence of these particles at the interface, and the resulting modification of the refractive index ratio, causes the light to travel into the absorptive

pigment region rather than undergo TIR at the original interface. A numerical model describing the effect of this index gradient was used to predict the path followed by a light ray through the particle concentration gradient, and the resulting degree of absorption along the path. Following a comparison with the experimental measurements, the most likely distribution appeared to be one in which the particle density has an upper limit near the interface with an exponentially tapered tail. In addition to providing a greater understanding of the current suspension samples, this insight may be important for developing improved pigment suspensions with increased absorption capabilities.

A key result of this thesis is the first demonstration of spectral control of TIR. In order for these pigment suspensions to be useful in a subtractive colour filtering TIR-based device, they must be able to preferentially absorb certain wavelengths of visible light. In addition, the particles must be essentially non-scattering, so that light of non-absorbed wavelengths reflects as it would if the particles were not present. The experimental pigment suspensions have these characteristics and therefore successfully achieved the spectrally selective reflectance modulation. The colour gamut predicted for a reflective image device using these particular particle suspensions is reasonably large, indicating that spectrally selective pigment electrophoresis has the potential to generate bright, vivid full-colour images.

Novel configurations of microstructured sheets, yielding a high surface reflectance, form the basis of these devices. Currently, high quality, optically precise polycarbonate micro-prisms, with a refractive index value of n_1=1.59, are available from a number of commercial sources, and can be incorporated into these devices. The key to a high reflectance is a large mismatch between the refractive index values of the two interfacial materials, since this ensures that the conditions for TIR are achieved over a significant range of incident angles. However, while the use of a liquid as the second medium reduces adhesion problems, it complicates the optical requirements since the refractive index of most liquids is greater than n_2=1.33. In combination with polycarbonate micro-prisms, the refractive index ratio, n_1/n_2, at the interface is quite low, and for many light rays, TIR will not occur.

Two approaches were taken during the course of this study to address the problem. First, a recently developed, low index fluid was identified to somewhat increase the refractive index ratio. Perfluorinated hydrocarbon liquid, with a refractive index value as low as n_2=1.276, is

advantageous not only because of its low index property, but also because of its dielectric strength, high density and chemical compatibility with polycarbonate resin and pigment suspensions. Second, a new optical configuration was developed to enhance the effective refractive index ratio at the interface, to ensure that TIR occurs as desired. This is based on previous results concerning optical systems with translational symmetry. A light ray travelling in such a system with a component of motion in the symmetry direction will behave, upon striking an interface, as though the index ratio at that interface were enhanced, and if the enhancement is sufficient, the ray will undergo TIR. The new design takes advantage of the translational symmetry in the linear micro-prismatic structures incorporated in the device by using two micro-structured portions, oriented with mutually perpendicular symmetry directions. The first portion deflects the incident light, so as to impart to the rays a component of travel in the direction of symmetry of the second sheet. The effective index ratio between the second sheet and the liquid can then be sufficiently enhanced to ensure that TIR occurs over a wide range of incident angles. Using this technique, polycarbonate micro-prisms, in contact with perfluorinated hydrocarbon liquid, are capable of yielding the high surface reflectance desired for a reflective image display.

There are many possible arrangements of mutually perpendicular micro-structured sheets that exhibit this behaviour. Depending on the sheet orientation, refractive index values, and prisms structures, each configuration may have advantages for certain device applications. Throughout the course of this study, the reflectance, in both the reflective and absorptive state, of many of these systems was predicted, using Monte Carlo computer ray tracing models. The predicted reflectance values for a few of these ideal structures were presented in this thesis. Surface reflectance values were consistently very high in the reflective state, and very low in the absorptive state, and thus predicting that these structures would be appropriate to generate a bright, high contrast image. These results strongly suggest that such specialized structures should be manufactured in order to demonstrate these predictions to the fullest extent possible.

A final experiment in this thesis combined the experimental pigment suspensions with an arrangement of non-ideal, but currently available polycarbonate micro-prismatic sheets. The reflectance of the device surface was successfully modulated to generate the predicted

reflectance values, further establishing that pigment electrophoresis is a practical method for controlling TIR in the micro-prisms.

The research undertaken in this thesis has been intended as an investigative study into the physical practicality of using TIR in a reflective image device, in particular one yielding bright colour images. It is widely accepted that improvement in reflectance is required for reflective image displays, and the TIR-based technique has the potential to yield a high surface reflectance, far in excess of current commercially available displays. Clearly, substantial additional research would be required to develop a product based on this unique approach, but the knowledge gained in the course of this study bodes well for its commercial application.

These results present an opportunity for further study in a wide range of areas. The pigment suspensions used in this work have successfully demonstrated the capability of frustrating TIR, but it is important to emphasize that they are initial formulations, that could be improved in a number of ways. For instance, pigments with more specific absorption characteristics would improve the spectral selectivity and further increase the resultant colour gamut. Increased electrophoretic mobility, perhaps from greater particle charge, would increase switching speed. Purification experiments, as well as chemical analysis, may identify excess charge carriers associated with the unexplained residual current in the test devices, and help to eliminate this as a potential source of long-term chemical degradation.

A further area of suggested research involves a detailed study of the hysteretic effect of the interaction of the particles at the interface. It was observed that the particles were impeded from moving in and out of the evanescent wave region, and it was subsequently postulated that this resulted from micellar structures formed by excess dispersant. A greater understanding of this possible mechanism could be useful both for increasing the response speed of the particles and for developing a grey-scale mechanism for controlling the degree of reflectance.

From the point of view of practical device construction, methods of achieving long-term particle stability, most likely by micro-fluidic encapsulation, will be required. As well, the

inclusion of higher index microstructure polymer sheets will result in a substantial increase in the useful viewing angle of the display.

In summary, this thesis has outlined a physical basis for a new reflective image device based on total internal reflection, and established unique advantages over current reflective image displays. The results presented here demonstrate the feasibility of the approach, and suggest that this technique be considered for a variety of practical applications.

REFERENCES

[1] Jackson, J.D., *Classical Electrodynamics*, p. 286, John Wiley & Sons, New York, 1975

[2] ibid 1, p.286

[3] ibid 1, p. 278

[4] Gordon, J.M., "Spherical Gradient-Index Lenses as Perfect Imaging and Maximum Power Transfer Devices", Applied Optics, Vol. 39(22), 3825-3832, 2000

[5] Feuermann, D., Gordon, J.M., "Gradient Index Rods as Flux Concentrators with Applications to Laser Fibre Optic Surgery", *Optical Engineering*, Vol. 40(3) 418-424, 2001

[6] ibid 1, pp. 281-282

[7] Luneburg, R.K., *Mathematical Theory of Optics*, pp. 178-182, University of California Press, Berkeley, 1966

[8] Lorrain, P., Corson, D., Lorrain, F., *Electromagnetic Fields and Waves*, pp. 583-584, W.H. Freeman and Company, New York, 1987

[9] ibid, pp. 584-585

[10] Remillard, J.T., et al., "Evanescent Wave Scattering by Electrophoretic Microparticles – A Mechanism for Optical Switching", *Applied Optics*, Vol. 21, 3536-3538, 1995

[11] Trizact™ Film, manufactured by 3M Company, St. Paul, MN, 55144-1000, USA

[12] 2301 Optical Lighting Film, Product Identification Number 70-0061-8656-6, manufactured by 3M Company, St. Paul, MN, 55144-1000, USA

[13] Whitehead, L.A., et al., "New Efficient Light Guide for Interior Illumination", *Applied Optics*, Vol. 21(15), 2755-2757, 1982

[14] ibid 12

[15] 2370 Transmissive Film, Product Identification Number 70-0061-8656-4, manufactured by 3M Company, St. Paul, MN, 55144-1000, USA

[16] Whitehead, L.A. et al, "Visual Applications of Total Internal Reflection in Prismatic Microstructures", *Physics in Canada*, Vol. 57(6), 329-335, 2001

[17] Whitehead, L.A., "Simplified Ray Tracing in Cylindrical Systems", *Applied Optics*, Vol. 21(19), 3536-3538, 1982

[18] ibid 17

[19] Rea, M.S., ed., *Lighting Handbook Reference and Application*, p. 911, Illuminating Engineering Society of North America, New York, 1993

[20] Tyvek®, manufactured by Dupont Corporation, 1007 Market St., Wilmington DE, 19898, USA

[21] VM2000 Radiant Mirror Film, manufactured by 3M Company, St. Paul, MN, 55144-1000, USA

[22] ibid 19, p. 72

[23] ibid 19, p.109

[24] ibid 19, p. 111

[25] ibid 19, pp. 109-115

[26] ibid 19, p. 112

[27] Ross, S., Morrison, I., *Colloidal Systems and Interfaces*, John Wiley & Sons, New York, 236, 1988

[28] ibid 27, pp. 238-240

[29] ibid 27, pp. 346-348

[30] ibid 27, pp. 252-254

[31] ibid 27, pp. 354-359

[32] Kornbrekke, R.E., et al., "Electrophoretic Mobility Measurements in Low Conductivity Media", *Langmuir*, Vol. 8(4), 1992

[33] ibid

[34] ibid

[35] ibid 27, p.39

[36] ibid 32

[37] Hunter, R.J., *Zeta Potential in Colloid Science*, Academic Press, New York, 1981

[38] ibid 27, p. 46

[39] Morrissy, J.H., "Will Traditional TN/FSTN LCDs Dominate in Low Power, Reflective Display Applications?", *Society for Information Display Symposium Proceedings*, 80-83, 2001

[40] ibid

[41] Hashimoto, K., et al., "Reflective Colour Display Using Cholesteric Liquid Crystals", *Society for Information Display Symposium Proceedings*, 897-900, 1998

[42] Khan, A., et al., "Super High Brightness Reflective Cholesteric Display", *Society for Information Display Symposium Proceedings*, 460-463, 2001

[43] Davis, D., "Eight-Colour High-Resolution Reflective Cholesteric LCDs", *Society for Information Display Symposium Proceedings*, 901-904, 2001

[44] ibid

[45] Dalisa, A., "Electrophoretic Display Technology", *IEEE Transactions on Electron Devices*, Vol. 24, 827-834, 1977

[46] Swanson, S.A., et al., "High Performance Electrophoretic Displays", *Society for Information Display Symposium Proceedings*, 29-31, 2000

[47] Kishi, E., et al., "Development of In-Plane EPD", *Society for Information Display Symposium Proceedings*, 24-27, 2000

[48] Hou, J., et al., "Active Matrix Electrophoretic Displays Containing Black and White Particles of Opposite Polarities", *Society for Information Display Symposium Proceedings*, 164-167, 2001

[49] Murau, P., Singer, B., "The Understanding and Elimination of Some Suspension Instabilities in an Electrophoretic Display", *Journal of Applied Physics*, Vol. 49(9), 1978

[50] Drzaic, P., et al., "A Printed and Rollable Bistable Electronic Display", *Society for Information Display Symposium Proceedings*, 1131-1134, 1998

[51] Amundson, K., Drzaic, P, "Microencapsulated Electrophoretic Materials for Electronic Paper Displays", *International Display Research Conference Proceedings, Society for Information Display*, 84-87, 2000

[52] Nakamura, E., et al., "Development of Electrophoretic Display Using Microcapsulated Suspension", *Society for Information Display Symposium Proceedings*, 1014-1017, 1998

[53] Amundson, K., et al., "Flexible, Active-Matrix Display Constructed Using a Microencapsulated Electrophoretic Material and an Organic-Semiconductor-Based Backplane", *Society for Information Display Symposium Proceedings*, 160-163, 2001

[54] Whitehead, L.A., "Passive High Efficiency Variable Reflectance Image Display Device", US Patent 5,959,777, 1999

[55] Whitehead, L.A., et al., "Method and Apparatus for Controllable Frustration of Total Internal Reflection", US Patent 5,999,307, 1999

[56] Coope, R.J, et al., "Modulation of Retro-Reflection by Controlled Frustration of TIR", *Applied Optics*, submitted Jan 2002, under review

[57] ibid

[58] Fluorinert™ FC-75 Electronic Liquid, Product Identification Number 98-0211-3996-3, manufactured by 3M Company, St. Paul, MN, 55144-1000, USA

[59] ibid 17

[60] Whitehead, L.A., et al., "Enhanced Effective Index ACTIR Image Device":, US Patent 6,304,365, 2001

[61] ibid 27, p. 11

[62] Rao, S.P., "Liquid Toners for Use with Perfluorinated Solvents", US Patent 5,283,148, 1994

[63] Rao, S.P., "Liquid Toners for Use with Perfluorinated Solvents", US Patent 5,397,669, 1995 Rao, S.P., Smith, T.P., "Liquid Toners Utilizing Highly Fluorinated Solvents", US Patent 5,530,053, 1996

[64] Rao, S.P., Smith, T.P., "Liquid Toners Utilizing Highly Fluorinated Solvents", US Patent 5,530,053, 1996

[65] Rao, S.P., Advanced Materials Technology Center, 3M Company, St. Paul, MN, 55144-1000, USA, personal communication, 2000

[66] Coulter Model N4 Plus particle size analyzer, manufactured by Coulter Electronics, Inc., 590 West 20th St., Hialeah, FL, 33012-0145, USA

[67] ibid 27, p. 11

[68] Mossman, M.A. et al., "New Reflective Display Technique Based on Total Internal Reflection in Prismatic Microstructures", *Society for Information Display Symposium Proceedings*, 311-314, 2000

[69] Whitehead, L. A. et al., "Electrophoretic, Dual Refraction Frustration of Total Internal Reflection in High Efficiency Variable Reflectance Image Displays", US Patent 6,064,784, 2000

[70] Whitehead, L. A. et al., "Electrophoretic, High Index and Phase Transition Control of Total Internal Reflection in High Efficiency Variable Reflectance Image Display Devices", US Patent 6,215,920, 2001

[71] ibid 50

[72] ibid 50

[73] Solomentsev, Y., et al., "Particle Clustering and Pattern Formation During Electrophoretic Deposition: A Hydrodynamic Model", *Langmuir*, Vol. 13, 6058-6068, 1997

[74] ibid 51

[75] Mossman, M.A. et al., "New Reflective Colour Display Technique Based on Total Internal Reflection and Subtractive Colour Filtering", *Society for Information Display Symposium Proceedings*, 1054-1057, 2001

[76] Whitehead, L.A., Mossman, M.A., "Subtractive Filtering Frustrated TIR Display", US Patent allowed, February 2002, not yet issued

[77] PR®-650 Spectrascan® Colorimeter, manufactured by Photo Research®, 9731 Topanga Canyon Place, Chatsworth, CA, 91311-4135, USA

[78] ITO coated glass, supplied by Delta Technologies, Ltd., 13960 North 47th Street, Stillwater, MN, 55082-1234, USA

[79] Ilford Ilfochrome photographic filters, cyan (CP50C), magenta (CP50M) and yellow (CP50Y), supplied by Ilford Imaging Canada, Ltd., 361 Steelcase Road West, Unit #4, Markham, ON, L3R 3V8, Canada

[80] TSSL251 light-to-voltage optical sensor, manufactured by Texas Advanced Optoelectronic Solutions, Inc., 800 Jupiter Road, Suite 205, Plano, TX, 75074, USA

[81] Patton, T.C., ed., *Pigment Handbook, Volume III*, p. 72, John Wiley and Sons, New York, 1973

[82] Goos, F. and Hänchen, H., Ann. Physik Vol.1(33), 1947

[83] Kittel, C., *Introduction to Solid State Physics*, p. 130, John Wiley and Sons, New York, 1986

[84] Whitehead, L.A., et al., "Enhanced Effective Refractive Index Total Internal Reflection Image Display Device", US Patent 6,304,365, 2001

[85] BEF II Brightness Enhancement Film, manufactured by 3M Company, St. Paul, MN, 55144-1000, USA

[86] TracePro® raytracing software, a product of Lambda Research Corporation, 80 Taylor St., P.O. Box 1400, Littleton, MA, 01460-4400, USA

[87] AutoCAD® computer-aided design software, a product of Autodesk, Inc., 111 McInnis Parkway, San Rafael, CA, 94903, USA

[88] 8142 Optically Clear Adhesive, Product Identification Number 70-0061-8769-7, manufactured by 3M Company, St. Paul, MN, 55144-1000, USA

[89] Sekonic L-778 luminance meter, manufactured by Sekonic Professional Division, Mamiya America Corporation, 8 Westchester Plaza, Elmsford, NY, 10523, USA

APPENDIX A: USING DIFFERENTIAL SNELL'S LAW TO DETERMINE THE RAY PATH THROUGH A REGION OF REFRACTIVE INDEX GRADIENT

As described briefly in Section 2.1.2, the differential form of Snell's law in (2-9) can be used to calculate the path travelled by a light ray through a region of gradually varying refractive index. In particular, the procedure described in this appendix was followed to determine the degree of absorption as the light ray passes through a density distribution of moderately absorptive pigment near the TIR interface.

This calculation assumes a refractive index gradient along the direction of the y-axis, as illustrated in Figure A-1.

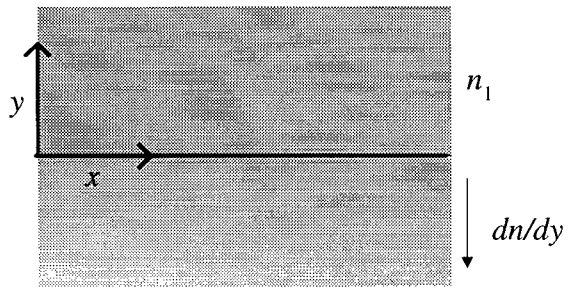

Figure A-1: Index gradient region

Equation (2-9) can then be simplified as:

$$\frac{d}{dl}(n\hat{r}) = \frac{dn}{dy}\,\hat{j} \qquad \textbf{(A-1)}$$

where dl is an increment of length along the ray path, and $\hat{j}$ is the unit vector in the y direction. At each location y in the distribution, the effective refractive index is estimated from the refractive index of the particles and the surrounding fluid and the concentration of the particles in the nearby region. Thus, the refractive index value $n(y)$ and the gradient dn/dy are known at any position y.

Equation (A-1) can be solved numerically by considering the position (x,y) and direction (v_x, v_y) of the light ray as the path length, l, increases by a small step, Δl. The initial position

(x_o,y_o) is known, and since the initial ray angle, θ_o, is known, the initial direction (v_{xo}, v_{yo}) is easily calculated. Using these initial conditions, the differential equation in (A-1) can be solved approximately, to first order, to determine the new direction (v_x, v_y) following the incremental increase in the path length, and from these values, the new position (x,y) is determined. This stepwise calculation is repeated to determine the ray path as the ray interacts with the index gradient.

Provided the increment Δl is sufficiently small, the error associated with this numerical solution is negligible. Figure A-2 demonstrates the calculated ray paths for two different incident angles. Here, the index gradient is calculated based on an exponentially tapered distribution (as in Chapter 6) of particles of n_p=2.0 suspended in a liquid of n_l=1.276, in contact with glass (n_1=1.5), and hence a critical angle, θ_c=58.3°. Figure A-2(a) shows that a light ray at θ_o=58.0° travels through the index gradient, whereas a light ray at 60.0° incidence, as in Figure A-2(b), undergoes total internal reflection. The transmitted angle in Figure A-2(a) is 85.5°, as predicted by the simplified expression of Snell's law in equation (2-7).

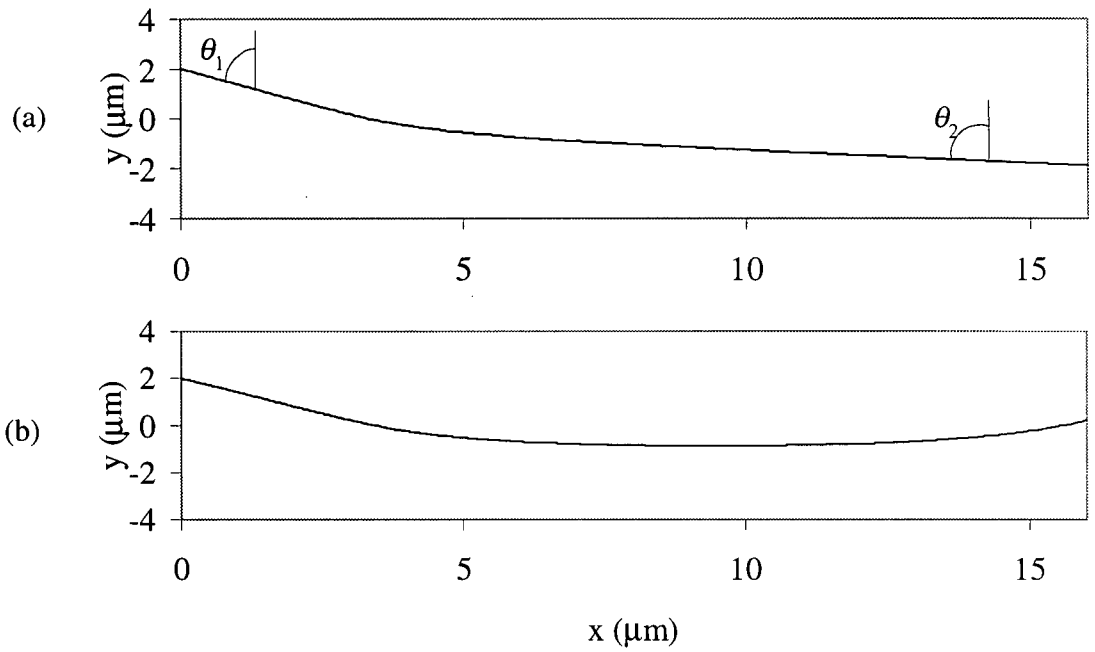

Figure A-2: Path calculated using differential Snell's law

APPENDIX B: CALCULATING REFLECTED LUMINANCE USING THE BI-DIRECTIONAL REFLECTANCE DISTRIBUTION FUNCTION

The bi-directional reflectance distribution function (BRDF) describes the directional dependence of light reflected from a surface in terms of the distribution of the incident light. A geometrical representation used to determine the BRDF is shown in Figure B-1.

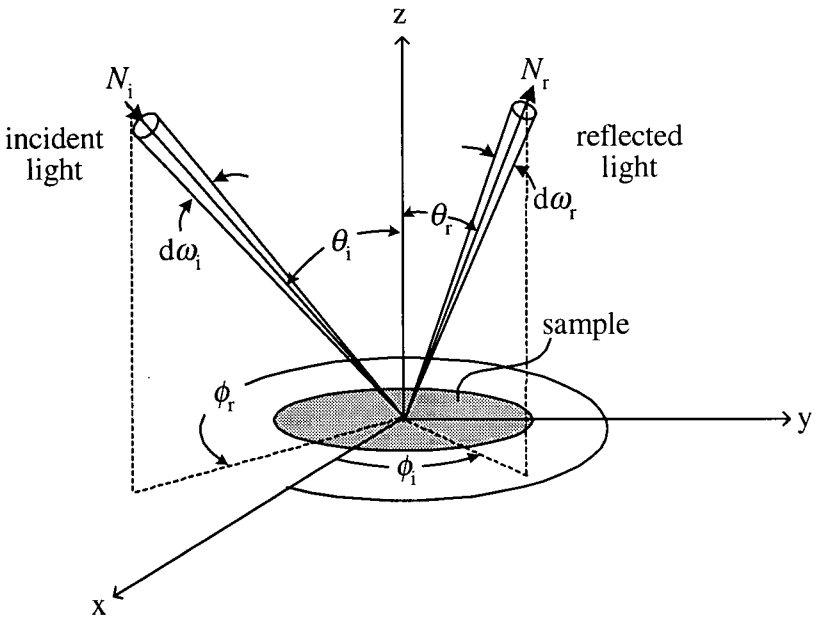

Figure B-1: Determining the reflectance of a surface using the BRDF

The direction of the incident light, N_i, is given by the angles (θ_i,ϕ_i), and the reflected light N_r by (θ_r,ϕ_r). The BRDF, $\rho'(\theta_i,\phi_i,\theta_r,\phi_r)$ is defined as the ratio of the reflected luminance in a particular direction to the incident illuminance from a particular direction.

$$N_r(\theta_r,\phi_r) = \oint d\omega_i \cos\theta_i N_i(\theta_i,\phi_i)\rho'(\theta_i,\phi_i,\theta_r,\phi_r) \qquad \textbf{(B-1)}$$

As a result of the dependence of the BRDF upon these four angles, the measurement of the reflectance of a surface is a non-trivial issue, and any values provided for the reflectance must specify the angles at which the measurement was taken.

APPENDIX C: PROPERTIES OF FC-75 FLUORINERT™ ELECTRONIC LIQUID

FC-75 Fluorinert™ Electronic Liquid is available from 3M Company (St. Paul, MN, USA), under product identification number 98-0211-3996-3. The physical and electrical properties of the material are listed in Table C-1.

Property	Value	Unit
Typical boiling point	375	K
Pour point	185	K
Average molecular weight	420	$g\,mol^{-1}$
Surface tension	$1.5x10^{-2}$	$N\,m^{-1}$
Critical temperature	500	K
Critical pressure	$1.6x10^{6}$	$N\,m^{-2}$
Refractive index	1.276	
Acoustic velocity	585	$m\,s^{-1}$
Vapour pressure	$4.1x10^{4}$	$N\,m^{-2}$
Solubility of water	11	ppm
Solubility of air @ STP	40	ml/100ml
Density	$1.77x10^{3}$	$kg\,m^{-3}$
Viscosity	$1.42x10^{-3}$	$kg\,m^{-1}\,s^{-1}$
Specific heat	$1.05x10^{3}$	$J\,kg^{-1}\,K^{-1}$
Heat of vapourization at B.P.	$8.8x10^{4}$	$J\,kg^{-1}$
Thermal conductivity	$6.3x10^{2}$	$W\,m^{-3}\,K^{-1}$
Coefficient of expansion	0.0014	K^{-1}
Volume resistivity	$8.0x10^{13}$	Ωm
Dielectric strength (2.54 mm gap)	$4.0x10^{4}$	V (RMS)
Dielectric constant (1 kHz)	1.86	
Dissipation factor (1 kHz)	<0.0001	$\tan\delta$

Table C-1: Properties of FC-75 at 25°C

APPENDIX D: CALCULATING CHROMATICITY COORDINATES AND LUMINOUS REFLECTANCE

The CIE method of colour specification, as described in Section 2.3.2, was used to predict the chromaticity coordinates for a full-colour reflective image device using the photographic filters and pigment systems analyzed in Chapter 4. An Excel spreadsheet program was used to calculate the chromaticity coordinates from the effective spectral transmittance measurements of the photographic filters, $C(\lambda)$, $M(\lambda)$, and $Y(\lambda)$ in Section 4.2.1 and of the pigment systems, $c(\lambda)$, $m(\lambda)$, and $y(\lambda)$ in Section 4.2.2, for each of the filter combinations representing each of the eight standard net colour states: red, green, blue, cyan, magenta, yellow, black and white. For illustrative purposes, a sample calculation for the net red state is provided in this appendix. Since the basic calculation is the same for each of the other colour states, it is not necessary to show them in detail here.

As discussed in the detailed description of the operation of the full-colour TIR-based reflective device in Section 3.12.3, a net red colour is generated by moving the magenta and yellow pigments, (but not the cyan pigments), into contact with the TIR interface. The average spectral reflectance function, $\rho_{average}(\lambda)$, is calculated in the spreadsheet as:

$$\rho_{average}(\lambda) = \frac{1}{3}(Y(\lambda)m(\lambda) + M(\lambda)y(\lambda) + C(\lambda)y(\lambda)m(\lambda)) \qquad \textbf{(D-1)}$$

from equations (3-3) to (3-6). Using equations (2-28) to (2-30), and the spectral CIE data for Standard Illuminant D_{65} in Table E-1 in Appendix E, the primary functions X, Y and Z are determined, and from these the chromaticity coordinates are calculated. Table D-1 shows the spreadsheet results for this prediction for net red state in Chapter 4.

λ	$\rho_Y(\lambda)$	$\rho_M(\lambda)$	$\rho_C(\lambda)$	$\rho_{average}$	$S(\lambda)\bar{x}(\lambda)\rho_{average}$	$S(\lambda)\bar{y}(\lambda)\rho_{average}$	$S(\lambda)\bar{z}(\lambda)\rho_{average}$
380	0.105	0.113	0.053	0.090	0.005	0.000	0.026
384	0.337	0.507	0.039	0.294	0.027	0.000	0.132
388	0.717	0.339	0.243	0.433	0.072	0.003	0.337
392	0.169	0.504	0.052	0.242	0.075	0.002	0.353
396	0.095	0.521	0.099	0.238	0.138	0.003	0.658
400	0.106	0.432	0.029	0.189	0.200	0.006	0.953

λ	$\rho_Y(\lambda)$	$\rho_M(\lambda)$	$\rho_C(\lambda)$	$\rho_{average}$	$S(\lambda)\bar{x}(\lambda)\rho_{average}$	$S(\lambda)\bar{y}(\lambda)\rho_{average}$	$S(\lambda)\bar{z}(\lambda)\rho_{average}$
404	0.356	0.188	0.148	0.231	0.383	0.011	1.817
408	0.539	0.091	0.111	0.247	0.699	0.020	3.328
412	0.437	0.054	0.155	0.215	1.007	0.028	4.804
416	0.289	0.042	0.121	0.151	1.112	0.032	5.320
420	0.344	0.028	0.128	0.166	1.877	0.055	9.010
424	0.306	0.025	0.106	0.145	2.407	0.078	11.587
428	0.276	0.026	0.091	0.131	2.789	0.103	13.531
432	0.277	0.022	0.092	0.131	3.456	0.151	16.925
436	0.245	0.022	0.082	0.116	3.707	0.193	18.327
440	0.221	0.021	0.073	0.105	3.814	0.240	19.065
444	0.233	0.021	0.081	0.112	4.271	0.332	21.690
448	0.183	0.018	0.064	0.088	3.460	0.335	17.927
452	0.180	0.020	0.065	0.088	3.440	0.414	18.269
456	0.157	0.023	0.058	0.079	2.963	0.449	16.221
460	0.119	0.025	0.043	0.063	2.193	0.424	12.457
464	0.116	0.028	0.043	0.062	1.942	0.494	11.524
468	0.126	0.033	0.051	0.070	1.848	0.653	11.568
472	0.124	0.038	0.052	0.071	1.519	0.785	10.181
476	0.096	0.043	0.040	0.060	0.984	0.780	7.198
480	0.098	0.052	0.044	0.065	0.782	1.001	6.422
484	0.104	0.060	0.047	0.070	0.578	1.245	5.517
488	0.089	0.069	0.042	0.067	0.351	1.353	4.089
492	0.081	0.083	0.041	0.068	0.214	1.626	3.304
496	0.068	0.097	0.037	0.068	0.113	1.916	2.623
500	0.061	0.117	0.037	0.072	0.050	2.423	2.247
504	0.059	0.127	0.037	0.074	0.024	3.010	1.905
508	0.056	0.133	0.036	0.075	0.041	3.617	1.548
512	0.056	0.130	0.037	0.074	0.109	4.169	1.188
516	0.054	0.122	0.036	0.071	0.226	4.541	0.844
520	0.053	0.116	0.036	0.068	0.397	4.954	0.602
524	0.054	0.115	0.039	0.069	0.667	5.593	0.481
528	0.057	0.120	0.041	0.073	1.028	6.378	0.398
532	0.059	0.130	0.044	0.078	1.472	7.231	0.330
536	0.062	0.139	0.045	0.082	1.956	7.911	0.260
540	0.060	0.145	0.045	0.083	2.414	8.253	0.192
544	0.059	0.144	0.043	0.082	2.835	8.290	0.137

λ	$\rho_Y(\lambda)$	$\rho_M(\lambda)$	$\rho_C(\lambda)$	$\rho_{average}$	$S(\lambda)\bar{x}(\lambda)\rho_{average}$	$S(\lambda)\bar{y}(\lambda)\rho_{average}$	$S(\lambda)\bar{z}(\lambda)\rho_{average}$
548	0.059	0.133	0.040	0.077	3.134	7.940	0.093
552	0.058	0.122	0.037	0.072	3.355	7.438	0.062
556	0.057	0.109	0.032	0.066	3.432	6.697	0.039
560	0.059	0.105	0.028	0.064	3.689	6.365	0.027
564	0.067	0.109	0.026	0.068	4.291	6.561	0.021
568	0.085	0.126	0.026	0.079	5.453	7.418	0.019
572	0.115	0.150	0.025	0.097	7.243	8.791	0.019
576	0.152	0.177	0.025	0.118	9.541	10.368	0.021
580	0.188	0.208	0.026	0.140	12.139	11.836	0.022
584	0.235	0.242	0.026	0.168	14.870	13.070	0.023
588	0.299	0.280	0.025	0.201	18.089	14.386	0.023
592	0.349	0.310	0.023	0.227	20.860	15.048	0.022
596	0.392	0.338	0.021	0.250	23.619	15.557	0.022
600	0.429	0.364	0.018	0.270	25.872	15.671	0.022
604	0.465	0.381	0.016	0.287	27.194	15.295	0.018
608	0.501	0.401	0.014	0.305	28.164	14.825	0.013
612	0.535	0.423	0.014	0.324	28.580	14.183	0.008
616	0.562	0.444	0.013	0.340	28.158	13.264	0.007
620	0.583	0.457	0.013	0.351	26.890	12.107	0.007
624	0.600	0.470	0.013	0.361	24.620	10.709	0.004
628	0.604	0.482	0.014	0.367	21.860	9.226	0.001
632	0.608	0.492	0.014	0.371	19.289	7.922	0.000
636	0.607	0.501	0.015	0.374	16.962	6.799	0.000
640	0.604	0.510	0.017	0.377	14.710	5.772	0.000
644	0.602	0.519	0.017	0.380	12.349	4.771	0.000
648	0.602	0.528	0.018	0.383	10.202	3.888	0.000
652	0.610	0.535	0.017	0.388	8.413	3.169	0.000
656	0.620	0.543	0.016	0.393	6.914	2.581	0.000
660	0.619	0.546	0.014	0.393	5.511	2.044	0.000
664	0.612	0.544	0.012	0.389	4.359	1.607	0.000
668	0.612	0.554	0.012	0.393	3.457	1.268	0.000
672	0.615	0.567	0.012	0.398	2.697	0.986	0.000
676	0.617	0.576	0.012	0.402	2.058	0.750	0.000
680	0.630	0.587	0.016	0.411	1.602	0.583	0.000
684	0.632	0.594	0.021	0.416	1.195	0.434	0.000
688	0.643	0.601	0.031	0.425	0.879	0.320	0.000

λ	$\rho_Y(\lambda)$	$\rho_M(\lambda)$	$\rho_C(\lambda)$	$\rho_{average}$	$S(\lambda)\bar{x}(\lambda)\rho_{average}$	$S(\lambda)\bar{y}(\lambda)\rho_{average}$	$S(\lambda)\bar{z}(\lambda)\rho_{average}$
696	0.658	0.614	0.059	0.444	0.503	0.180	0.000
700	0.661	0.620	0.071	0.451	0.392	0.140	0.000
704	0.663	0.626	0.087	0.458	0.311	0.113	0.000
708	0.666	0.632	0.109	0.469	0.248	0.091	0.000
712	0.668	0.638	0.139	0.482	0.191	0.070	0.000
716	0.671	0.643	0.154	0.489	0.136	0.050	0.000
720	0.673	0.609	0.176	0.486	0.092	0.034	0.000
724	0.675	0.603	0.184	0.487	0.073	0.026	0.000
728	0.636	0.595	0.193	0.474	0.058	0.021	0.000
732	0.649	0.628	0.233	0.504	0.049	0.018	0.000
736	0.619	0.589	0.232	0.480	0.036	0.013	0.000
740	0.668	0.603	0.284	0.518	0.031	0.010	0.000
744	0.650	0.642	0.272	0.521	0.023	0.006	0.000
748	0.656	0.629	0.278	0.521	0.015	0.005	0.000
752	0.638	0.682	0.288	0.536	0.009	0.003	0.000
756	0.686	0.631	0.337	0.551	0.006	0.000	0.000
760	0.684	0.676	0.409	0.590	0.006	0.000	0.000
764	0.684	0.527	0.397	0.536	0.005	0.000	0.000
768	0.573	0.460	0.378	0.470	0.005	0.000	0.000
772	0.465	0.435	0.205	0.369	0.002	0.000	0.000
776	0.675	0.672	0.300	0.549	0.000	0.000	0.000
780	0.687	0.596	0.420	0.568	0.000	0.000	0.000
				sum=	512.141	359.773	265.789

x=	0.450
y=	0.316
ρ=	0.136

Table D-1: Sample calculation of chromaticity coordinates

APPENDIX E: SPECTROPHOTOMETRIC CURVE FOR A SURFACE ILLUMINATED BY STANDARD ILLUMINANT D_{65}

Table E-1 provides the spectral CIE data for Illuminant D_{65} in terms of the colour matching functions.[24] These values were used to calculate the chromaticity coordinates provided in Table 4-1, by following the procedure outlined in Appendix D.

λ	$\bar{x}(\lambda)S(\lambda)$	$\bar{y}(\lambda)S(\lambda)$	$\bar{z}(\lambda)S(\lambda)$	λ	$\bar{x}(\lambda)S(\lambda)$	$\bar{y}(\lambda)S(\lambda)$	$\bar{z}(\lambda)S(\lambda)$
380	0.06	0	0.29	515	2.55	62.39	12.76
385	0.1	0	0.49	520	5.8	72.39	8.79
390	0.21	0.01	0.97	525	10.57	82.64	6.46
395	0.46	0.01	2.19	530	16.57	91.48	4.84
400	1.06	0.03	5.05	535	22.63	96.02	3.4
405	1.81	0.05	8.58	540	28.93	98.9	2.3
410	3.52	0.1	16.77	545	36.01	101.73	1.52
415	6.4	0.18	30.59	550	43.53	103.3	0.99
420	11.28	0.33	54.15	555	50.6	101.99	0.64
425	17.89	0.59	86.14	560	57.78	99.69	0.42
430	23.56	0.92	114.76	565	64.95	96.47	0.29
435	30.8	1.51	151.78	570	71.82	92.3	0.21
440	36.3	2.28	181.45	575	79.42	88.71	0.18
445	38.75	3.15	197.52	580	86.43	84.27	0.16
450	39.68	4.24	207.79	585	89.22	76.34	0.13
455	37.91	5.38	205.76	590	90.29	68.22	0.1
460	35.02	6.77	198.95	595	94.04	63.21	0.09
465	30.3	8.25	182.02	600	95.67	57.95	0.08
470	23.75	10.02	153.77	605	94.38	52.05	0.06
475	17.57	12.45	125.79	610	90.77	46.2	0.03
480	12.09	15.47	99.3	615	84.47	40.19	0.02
485	7.26	18.28	73.28	620	76.56	34.47	0.02
490	3.96	21.7	53.53	625	66.08	28.45	0.01
495	1.91	27	40.68	630	55.29	22.96	0
500	0.69	33.74	31.29	635	46.87	18.87	0
505	0.24	42.27	24.26	640	39.02	15.31	0
510	0.75	52.06	18.17	645	30.9	11.88	0

λ	$\bar{x}(\lambda)S(\lambda)$	$\bar{y}(\lambda)S(\lambda)$	$\bar{z}(\lambda)S(\lambda)$
650	23.85	9.02	0
655	18.49	6.91	0
660	14.02	5.2	0
665	10.49	3.86	0
670	7.68	2.81	0
675	5.43	1.98	0
680	3.9	1.42	0
685	2.62	0.95	0
690	1.7	0.62	0
695	1.2	0.43	0
700	0.87	0.31	0
705	0.63	0.23	0
710	0.46	0.17	0
715	0.3	0.11	0
720	0.19	0.07	0
725	0.14	0.05	0
730	0.11	0.04	0
735	0.08	0.03	0
740	0.06	0.02	0
745	0.04	0.01	0
750	0.02	0.01	0
755	0.01	0	0
760	0.01	0	0
765	0.01	0	0
770	0.01	0	0
775	0	0	0
780	0	0	0

Table E-1: Standard Illuminant D_{65}

APPENDIX F: SPECIFICATIONS OF TAOS TSL251 OPTICAL SENSOR

The specifications provided below are reproduced from the technical data sheet for the TSL251 light-to-voltage optical sensor, provided by Texas Advanced Optoelectronic Solutions.

Parameter	Min	Nom	Max	Unit
Supply Voltage, V_{DD}	3	5	9	V
Operating free-air temperature, T_A	0		70	°C

Table F-1: Recommended operating conditions of TSL251 optical sensor

Electrical Characteristics at V_{DD}=5V, T_A=25°C, λ_p=880nm, R_L=10KΩ:

Parameter	Test conditions	Min	Typ	Max	Unit
Dark voltage, V_D	E_e=0		0.003	0.010	V
Maximum output voltage swing, V_{OM}	E_e=2 mW/cm^2	3.1	3.5		V
Output voltage, V_O	E_e=25 μW/cm^2				V
	E_e=45 μW/cm^2	1	2	3	
	E_e=285 μW/cm^2				
Temperature coefficient of output voltage, α_{vo}	E_e=25 μW/cm^2, T_A=0°C to 70°C				V/ °C
	E_e=45 μW/cm^2, T_A=0°C to 70°C		±0.001		
	E_e=285 μW/cm^2, T_A=0°C to 70°C				
Irradiance responsivity, N_e	V_o=0.05 to 3V		4.5		(V m^2/W)
Supply current, I_{DD}	E_e=25 μW/cm^2				A
	E_e=45 μW/cm^2		9x10^{-4}	1.6x10^{-3}	
	E_e=285 μW/cm^2				

Table F-2: Electrical characteristics of TSL251 optical sensor

Operating Characteristics at T_A=25°C:

Parameter	Test conditions	Min	Typ	Max	Unit
Output pulse rise time, t_r	V_{DD}=5V, λ_p=880nm		9x10^{-5}		S
Output pulse fall time, t_f	V_{DD}=5V, λ_p=880nm		9x10^{-5}		S
Output noise voltage, V_n	V_{DD}=5V, f=20Hz		5x10^{-7}		V/sqrt(Hz)

Table F-3: Operating characteristics of TSL251 optical sensor

Typical Characteristic:

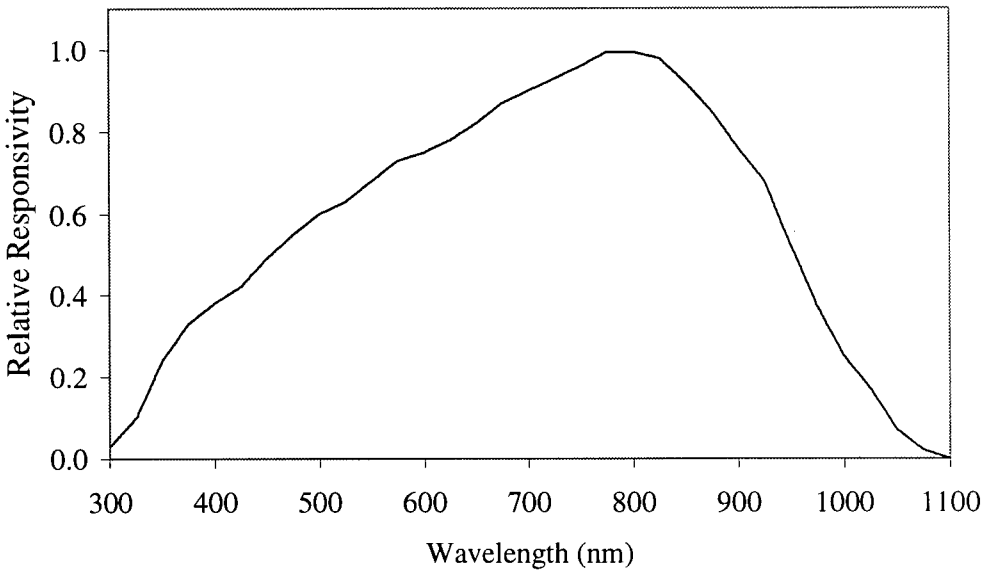

Figure F-1: Photodiode spectral responsivity

APPENDIX G: ANGULAR RESPONSE OF COLLIMATED DETECTOR

To determine the degree of collimation of light measured by the detector system, the angular response was measured using the experimental set-up depicted, as viewed from above, in Figure G-1. The collimated detector was held in a fixed position a distance x=0.9 m from a diffuse light source. The light source was then moved along the path perpendicular to the axis of the detector, and the response of the optical sensor was recorded at discrete positions, y, along this path. The angle, ϕ, between the light source and the detector was calculated trigonometrically.

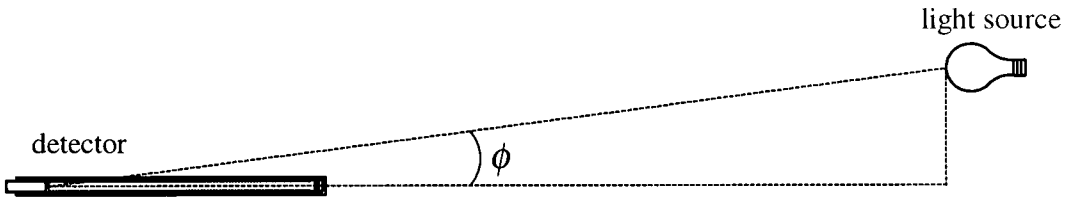

Figure G-1: Measuring the angular response of the collimated detector

In a highly collimated detector, the response of the optical sensor is be negligible, and there will be a peak response in a narrow angular region close to ϕ=0. The width of this peak, specifically the full-width half-max, determines the degree of collimation of the detector.

The normalized response, calculated as the fraction of the maximum response, was measured for the detector system used in this study and is shown in Figure G-2. The full-width half-max for this detector is ±1°.

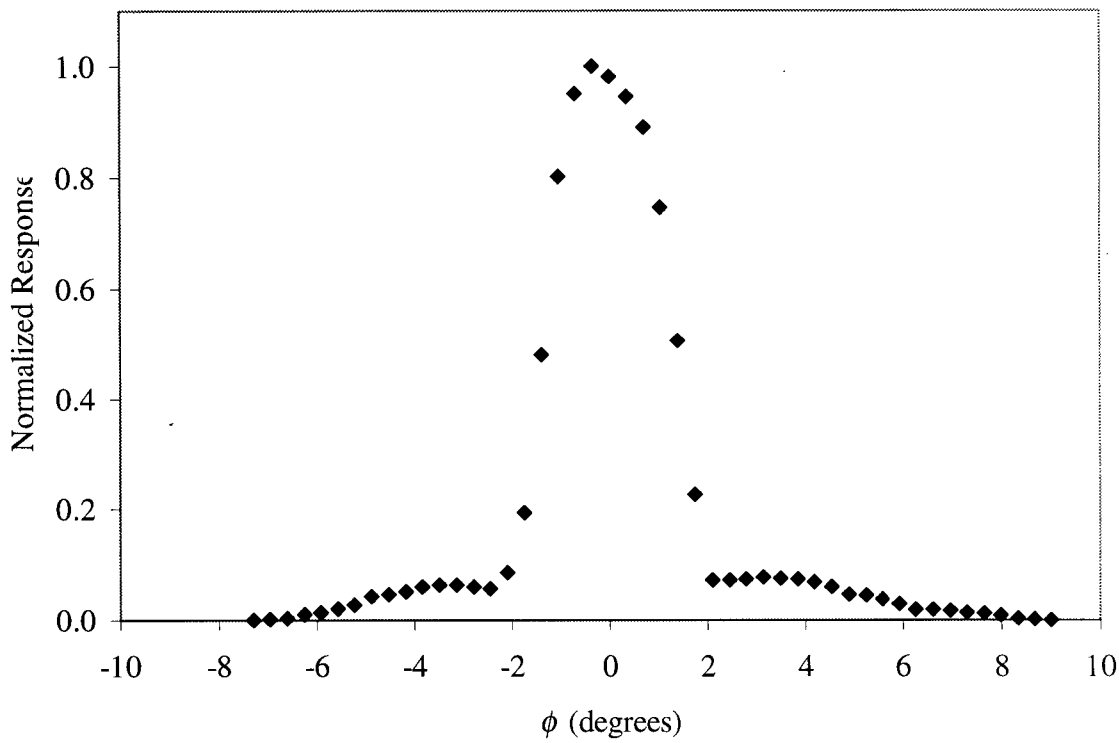

Figure G-2: Angular response of collimated detector

APPENDIX H: SPECTRAL TRANSMITTANCE OF FILTERS

For the reflectance measurement experiments in Chapter 5, wideband interference filters were used to control the wavelength of the detected light. These interference filters, obtained from optics components supplier Melles Griot, were multilayer thin film devices. Incident light passing through the filters undergoes multiple reflections between the coated surfaces comprising the filter. If there is no phase difference between the transmitted wavefronts, interference produces a transmission maximum for a given wavelength. By adjusting the optical path difference when the filter is constructed, the wavelength for which this maximum occurs can be accurately controlled. The result is a filter that will transmit a desired wavelength of light, while simultaneously rejecting longer and shorter wavelengths.

Three multilayer filters, specifically a blue filter (Melles Griot 03 FIB 004), a green filter (Melles Griot 03 FIB 006) and a red filter (Melles Griot 03 FIB 014), were used in the course of this study. Their transmittance characteristics were measured using the spectroradiometric telecolorimeter approach described earlier in Section 4.1, and are shown in Figure H-1.

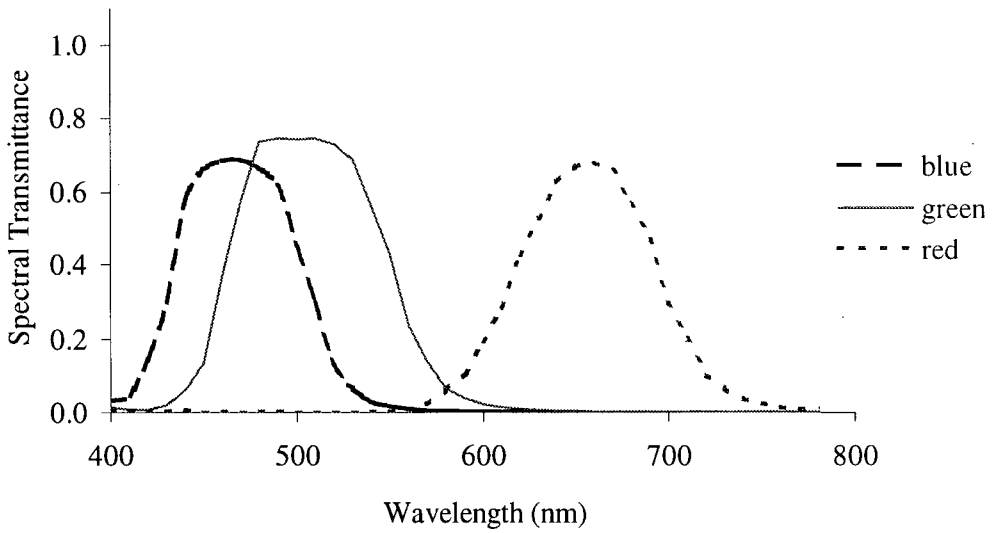

Figure H-1: Spectral transmittance of interference filters

Figure H-1 shows that the blue filter has a peak transmittance at 475 nm, and a full width half max of about 70 nm. Similarly, the green filter has a peak transmittance at 515 nm, and a full

width half max of about 90 nm, and the red filter has a peak transmittance at 660 nm, and a full width half max of about 80 nm.

To prevent unnecessary infrared radiation from reaching the optical sensor, a filter was used to separate the infrared radiation from the visible radiation by absorption. This heat-absorbing filter from Melles Griot (product number FCG 563) is made of KG1 Schott heat-absorbing glass that transmits light in the visible range, while absorbing radiation of wavelengths greater than 700nm. The transmittance characteristic shown in Figure H-2 was measured using the spectroradiometric telecolorimeter approach described in Section 4.1.

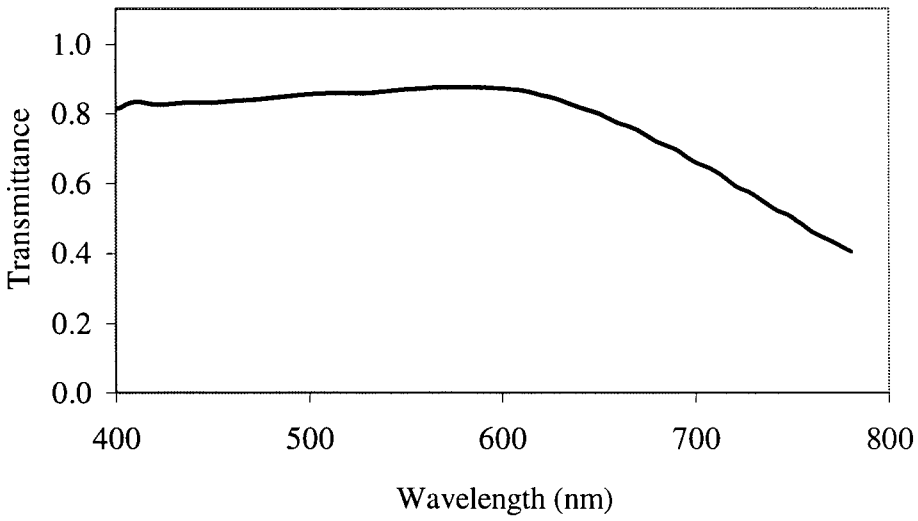

Figure H-2: Spectral transmittance of infrared filter

APPENDIX I: SPECTRAL RADIANCE DISTRIBUTION OF INCANDESCENT SOURCE

A diffuse, incandescent bulb was used as the light source to obtain the reflectance measurements presented in Chapter 5. The radiance distribution of this source was measured, as a function of wavelength, using the spectroradiometric telecolorimeter described in Chapter 4.

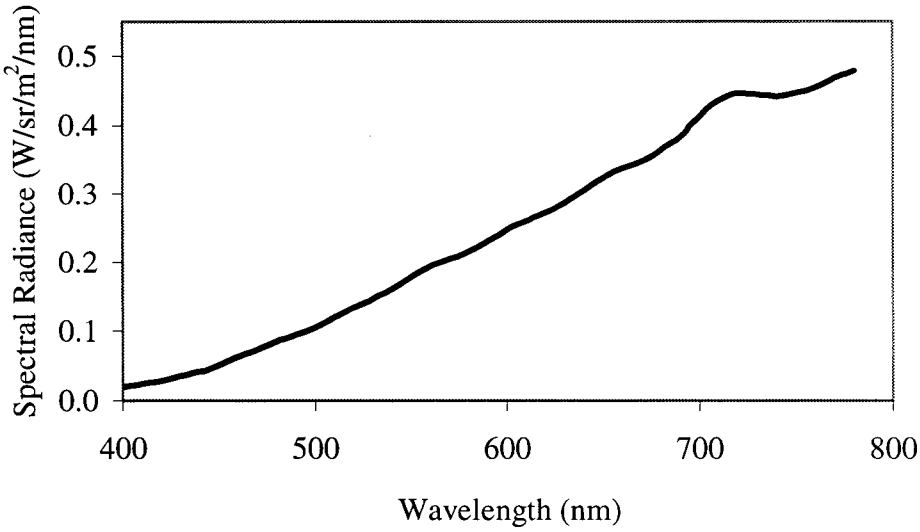

Figure I-1: Spectral radiance of incandescent source

The reflectance results are normalized by calculating the ratio of the measured optical sensor voltage to the maximum voltage measured with the same optical configuration, but without any absorbing particles. This normalization procedure takes into account the non-uniform spectral radiance distribution of the source.

APPENDIX J: EVANESCENT WAVE PENETRATION DEPTH

The evanescent wave penetration depth was calculated, for different incident angles, using the relationships provided in Section 2.1.3, at an interface between glass (n_1=1.5) and FC-75 Fluorinert™ electronic liquid (n_2=1.276). The results of these calculations, for three specific wavelengths of visible light, are shown in Figure J-1.

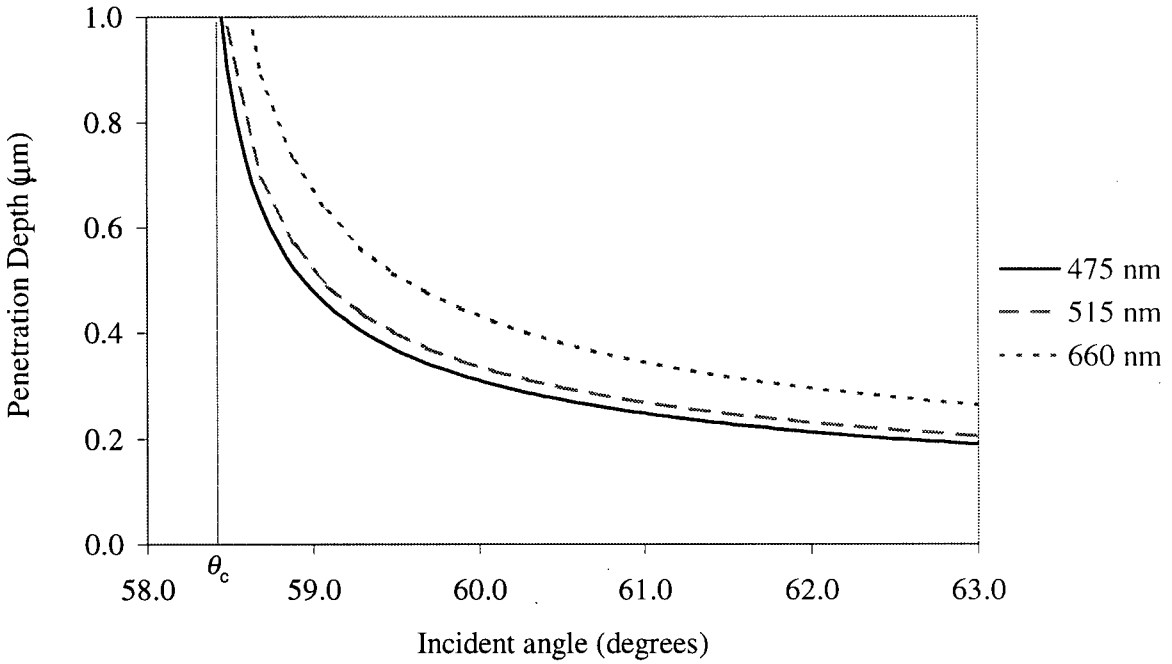

Figure J-1: Evanescent wave depth at polycarbonate/Fluorinert™ interface

The thickness of the evanescent wave region diverges at the critical angle, θ_c, and decreases rapidly as the incident angle increases. At $\theta=\theta_c+2°$, the penetration depth is about 0.25 μm, or half a wavelength. The wavelength comparison shows a significant difference between the depth of the evanescent wave across the visible spectrum.

APPENDIX K: FRESNEL EQUATIONS

The Fresnel equations[9] express the relationship between the electric field vectors of the incident, reflected and transmitted waves, $\boldsymbol{E}_I$, $\boldsymbol{E}_R$, and $\boldsymbol{E}_T$, at an interface between two materials. These relations are required to ensure the continuity of the tangential components of the electric and magnetic fields across the interface. Specifically, if these two materials are nonmagnetic and nonconductors, the Fresnel relations are given by:

$$\left(\frac{\mathbf{E}_R}{\mathbf{E}_I}\right)_{\perp} = \frac{(n_1/n_2)\cos\theta_I - \cos\theta_T}{(n_1/n_2)\cos\theta_I + \cos\theta_T}$$

$$\left(\frac{\mathbf{E}_T}{\mathbf{E}_I}\right)_{\perp} = \frac{2(n_1/n_2)\cos\theta_I}{(n_1/n_2)\cos\theta_I + \cos\theta_T}$$

$$\left(\frac{\mathbf{E}_R}{\mathbf{E}_I}\right)_{\parallel} = \frac{-\cos\theta_I + (n_1/n_2)\cos\theta_T}{\cos\theta_I + (n_1/n_2)\cos\theta_T}$$

$$\left(\frac{\mathbf{E}_T}{\mathbf{E}_I}\right)_{\parallel} = \frac{2(n_1/n_2)\cos\theta_T}{\cos\theta_I + (n_1/n_2)\cos\theta_T}$$

where θ_I is the angle of incidence, θ_T is the angle of transmission, and n_1 and n_2 are the indices of refraction of the two materials. Here, the subscript $\perp$ indicates that the $\boldsymbol{E}$ vectors are perpendicular to the plane of incidence, whereas the subscript $\parallel$ indicates that the $\boldsymbol{E}$ vectors are parallel to this plane.

The coefficients of reflection, R, and transmission, T, calculated as the ratio of the average flux of energy per unit area per unit time, are then given by:

$$R_{\perp} = \left[\frac{(n_1/n_2)\cos\theta_I - \cos\theta_T}{(n_1/n_2)\cos\theta_I + \cos\theta_T}\right]^2$$

$$T_{\perp} = \left[\frac{2(n_1/n_2)\cos\theta_I}{(n_1/n_2)\cos\theta_I + \cos\theta_T}\right]^2$$

$$R_{\parallel} = \left[\frac{-\cos\theta_I + (n_1/n_2)\cos\theta_T}{\cos\theta_I + (n_1/n_2)\cos\theta_T} \right]^2$$

$$T_{\parallel} = \left[\frac{2(n_1/n_2)\cos\theta_T}{\cos\theta_I + (n_1/n_2)\cos\theta_T} \right]^2$$

These relations were used to calculate the partial reflections at the interface in Section 7.3.

APPENDIX L: DESIGNING AN OPTICAL STRUCTURE IN TRACEPRO®

TracePro®, a commercially available computer ray tracing program, was used to predict the reflectance of the optical systems discussed in Chapter 7. To model these systems, the components of the structure were drawn using AutoCAD®, a three-dimensional computer design program, and imported into TracePro®. As an example, Figure L-1 shows the TracePro® model, in two cross-sectional views, of the layered 70°/90°/90° micro-prism geometry described in Section 7.4.

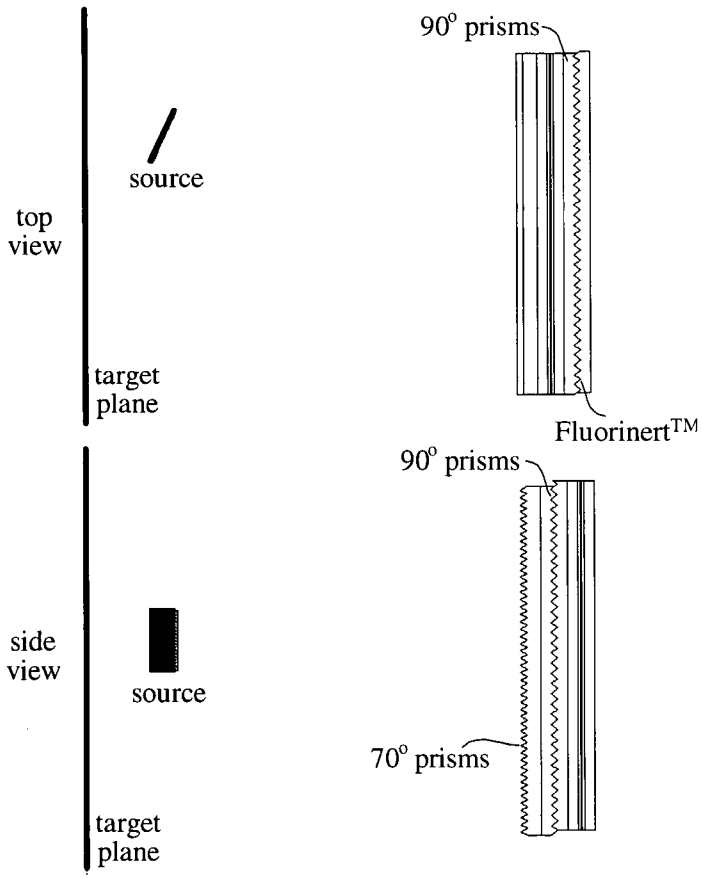

Figure L-1: Example of optical structure in TracePro®

In TracePro®, each component was assigned the desired optical characteristics, from a library of material properties, to represent a particular material. The light source directed on the surface was modeled as a highly collimated, planar source, and the angle of the source,

with respect to the optical system, was adjusted as desired. This basic procedure was used to predict the reflectance of the surface under various conditions.

APPENDIX M: TYPICAL OUTPUT FROM TRACEPRO®

The ray tracing program TracePro®, used to predict the reflectance of various optical structures in Chapter 7, presents output data in a number of forms. Two of these forms, in particular, were used often throughout the course of this study. The first involves a visual analysis of the ray paths. After the ray trace program has been completed for a given structure, the paths followed by a desired fraction of the rays were superimposed on the structure. This was particularly useful for interpreting the statistical data as it provided a direct indication of the ray behaviour. An example of such a ray diagram is shown, for the 70°/90°/90° structure, in Figure M-1. In this example, only 20 rays, superimposed on the structure, have been plotted. It is apparent from this example that some of the rays followed the desired TIR ray path, while others were either prematurely reflected, or did not undergo TIR at all.

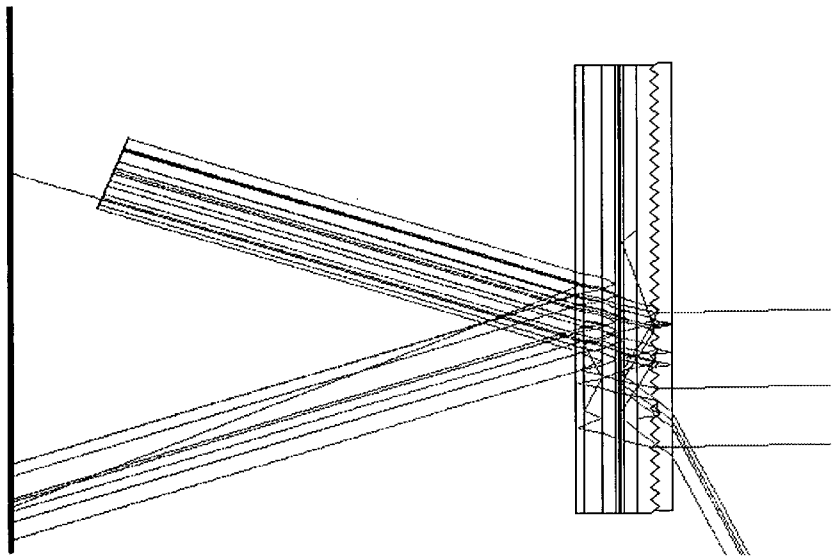

Figure M-1: Typical ray diagram for TracePro® model

In addition to this visual interpretation, the path followed by each ray in the analysis was recorded in a ray history table where, the refraction and reflection events of each ray were recorded, along with the geometrical coordinates at which these events occur. Table M-1 shows an excerpt from the ray history table for the ten rays that strike the target plane, as plotted in Figure M-1.

Ray number	Type	Incident flux	Absorbed flux	*x*	*y*	*z*
1	SpecTran	50.0	50	-159.22	223.78	272.52
2	SpecTran	40.5	40.5	-119.99	399.32	272.52
3	SpecTran	40.5	40.5	-233.02	201.62	272.52
4	SpecTran	50.0	50	-168.50	236.13	272.52
5	SpecTran	50.0	50	-163.03	242.36	272.52
6	SpecTran	50	50	-176.89	217.05	272.52
7	SpecRefl	50	50	-362.49	218.81	272.52
8	SpecTran	50	50	-159.51	242.52	272.52
9	SpecTran	50	50	-167.73	222.14	272.52
10	SpecTran	50	50	-174.36	210.93	272.52

Table M-1: Ray history table from TracePro® model

For each ray, the type of interaction, the incident flux and the absorbed flux were recorded, as well as the *x*, *y* and *z* coordinates where the ray intercepted the target plane. Using this data, the position, direction and intensity of each ray were determined at different points in the structure, and the behaviour was analyzed from a number of perspectives.